

Commensurate and incommensurate 1D interacting
quantum systems

Christopher Parsonage

Experimental Quantum Optics and Photonics Group

Department of Physics

University of Strathclyde, Glasgow

June 10, 2025

This thesis is the result of the author's original research. It has been composed by the author and has not been previously submitted for examination which has led to the award of a degree.

The copyright of this thesis belongs to the author under the terms of the United Kingdom Copyright Acts as qualified by University of Strathclyde Regulation 3.50. Due acknowledgement must always be made of the use of any material contained in, or derived from, this thesis.

Abstract

Quantum simulation is a versatile approach for exploring many-body quantum systems. Single-atom imaging using quantum gas microscopes has enabled direct observation of these systems in optical lattices. In this thesis, we employ a ^{87}Rb quantum gas microscope to investigate the physics of strongly interacting quantum systems. A key feature of this microscope is its ability to utilise engineered dynamic light potentials, which provide additional versatility for simulating complex quantum systems.

We explore the use of dynamically varying microscopic light potentials to study both commensurate and incommensurate one-dimensional (1D) systems. A system is said to be commensurate when there is an equal or multiple number of atoms to lattice sites, otherwise it is said to be incommensurate. In particular, we focus on strongly interacting incommensurate systems which, similar to doped insulating states, exhibit atom transport and compressibility. We begin with a commensurate system with unit filling and fixed atom number between two potential barriers. To prepare the incommensurate system, we dynamically adjust the position of the potential barriers, reducing the number of available lattice sites while maintaining a constant atom number.

We characterise these systems by measuring the distribution of particles and holes as a function of lattice filling and interaction strength, and probe particle mobility by applying a bias potential. Our work establishes the groundwork for preparing low-entropy states with controlled filling in optical lattice experiments, thus advancing our understanding of strongly correlated systems.

Additionally, we utilise these microscopic light potentials to realise the disordered Bose-Hubbard model, taking initial steps toward exploring the Bose-glass phase. The study of disordered systems opens new avenues for investigating localisation, phase

Chapter 0. Abstract

transitions, and the interplay between disorder and coherence.

Contents

Abstract	ii
List of Figures	vi
Acknowledgements	x
1 Introduction	1
2 Bose-Hubbard model and optical lattices	5
2.1 Model	5
2.2 Dipole traps	8
2.3 Optical lattice	9
2.4 Wannier functions	11
3 Experimental setup	16
3.1 Experiment	16
3.2 Initial cooling	17
3.3 Optical Pumping	19
3.4 Transport	19
3.5 Science chamber	20
3.6 Preparation of a 2D system	21
3.7 Cooling to quantum degeneracy	23
3.8 Imaging	24
3.9 Lattice calibration	27
3.10 Lattice alignment	28

Contents

3.11	Temperature	29
3.12	Time-of-flight imaging	30
3.13	Heating	33
4	Multi-wavelength single-site addressing	34
4.1	Introduction	34
4.2	Multi-wavelength set-up	35
4.3	Phase, feedback and dynamic control	38
4.4	Addressing beam	39
4.5	Repulsive potential	43
5	Commensurate and incommensurate 1D interacting quantum systems	45
5.1	Introduction	46
5.2	Preparation of (in)commensurate systems	47
5.3	Strongly and weakly interacting systems	54
5.4	Effect of post-selection	55
5.5	Atom number, variance and site occupations vs density	57
5.6	Particle mobility in a bias potential	61
5.7	Numerical simulations	62
5.8	Discussion	67
6	Disordered systems	68
6.1	Introduction	68
6.2	Preparation of the Bose-glass state	70
6.3	Edwards-Anderson parameter	73
6.4	Time-of-flight measurements	78
6.5	Outlook	79
7	Conclusion and outlook	82
7.0.1	Conclusion	82
7.0.2	Outlook	83

Contents

Bibliography

87

List of Figures

2.1	Phase diagram of the 2D Bose-Hubbard model.	6
2.2	Eigenenergies calculated from Eq.2.17 for a lattice with depth $V_0 = 5E_r$	12
2.3	Wannier functions at different lattice depths.	13
2.4	The interaction energy U vs the lattice depth in both V_x and V_y	14
2.5	The tunnelling term J vs the lattice depth.	15
3.1	3D render of the experiment	17
3.2	Top-down drawing of the MOT and Science chamber	18
3.3	Microwave spectrum for selecting a single anti-node of the vertical lattice.	21
3.4	Different stages of the evaporation sequence.	22
3.5	Experimental sequence for the evaporation in a single antinode.	23
3.6	Single atom imaging set-up	25
3.7	Fluorescence images of Mott insulators with and without modulating the position of the molasses beam	26
3.8	Relation between the lattice depth and the band structure	27
3.9	Parametric heating for lattice depth calibration	28
3.10	Temperature measurement of a Mott insulator	30
3.11	Time-of-flight momentum imaging with the microscope	31
3.12	Visibility measurement of the superfluid to Mott insulator transition . .	32
4.1	Schematic of the path for the 787 nm and 666 nm beams	36
4.2	Illustration of the affine transformation from the DMD plane to the atom plane	38

List of Figures

4.3	Light shift for $F = 1, m_F = -1$ and $F = 2, m_F = -2$ for wavelengths between the $D1$ and $D2$ lines	39
4.4	Microwave detuning for the transfer from the $F = 1$ state to the $F = 2$ state with and without the light shift from the addressing beam	40
4.5	Microwave detuning with intensity feedback on the addressing beam	41
4.6	Single line of atoms created using the addressing beam	42
4.7	The repulsive potential pattern shown at the three different stages of the experiment	43
4.8	Calibration of the repulsive potential	45
5.1	1D system preparation.	48
5.2	Experimental scenario and phase diagram.	49
5.3	Experimental procedure for doping a Mott insulator.	51
5.4	Strongly and weakly interacting commensurate and incommensurate 1D systems.	53
5.5	Effect of post-selection.	55
5.6	Atom number, variance, and site occupation of commensurate and incommensurate systems.	59
5.7	State detection probabilities for incommensurate systems with two additional particles.	60
5.8	Calibration of the magnetic gradient field	60
5.9	Mott insulator and doped insulator in a bias potential.	61
5.10	Numerical simulations.	64
5.11	Effect of the point spread function on the potential shape.	65
6.1	Illustration of the phase diagram of the disordered 2D bose-hubbard model.	70
6.2	Experimental procedure for preparing a Bose-glass	71
6.3	Calibration for the disorder pattern.	72
6.4	Illustration of the method for calculating $\langle \hat{n}_i \rangle$ the Edwards-Anderson order parameter	74
6.5	Average occupations and Edwards-Anderson parameters.	75

List of Figures

6.6	Radial average of the Edwards-Anderson parameter for different numbers of disorder patterns.	76
6.7	Radial average of the Edwards-Anderson parameter for different disorder strengths.	77
6.8	Time-of-flight images for a range of disorder strengths	78
6.9	Visibility measurement for increasing disorder strength	80
7.1	2-leg ladder	83
7.2	Time-of-flight imaging for a driven lattice	85

Acknowledgements

This PhD would not have been possible without the help and support of numerous individuals over the last four years.

First and foremost, I would like to extend my gratitude to Dr. Oliver Burrow and Prof. Paul Griffin. They introduced me to the field of research in physics and to the EQOP group. Without their guidance and support, I would not have started on the PhD, and they have continued to offer assistance throughout my PhD.

I also owe a great deal to Prof. Stefan Kuhr and Dr. Elmar Haller. Their patience and guidance in helping me with the research have been invaluable. Their willingness to answer any question has been instrumental in my growth as a researcher.

A special thanks goes to Andrea Di Carli, with whom I spent the majority of my time in the lab. Andrea not only taught me the ins and outs of the lab but also instilled in me a deep appreciation for Italian music. His help and expertise were crucial to my work.

I would like to thank all the members of the quantum gas microscope group who contributed to this PhD: James Howell, Paul Schroff, Matt Mitchell, Paul Catterson, Robbie Cruickshank, Illian Despard, Lennart Koehn, Arthur La Rooij, Lorenzo Carfora, Harikesh Ranganath, and Timon Hilker. Their collaboration and support have made this experience both enriching and enjoyable.

My gratitude also extends to everyone in my office, including the regular guests who joined us for physics discussions, knowledge exchanges, and works of art. These conversations were a great source of inspiration and balance during the PhD.

Finally, I would like to acknowledge those outside of the EQOP group who have made a significant impact during the last four years. My friends in the rowing club

Chapter 0. Acknowledgements

have provided a much-needed distraction and a space to unwind from the PhD. I am also grateful to my friends and teachers from school who have been a source of encouragement and motivation.

Chapter 1

Introduction

Quantum many-body systems are at the forefront of modern physics, offering insights into fundamental phenomena such as quantum phase transitions, conductivity, and entanglement. However, their study presents significant challenges, mainly due to the exponential growth of complexity as system size increases. This means that classical computers are impractical for simulating these systems at meaningful scales. Ultracold atoms can be used as quantum simulators, serving as versatile experimental platforms where quantum many-body physics can be explored under controlled conditions. By taking advantage of their tunability, you can emulate theoretical models and explore novel physics with direct relevance to areas such as condensed matter physics and quantum chemistry [1–4].

The experimental control achieved with ultracold atoms has expanded over the last decades. The introduction of a periodic potential to atomic systems is a central progress that has enabled the study of the Hubbard model. The Hubbard model is important in condensed matter physics and describes interacting particles in a lattice. The Hubbard model is useful for describing quantum phase transitions, between insulating and conducting phases. For bosons, this is the Mott insulator to superfluid transition, determined by the ratio of the interactions and the tunnelling. The system remains as a superfluid for a weak lattice potential, and will remain so as long as the interactions between atoms are small compared to the tunnelling. When the lattice potential is increased, the ratio between the interactions and the tunnelling increase and there is a

phase transition from the superfluid into the Mott insulator phase [5]. This proposal was made in 1998 [6] and was observed with rubidium atoms in 2002 [7]. By probing the momentum distribution of the system, they were able to observe the loss of phase coherence for an increasing lattice depth.

Subsequent developments have expanded the experimental toolkit for studying ultracold atoms in optical lattices. In particular, the addition of the quantum gas microscope has opened the way for further study of the Hubbard model with single-site resolved detection [8]. This led to experiments exploring the superfluid to Mott insulator transition in a 2D optical lattice with number statistics rather than the momentum distribution [9, 10]. To image the position of the atoms, the optical lattice is quickly changed to a deep lattice and fluorescence imaging is used where the photons are captured by a high NA objective and imaged on a camera. This method allows for the measurement of the position of the atoms, and can still measure the global phase coherence of the atoms by turning off the horizontal lattices and letting the atoms evolve for a short period of time of flight, before freezing the momentum distribution [10].

Beyond the study of the superfluid-to-Mott-insulator transition, ultracold atom systems have become ideal for investigating increasingly exotic quantum phenomena. More control techniques have emerged, enhancing the abilities of these platforms. For example, amplitude and phase modulation of optical lattices allows researchers to dynamically manipulate lattice parameters, including the tunnelling, through Floquet engineering [11]. Similarly, tightly focused lasers have been used to target individual lattice sites, inducing differential light shifts on these sites, that brings atoms into or out of microwave transitions [12]. The incorporation of digital micromirror devices (DMDs) has further increased experimental possibilities, enabling the creation of customized lattice geometries and disordered potentials [13]. Using these methods, researchers have prepared isolated systems with a few atoms only to explore entanglement entropy and other hallmarks of many-body quantum systems [14].

Significant open questions remain in the study of quantum many-body systems that are becoming more accessible to experimental platforms. Addressing these challenges requires continued innovation in both experimental and theoretical approaches. This

thesis builds upon these advancements to explore the role of commensurability in the lattice by designing a method to control the exact number of particles and lattice sites in 1D systems. When the number of particles is equal to, or a multiple of the number of lattice sites, the system is said to be commensurate. By adding an atom or a hole to the system, the particle number no longer matches the lattice sites, making the system incommensurate. This definition is different from the mathematical definition of commensurability that is based on rational and non-rational ratios [see [https://en.wikipedia.org/wiki/Commensurability_\(mathematics\)](https://en.wikipedia.org/wiki/Commensurability_(mathematics))]. It continues exploring the effect of disorder on strongly-correlated systems to study thermalisation and ergodicity. By combining theoretical concepts and experimental realizations, this work contributes to further advancing our understanding of fundamental physics in quantum many-body systems and its potential applications.

This thesis is structured as follows:

- **Chapter 2** explains the Bose-Hubbard model and its realisation with optical lattices. It goes into details about the quantum phase transition between the superfluid and the Mott insulator, and how to calculate the interaction and tunnelling terms in the Bose-Hubbard model.
- **Chapter 3** describes the experimental sequence for preparing a superfluid or Mott insulator. It explains the initial cooling steps and the selection of a single anti-node of the vertical lattice, before detailing the final evaporation to degeneracy.
- **Chapter 4** describes the set-up for using multiple wavelengths with a digital micromirror device with single-site addressing capabilities. It describes the calibrations and initial results for the different wavelengths used.
- **Chapter 5** describes the procedure to generate incommensurate 1D systems and the features of incommensurate systems. We explore the systems across the weakly to strongly interacting regime, and the effects of applying a bias potential.
- **Chapter 6** describes the physics when adding a disordered potential to the optical

Chapter 1. Introduction

lattice. The disordered Bose-Hubbard model includes the Bose-Glass phase, and we show our initial measurements of the superfluid to Bose-Glass transition and the Mott insulator to Bose-Glass transition.

- **Chapter 7** comprises a conclusion and outlook of the thesis.

List of publications and presentations to conferences

- *Commensurate and incommensurate 1D interacting quantum systems*
A. Di Carli, C. Parsonage, A. La Rooij, L. Koehn, C. Ulm, C. W Duncan, A. J Daley, E. Haller, and S. Kuhr
Nat Commun, vol. 15, no. 474, 2024.1815
- *Commensurate and incommensurate 1D interacting quantum systems*
C. Parsonage
QUAMP 2023

Chapter 2

Bose-Hubbard model and optical lattices

This thesis explores a specific type of quantum gas, the Bose-Einstein condensate, which takes advantage of the quantum properties of bosons, in our case ^{87}Rb atoms. In this chapter, we discuss the Bose-Hubbard model. We explore the two distinct quantum phases, the Mott insulator and the superfluid. We then discuss dipole traps and the optical lattice, which we use to realise the Bose-Hubbard model experimentally. Finally, we discuss how to calculate the maximally localised Wannier functions for determining the on-site interaction energy and the tunnelling energy.

2.1 Model

The Bose-Hubbard model describes interacting bosons in a lattice and can be realised with ultra-cold atoms in optical lattices [6, 7]. The Bose-Hubbard Hamiltonian in an optical lattice with a harmonic potential is given by

$$\hat{H} = -J \sum_{i,j} \hat{a}_i^\dagger \hat{a}_j + \sum_i \frac{U}{2} \hat{n}_i (\hat{n}_i - 1) + \sum_i (\epsilon_i - \mu) \hat{n}_i, \quad (2.1)$$

where \hat{a}_i^\dagger and \hat{a}_j are the creation and annihilation operators of particles on sites i and j , and $\hat{a}_i^\dagger \hat{a}_i = \hat{n}_i$ is the number operator. The first term in the Hamiltonian represents the tunnelling, where J is the tunnelling matrix element. The second term describes

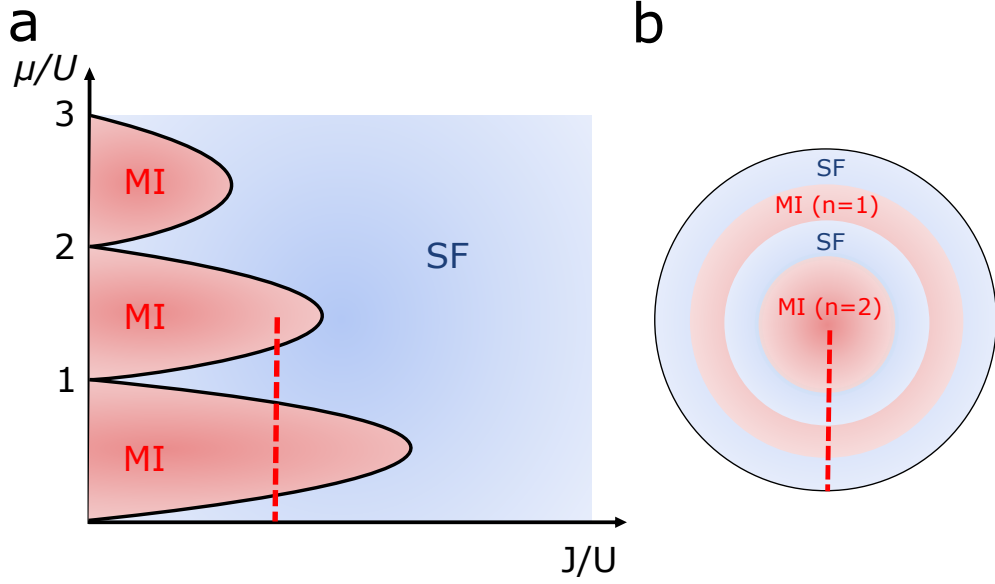


Figure 2.1: **Phase diagram of the 2D Bose-Hubbard model.** **a**, Illustration of the phase diagram with the dotted line representing the phases in **b**, adapted from [15]. **b**, The shell structure of a system with small finite tunnelling. The spatially varying chemical potential gives rise to regions of Mott insulating shells with different number of atoms per sites. The centre shell is a Mott insulator with 2 atoms per site that is separated from a Mott insulator with 1 atom per site by the superfluid phase.

the on-site interaction, where U is the interaction energy for two particles. The final term contains the energy offset, ϵ_i , of a lattice site in an external potential and the chemical potential, μ . The Gaussian beams used to generate the optical lattice cause a harmonic confinement in addition to the periodic optical lattice potential, leading to a spatially varying local chemical potential, $\mu_{loc} = \mu - V(i)$, where $V(i)$ is the potential offset on lattice site i from the harmonic potential. This means that locally the atom number and the variance in the atom number on a site can differ [9].

There are two distinct phases in the Bose-Hubbard model, the Mott insulator and the superfluid phase. In the case where the tunnelling energy is much larger than the interaction energy ($J \gg U$), the system is in the superfluid phase where the atoms are delocalised over the lattice. When $U \gg J$, the system is in the Mott insulator phase with an integer number of atoms per site and a vanishing variance. The varying local chemical potential leads to systems with both superfluid and Mott insulator phases locally. The dotted line (Figure 2.1) shows the varying chemical potential in the phase

diagram of the Bose-Hubbard model. The shell structure that arises from the chemical potential (Figure 2.1b) leads to regions with multiple atoms per site.

The system can be driven between the superfluid and the Mott insulator by changing the tunnelling and interaction terms. This is a quantum phase transition that occurs at zero temperature and is caused by quantum fluctuations in the position and phase of the atoms. When the system is driven from the superfluid to the Mott insulator, it becomes energetically unfavourable to have high fluctuations in the position of the atoms and there is atom number squeezing [16] and the variance of the atom number approaches zero. Experimentally, we can change the ratio between J and U using the lattice depth. For a shallow lattice, the system is in the superfluid phase with $J \gg U$. For increasing lattice depth, the ratio U/J increases and the system can be driven into the Mott insulator phase.

The superfluid can be described by a macroscopic wavefunction where the many-body ground state is given by

$$|\psi\rangle \propto \left(\sum_i^M \hat{a}_i^\dagger \right)^N |0\rangle, \quad (2.2)$$

where M is the number of lattice site and N is the number of bosons. This state is well described by the macroscopic wavefunction and exhibits long-range phase coherence. The atoms are delocalised over the lattice and occupy the same Bloch state. This superfluid state is compressible and has a gapless energy spectrum [7].

In the thermodynamic limit, where the number of atoms and lattice sites approaches infinity, the superfluid state has a Poissonian distribution of atoms, $P(n, \bar{n})$ [7]. The density can be written as a sum of the number particles multiplied by $P(n, \bar{n})$ and is given by

$$\bar{n} = \sum_{n=0}^{\infty} n \left(\frac{\bar{n}^n e^{-\bar{n}}}{n!} \right). \quad (2.3)$$

Experimentally, we can only detect the parity of the atom number (section 3.8). This means that any doubly-occupied sites are detected as empty sites, and any sites with three atoms are detected as a single atom. In [17] it is argued that the observed

atom number starts from zero and approaches a maximum value of 0.5 when the density increases. It is worth to note that away from the thermodynamic limit, with a restricted number of atoms and sites, the observed atom density in the superfluid can exceed $\bar{n} = 0.5$. This was observed later in the thesis for systems restricted to 6 or less atoms and lattice sites (Section: 5).

The Mott insulator has a significant energy cost for atoms occupying the same site as $U \gg J$. To minimise the interaction energy, the ground-state takes the form

$$|\psi\rangle \propto \prod_i^M (\hat{a}_i^\dagger)^N |0\rangle, \quad (2.4)$$

where the system is a collection of localised wavefunctions on each lattice site. The system cannot be described by a macroscopic wavefunction and has no long-range phase coherence. The Mott insulator state of a BEC corresponds to an incompressible gas and has an energy gap on the order of the interaction energy. In a harmonic trap, the varying local chemical potential leads to regions of Mott insulator shells separated by regions of superfluid for non-zero J/U (Figure 2.1b). The second shell forms when the onsite interaction energy to occupy the same site is lower than the energy offset of an atom a site further away from the centre of the trap, due to the energy offset from the harmonic trap.

The quantum phase transition between the Mott insulator and the superfluid occurs at a critical point for the ratio U/J . This critical point of the phase transition depends on the geometry of the system and the atom density. In 2D, the transition point has been calculated to be $(U/J)_c = 16.7$ at $\bar{n} = 1$, where \bar{n} is the density of the cloud [18] and for 1D the transition point is occurs at $(U/J)_c = 3.84$ for $\bar{n} = 1$ [19] and $(U/J)_c = 2.2\bar{n}$ for $\bar{n} \gg 1$.

2.2 Dipole traps

Far-detuned laser beams can be used to create dipole traps because the atoms experience a light shift when interacting with the light. When an atom is illuminated by the light, the electric field induces an atomic dipole moment. This dipole moment interacts

with the electric field and generates a potential of the form

$$V(r) = \frac{\Gamma\pi^2c^2}{2w_0^3} \left(\frac{2}{\Delta_{D2}} + \frac{1}{\Delta_{D1}} \right) I(r), \quad (2.5)$$

where Γ is the scattering rate, w_0 is the optical transition frequency, Δ_{D1} and Δ_{D2} is the detuning to the D1 and D2 line and $I(r)$ is the intensity of the laser [20]. For a red-detuned beam, the potential is attractive and atoms experience a force towards the region of highest intensity. Blue-detuned beams create a repulsive potential and atoms experience a force away from the higher intensity.

There are different types of dipole traps that can be formed using this effect. Blue-detuned light can be formed into a ring that traps atoms in the centre. For far red-detuned beams, atoms can be trapped in the focus of the beam.

2.3 Optical lattice

We realise the Bose-Hubbard model by trapping ultra-cold atoms in an optical lattice. We use far red-detuned light that is retro-reflected to create a standing wave where the atoms are trapped in the intensity peaks. The potential seen by the atoms in 1D is

$$V(x) = V_0 \cos^2 \left(\frac{\pi x}{d} \right), \quad (2.6)$$

where V_0 is the maximum potential depth and $d = \frac{\lambda}{2}$ is the lattice spacing. The lattice depth is often expressed in units of the recoil energy,

$$E_r = \frac{\hbar^2 \pi^2}{2md^2}, \quad (2.7)$$

where m is the atomic mass of ^{87}Rb . In practise, we use Gaussian beams with an intensity profile given by

$$I(r, z) = \frac{2P}{\pi w^2(z)} e^{\frac{-2r^2}{w^2(z)}}, \quad (2.8)$$

where P is the power of the laser, $w(z)$ is the waist of the beam, z is the axial distance from the centre and r is the radial distance. The intensity of the beam is directly

proportional to the potential $V(x)$ [21].

The potential in a 3D optical lattice then takes the form

$$V(x) = V_x \cos^2\left(\frac{\pi x}{d}\right) e^{-2\frac{y^2+z^2}{w^2(x)}} + V_y \cos^2\left(\frac{\pi y}{d}\right) e^{-2\frac{x^2+z^2}{w^2(y)}} + V_z \cos^2\left(\frac{\pi z}{d}\right) e^{-2\frac{x^2+y^2}{w^2(z)}}, \quad (2.9)$$

where V_x , V_y and V_x is the potential depth in each lattice direction and the exponential terms represent the harmonic confinement combined with the optical lattice. This potential can be approximated (assuming that we are considering distances much smaller than the beam waist) as the combination of the lattice potential and an external harmonic confinement [21],

$$V(x) = V_x \cos^2\left(\frac{\pi x}{d}\right) + V_y \cos^2\left(\frac{\pi y}{d}\right) + V_z \cos^2\left(\frac{\pi z}{d}\right) + \frac{m}{2} (\omega_x^2 x^2 + \omega_y^2 y^2 + \omega_z^2 z^2), \quad (2.10)$$

where $\omega_{x,y,z}$ are the trapping frequencies in the x , y and z directions. In our quantum gas microscope, V_z is usually larger than V_x and V_y to suppress tunnelling along the z direction. As a result, the harmonic trap on the lattice originates primarily from the vertical lattice.

The interaction and tunnelling energies, U and J , can be controlled in different ways. The lattice depth changes the size of the wave function (see below) on the lattice sites and thus determines both the interactions, and the tunnelling. This is the only method we use to control the two parameters in this thesis. The interactions can also be controlled with a Feshbach resonance that changes the scattering length [22], but it is not easily accessible for ^{87}Rb . The tunnelling term can also be controlled through amplitude or phase modulation of the lattice [23]. Through the lattice depth alone, we can access both Mott insulating and superfluid phases in the Bose-Hubbard model.

2.4 Wannier functions

To calculate the interaction and tunnelling energies for a specific lattice depth, we need to solve the Schrödinger equation and calculate the Wannier functions [24, 25]. The Wannier functions are a set of orthogonal localised wavefunctions that extend beyond a single lattice due to the non-zero tunnelling probability. The Wannier functions can be used to calculate both the interaction and tunnelling terms. The Wannier functions are calculated for each lattice direction, and a different tunnelling term is calculated for each lattice direction. The interaction term requires the product of the integral of the three different Wannier functions for each lattice. The Schrödinger equation is given by

$$-\frac{\hbar^2}{2m} \frac{\partial^2}{\partial x^2} \psi(x) + V(x)\psi(x) = E\psi(x), \quad (2.11)$$

where $\psi(x)$ is the wavefunction, m is the atomic mass and E is the energy. As $V(x)$ is a periodic potential (Eq.2.6), the solutions to the Schrödinger equation follow Bloch's theorem and have the form

$$\psi_{n,q}(x) = u_q^n(x)e^{iqx}, \quad (2.12)$$

where q is the quasimomentum, n is the band index and $u_q^n(x)$ is a periodic function. The Wannier functions are defined as

$$w_n(x) = \sqrt{\frac{a}{2\pi}} \int_{-\frac{a}{\pi}}^{\frac{a}{\pi}} u_q^n(x)e^{-iqx} dq, \quad (2.13)$$

where a is the lattice spacing.

By rewriting the Bloch function and the periodic potential as a Fourier series, we can then computationally solve the Schrodinger equation [26]. The periodic function is now given as

$$u_q^n(x) = \sum_{\nu} C_{\nu}^n e^{i\nu Gx}, \quad (2.14)$$

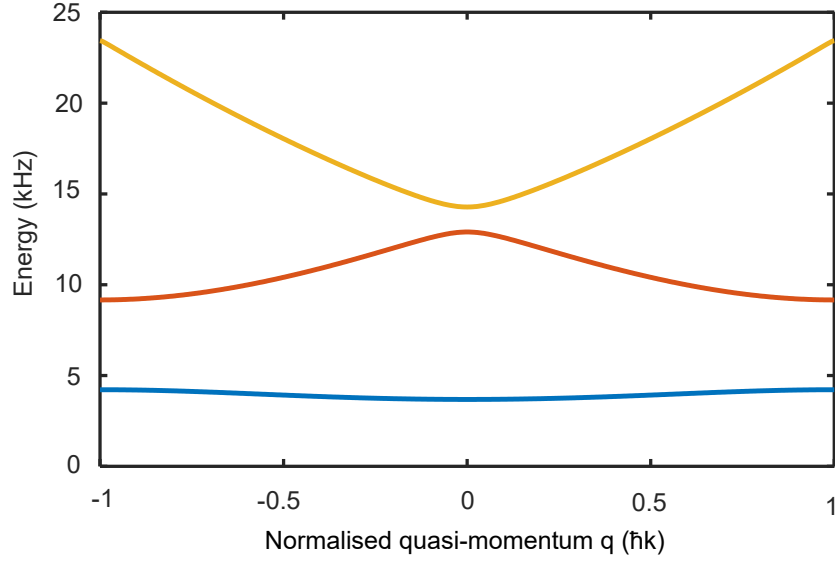


Figure 2.2: **Eigenenergies calculated from Eq.2.17 for a lattice with depth $V_0 = 5E_r$.** The first three energy bands are shown against the normalised quasi-momentum, q , for the first Brillouin zone.

and the optical lattice potential and the Bloch function take the form

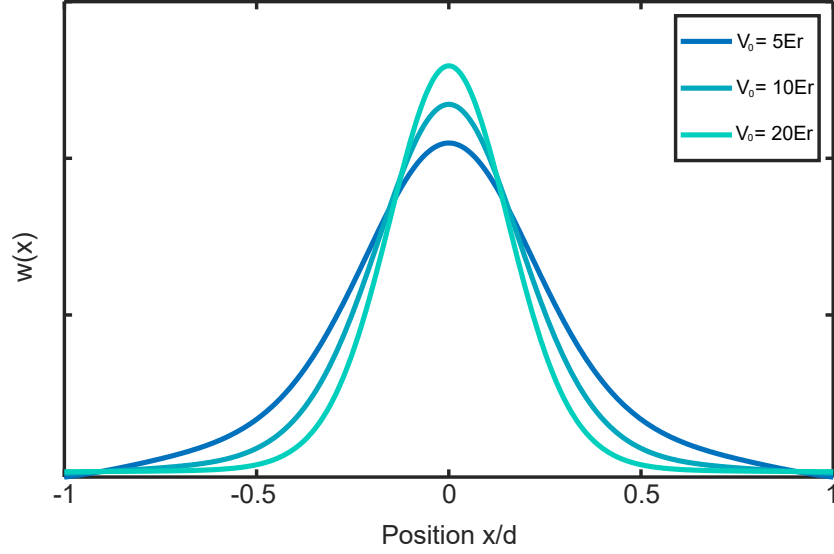
$$V(x) = V_0 \sum_{\nu} e^{i\nu Gx} \left[\frac{1}{2} + \frac{1}{4} (e^{iGx} + e^{-iGx}) \right], \quad (2.15)$$

$$\psi_{n,q}(x) = e^{iqx} \sum_m C_m^n e^{i\nu Gx}, \quad (2.16)$$

where q is the quasimomentum, G is the reciprocal lattice vector and C_m^n are the Fourier components. Substituting the Fourier series into the Schrödinger equations gives

$$\begin{aligned} \left(\frac{\hbar^2}{2m} (q - \nu G)^2 + V_{\nu=0} \right) C_{q-\nu G}^n + V_G C_{q-(\nu+1)G}^n \\ + V_{-G} C_{q-(\nu-1)G}^n = E C_{q-\nu G}^n, \end{aligned} \quad (2.17)$$

where $V_{\pm G} = V_0/4$ and $V_{\nu=0} = V_0/2$ for the given periodic function. We first write the Hamiltonian in matrix form, with the first part of Eq.2.17 on the principal diagonal, and $V_0/4$ on the upper and lower diagonal. The matrix, with dimension $2\nu + 1$, is given


 Figure 2.3: **Wannier functions at different lattice depths.**

by

$$\begin{bmatrix} F_{-\nu}(q) + \frac{V_0}{2} & \frac{V_0}{4} & 0 & 0 \\ \frac{V_0}{4} & \ddots & \ddots & 0 \\ 0 & \ddots & \ddots & \frac{V_0}{4} \\ 0 & 0 & \frac{V_0}{4} & F_{\nu}(q) + \frac{V_0}{2} \end{bmatrix} \quad (2.18)$$

where $F_{\nu}(q) = \frac{\hbar^2}{2m}(q - \nu G)^2$. The sums in equations 2.15 and 2.16 are truncated at $|\nu| = 11$ in our calculations, and matrix dimensions 23×23 . We calculate the eigenfunctions and eigenenergies for values of q between $-\pi$ and π . The eigenenergies form a band structure as illustrated in Figure 2.2 in the case of a lattice with $V_0 = 5E_r$.

For each band, there is only one real Wannier function that is symmetric or anti-symmetric around $x = 0$ or $x = \frac{d}{2}$ and also decays exponentially [24], which is the maximally localised Wannier function. No other phase leads to a faster decay, and are as such not as localised. In order to produce these maximally localised Wannier functions, the even bands ($n = 0, 2, \dots$) are chosen to be real and the odd bands ($n = 1, 3, \dots$) are chosen to be imaginary.

We then calculate the Bloch function by multiplying the eigenfunctions with the phase term and calculate the Wannier functions by taking the integral of the Bloch function with respect to the momentum. The Wannier functions for different lattice depths

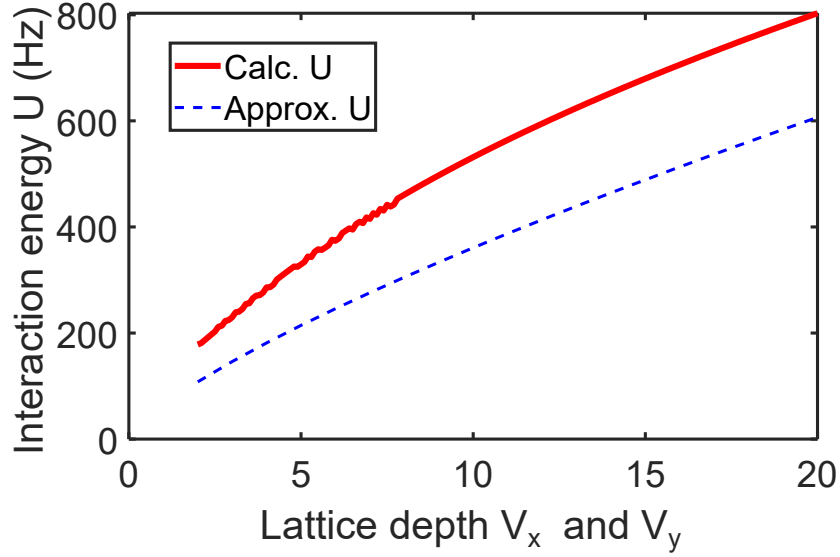


Figure 2.4: **The interaction energy U vs the lattice depth in both V_x and V_y for the calculated U (Eqn. 2.20) and the approximated U (Eqn. 2.23).** The vertical lattice is kept at $V_z = 20E_r$.

have been calculated (Fig.2.3). From these, the interaction energy can be determined as [26]

$$U = \frac{4\pi\hbar a_s}{m} \int |w(x)|^4 dx, \quad (2.19)$$

where a_s is the scattering length. To calculate U for the 3D system, we take the average of the three interaction energies for each lattice. We plot the interaction energy against the lattice depth in V_x and V_y (Figure 2.4). The vertical lattice is kept constant at $V_z = 20E_r$.

The tunnelling term can be calculated using Wannier functions by [26]

$$J = \int w_n(x - x_i) \left(-\frac{\hbar^2}{2m} \frac{\partial^2}{\partial x^2} + V(x) \right) w_n(x - x_j) dx, \quad (2.20)$$

where i and j are neighbouring sites. J can also be calculated from the energy bands (Figure 2.2) by measuring the width of the lowest band

$$4J = \max [E_0(q)] - \min [E_0(q)], \quad (2.21)$$

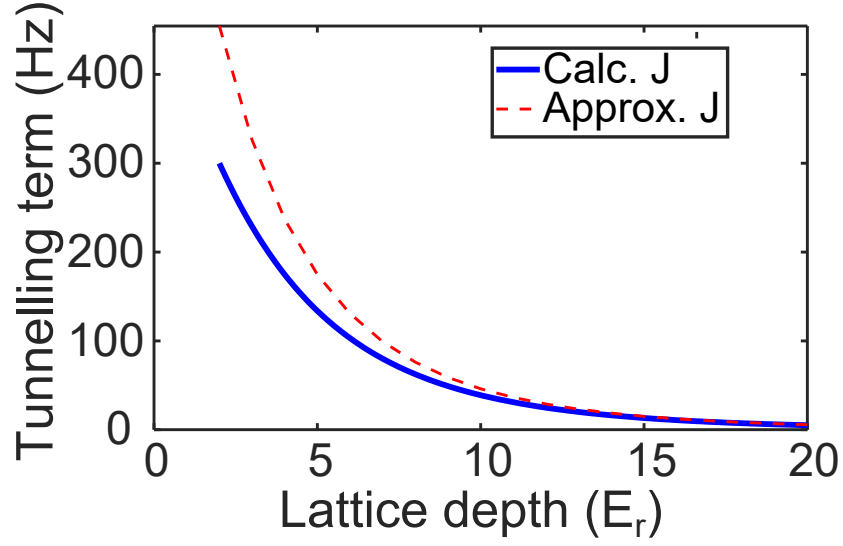


Figure 2.5: The tunnelling term J vs the lattice depth for the calculated J (Eqn. 2.22) and the approximated J (Eqn. 2.24). J decreases exponentially for increasing lattice depth.

which is the method we use for all calculations of J in this thesis.

By taking the Wannier function as the Gaussian ground state of a local oscillator potential, you can approximately calculate U in the limit that $V \gg E_r$ [27]

$$U = \sqrt{\frac{8}{\pi}} k a_s E_r \left(\frac{V_0}{E_r} \right)^{\frac{3}{4}}. \quad (2.22)$$

We show the approximation alongside the previous method in Figure 2.4. J can also be approximated for a deep lattice ($V > 15E_r$) using [5]

$$J = \frac{4}{\sqrt{\pi}} E_r \left(\frac{V_0}{E_r} \right)^{\frac{3}{4}} e^{\left(-2\frac{V_0}{E_r}\right)^{\frac{1}{2}}}. \quad (2.23)$$

Unlike the interaction energy, J is calculated individually for each lattice depth. We plot J against the lattice depth (Figure 2.5) for both the width of the band calculation and the approximation, which shows the exponential decay with increasing depth.

Chapter 3

Experimental setup

In this chapter, we introduce the experimental apparatus and its operation. The majority of the building of the experiment was completed within the thesis works of Dr. Andres Ulibarrena [28] and Dr. Ilian Despard [29], and with Dr. Andrea Di Carli as a post-doc.

3.1 Experiment

Our main vacuum chamber has two sections (Figure 3.1). The first is the ‘MOT chamber’, used for initial cooling and state preparation. The second section, known as the ‘Science chamber’, houses an optical lattice and a high-resolution microscope objective with a numerical aperture, $NA = 0.68$. This objective allows us to image atoms in the lattice with single-site resolution. To load atoms into the MOT chamber, we employ a 2D+ magneto-optical trap (MOT). A Rubidium oven is maintained at approximately 45°C , and a valve controls the amount of rubidium released into the chamber, such that the pressure is kept at about 4×10^{-7} mbar, with a 10l/s ion pump operating at the same time. The 2D MOT chamber is linked to the ultra-high vacuum chamber with a differential pumping tube. The ultra-high vacuum chamber has an ion pump and a titanium sublimation pump that reduces the pressure to 2×10^{-11} mbar.

We use a separate experimental table for most of the lasers in our setup. One of these lasers, called the master laser, is locked onto the $F = 2 \rightarrow F' = 3$ transition of ^{87}Rb using polarisation spectroscopy. This master laser is the reference laser in our

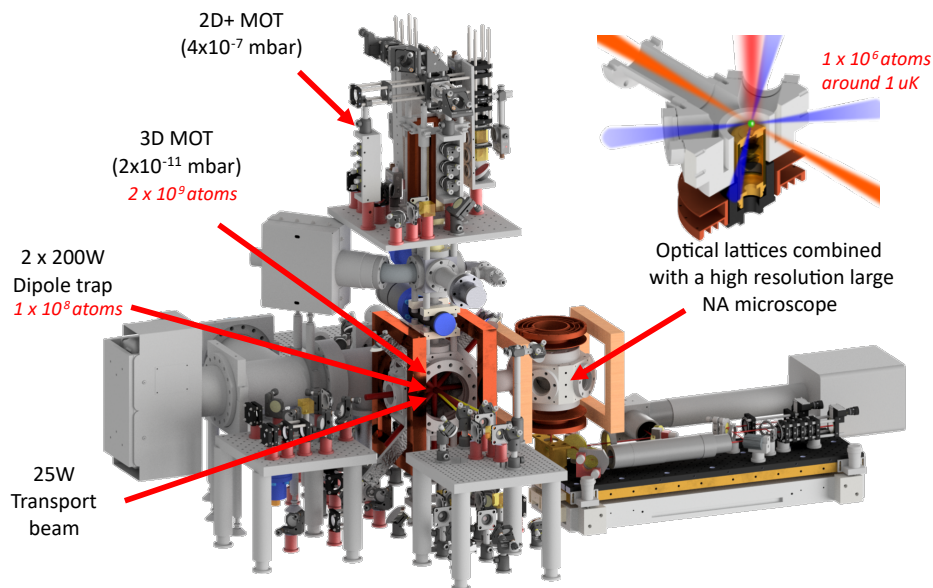


Figure 3.1: **3D render of the experiment [29]**. Starting with a 2D+ MOT chamber that loads the 3D MOT. The atoms are then transferred to the CODT before being transported to the Science chamber where they are first loaded into a CODT and then transferred into the optical lattice.

offset locking scheme for the MOT cooling lasers. The MOT cooling lasers consist of both the 3D MOT and 2D MOT cooling lasers, and a repumper laser. The 3D MOT cooling laser has a total power of 200 mW, the 2D MOT around 350 mW and the 3D MOT repumper 3 mW. The powers and frequencies of the 3D MOT cooling and repumper lasers are controlled using acousto-optic modulators (AOM).

3.2 Initial cooling

Our pre-cooling procedure involves using a 2D+ MOT and 3D MOT to cool atoms down initially before using molasses cooling to bring the atoms down to around $2\mu K$ and then load into a crossed-optical dipole trap (CODT).

The sequence starts with loading 2×10^9 ^{87}Rb atoms from the 2D+ MOT into the 3D MOT. The 3D MOT atom number saturates at 2×10^9 after a loading time of 2s, although we allow for 3s for the loading to achieve a higher reproducibility. After loading the 3D MOT, we turn off the 2D MOT B-field and use the 3D MOT shim fields to slightly reposition the cloud by less than a millimetre within 50 ms prior to molasses

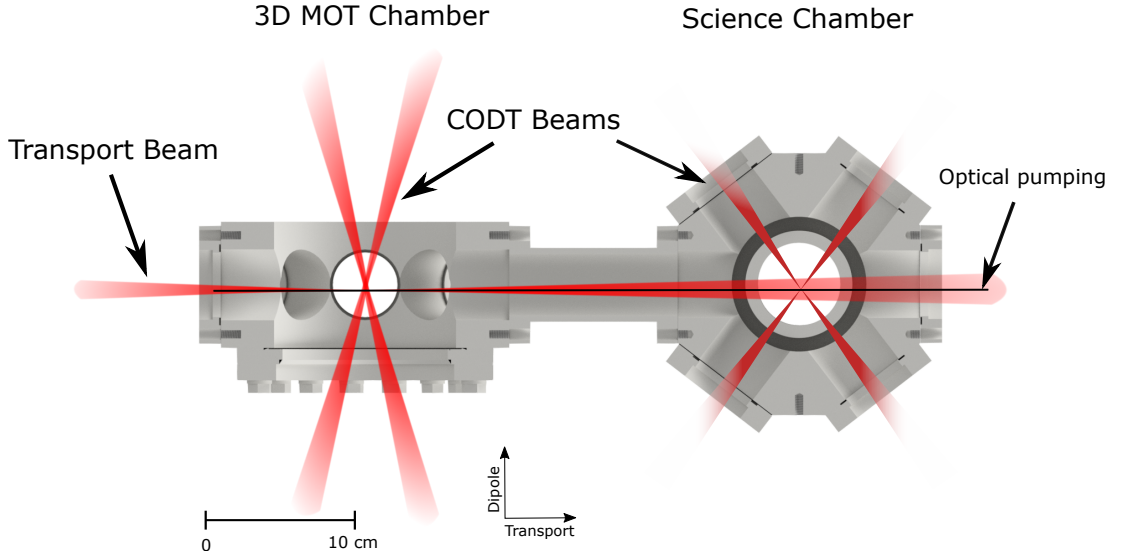


Figure 3.2: **Top-down drawing of the MOT and Science chamber.**

cooling and subsequent loading into the CODT. During the MOT loading phase, the cooling laser is red detuned to the $F = 2 \rightarrow F' = 3$ transition by 20 MHz and the repumper is resonant with the $F = 1 \rightarrow F' = 2$ transition, resulting in a temperature of $\sim 200 \mu\text{K}$. The next step involves compressing the cloud before sub-Doppler cooling and loading into the CODT, as the initial cloud is too large for efficient loading. The magnetic fields are increased linearly from $\frac{dB}{dz} = 15 \text{ G/cm}$ to 30 G/cm in 18 ms while reducing the repumper power by a factor of four. The 3D MOT cooling beam is red detuned by further 60 MHz to 80 MHz in total, and the power increased by 20%. While the compression has no effect on atom number, it heats the cloud up to $300 \mu\text{K}$. We turn on the CODT after compression and then lower the cloud's temperature to $2 \mu\text{K}$, using red molasses followed by Raman gray molasses cooling.

The CODT is made up of two 1070 nm lasers, intersecting at $17(1)^\circ$. The two beams have a waist of $425(5) \mu\text{m}$ and a power of 200 W each. The cooling techniques both require a zero magnetic field. We wait 3 ms to change the frequencies of the cooling laser for the red molasses while at the same time setting the magnetic fields to zero. During this stage, the cooling beam is blue detuned 30 MHz from the $F = 2 \rightarrow F' = 2$ transition while the repumper remains resonant on the $F = 1 \rightarrow F' = 2$ transition. We apply red molasses for 13 ms which cools the cloud down to $10 \mu\text{K}$. We then turn

off the cooling beam and detune its frequency to 10 MHz from the $F = 2 \rightarrow F' = 2$ transition, for the Raman gray molasses. The repumper for the Raman gray molasses is created by an electro-optic modulator (EOM) that generates a sideband at 6.8 GHz to the main cooling beam, which makes the two beams coherent with each other. The molasses is used for 1.5 ms and cools the cloud to around $2 \mu\text{K}$ with around 1×10^9 atoms.

3.3 Optical Pumping

The cloud remains in the CODT for 300 ms for free evaporation. For optically pumping the atoms into the $F = 2, m_F = -2$ state, we apply an offset field of 500 mG. The atoms are optically pumped into the $F = 2, m_F = -2$ state by driving the $F = 2 \rightarrow F' = 2$ transition, with the repumper beam on the $F = 1 \rightarrow F' = 2$ transition. Both beams are circularly polarised to drive the σ^- transition. This process lasts for 1 ms followed by an additional 0.3 ms using just the repumper. The magnetic field is then decreased to 100 mG in preparation for a microwave transfer from the $F = 2, m_F = -2$ state to the $F = 1, m_F = -1$ state. Before the microwave transfer, the repumper is used for another millisecond to remove any atoms left in the $F = 1$ state. The microwave transfer is done by using a rapid adiabatic passage over 10 ms with hyperbolic secant (HS2) microwave pulses [30]. After the microwave transfer, a “blow-out pulse” is used on the $F = 2 \rightarrow F' = 3$ cycling transition, removing the atoms from the trap. After these steps, there are approximately 1×10^8 atoms in the $F = 1, m_F = -1$ state in the CODT.

3.4 Transport

A transport trap with waist $47(5) \mu\text{m}$ is turned on in 200 ms. The transport laser is a 1064 nm wavelength with 12.5 W of power, along the transport axis (Figure 3.2). We spend 200 ms to evaporate the CODT down to 20% of its initial power, which loads the majority of atoms into the focus of the transport trap. The position of the transport trap is changed by 25.8 cm in 1.5 s using a translation stage, to move the atoms from

the MOT chamber into the Science chamber, where the high-resolution microscope objective is located. A piezo mirror is used to precisely position the beam. Initially, it is set such that the optimum number of atoms is loaded into the CODT. Then, during the first 800 ms, it is changed to move the position of the transport trap to overlap with the CODT in the Science chamber. The transport is conducted at a maximum velocity, acceleration and jerk of 180 mm/s, 280 mm/s² and 2×10^4 mm/s³, respectively.

3.5 Science chamber

The atoms are loaded into the Science chamber CODT which is formed by the same beams used for the optical lattice later in the experimental sequence. We have a mirror on a rotation stage that changes the beam path from the CODT configuration to the lattice configuration. At the same time, the B-fields in the Science chamber are turned on. Next, the transport beam power is linearly reduced to zero in 500 ms, resulting in the loading of 3×10^6 atoms into the Science CODT. An offset coil is used to change the B-field in preparation for a microwave transfer to the $F = 2, m_F = -2$ state. First, the atoms are evaporatively cooled in the CODT by exponentially turning the powers down to 20% of their initial power, over 1.5 s. The vertical lattice is then turned on with a hyperbolic tangent function

$$V_z = (U_1 - U_2) \tanh \frac{2t}{\tau} + U_2, \quad (3.1)$$

where U_1 and U_2 are the initial and final lattice depths, respectively, and τ determines the steepness of the ramp. The ramp duration is 300 ms, with $\tau = 100$ ms. This type of ramp allows for the smooth turning on of the lattice beams to minimise excitations through sudden changes in the lattice depth.

The CODT is then switched off in 50 ms, and approximately 1×10^6 atoms are loaded into the vertical lattice. This results in atoms populating 70 anti-nodes of the vertical lattice. Before transferring atoms to the $F = 2$, we drive the $F = 2 \rightarrow F' = 2$ transition for 15 ms to remove any atoms out of the $F = 2$ state. We then wait for 40 ms for the microwave amplifiers to turn on, and transfer the atoms into the $F = 2, m_F = -2$ state

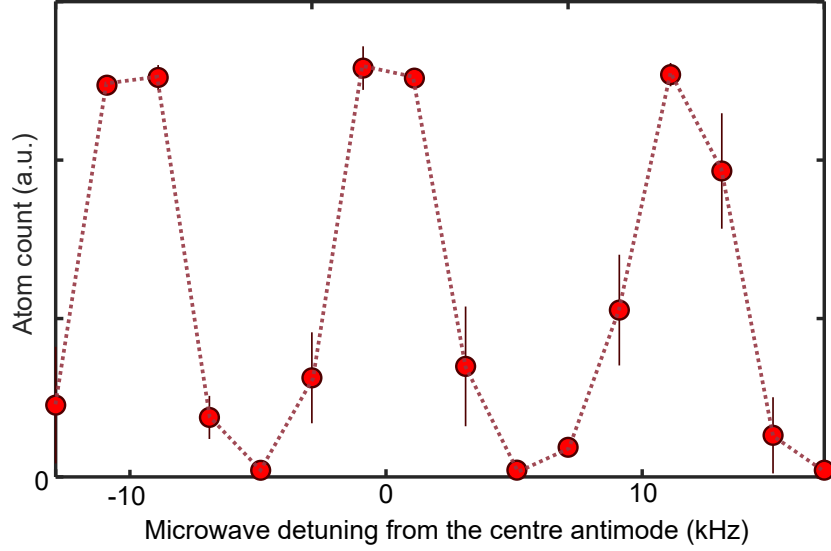


Figure 3.3: **Microwave spectrum for selecting a single anti-node of the vertical lattice.** The frequency is increased in steps of 2 kHz and with a sweep width of 7 kHz. Each antinode in the vertical lattice is separated in frequency by 10 kHz

using the same rapid adiabatic passage used earlier over 10 ms. Following this, we shine in the repumper for 3 ms to remove any atoms that remain in the $F = 1$ state.

3.6 Preparation of a 2D system

The next stage involves selecting a single antinode of atoms in the vertical lattice, referred to as a ‘layer’. We transfer a single layer to the $F = 1, m_F = -1$ and then blowout the other layers. This leaves behind a single 2D system.

We ramp up a strong magnetic field gradient, $\frac{dB}{dz} = 100$ G/cm, to create a spatially selective microwave transfer and subsequently transfer atoms into a single layer to the $F = 1, m_F = -1$ state. The magnetic field gradient results in different energy level splittings between the m_F levels for each layer, allowing us to select different layers of atoms by changing the frequency of the microwave. We then remove the remaining atoms by driving the $F = 2$ to $F' = 3$ transition, leaving a single layer of atoms behind in the $F = 1$ state (Figure. 3.3).

The magnetic field gradient is turned on in 150 ms and held for 140 ms. We use a quadrupole field to generate the magnetic gradient field. We require the field to be

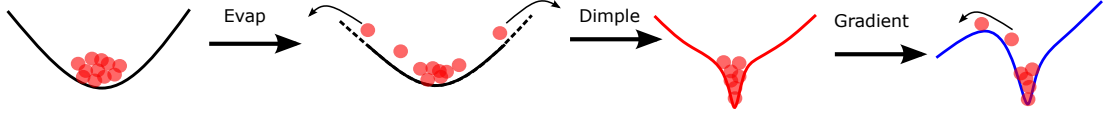


Figure 3.4: **Different stages of the evaporation sequence.** The first stage is the initial evaporation in the vertical lattice. The next stage adds the dimple trap, before then applying a magnetic field gradient. The strength of the dimple allows for control over the final atom number after evaporation.

locally flat on the atoms to select one distinct layer. To make sure that the symmetry axis of the quadrupole field overlaps with the vertical lattice, we need to use the 3D MOT coil and transport shim fields in addition to the science chamber shim fields and offset coil. The quadrupole field is turned on to $\frac{dB}{dz} = 100 \text{ G/cm}$ resulting in a frequency shift of 10 kHz between the antinodes in the vertical lattice.

We use three microwave pulses and blow out pulses to minimise any atoms left over in other layers. Initially, we transfer atoms into $F = 1$ and then blow away any remaining atoms in $F = 2$. We then transfer the atoms to $F = 2$ using the microwave pulse and repump the atoms in the $F = 1$ before then transferring back to the $F = 1$ and blowing away atoms left in the $F = 2$. To find the microwave frequency corresponding to the centre of a layer, we change the microwave frequency in steps of 2 kHz (Figure 3.3). The width of the microwave sweep is 7 kHz which is narrower than the frequency separation between the layers and allows us to find the centre of the layer. Each layer is at a different position with respect to the focal point of the microscope objective. Before every dataset taken in this thesis, this microwave spectrum was used to find the centre of the layer that is in the focal plane of the microscope. After finding the centre, the width of the microwave pulse was changed to 12 kHz to increase the probability of transferring all the atoms in a single layer and to make it resilient to drifts in the experiment, while still being narrow enough to not transfer any atoms in other layers. The B-fields are then ramped down in 50 ms. We keep a field on in the vertical direction, $B = 10 \text{ mG}$, to avoid any mixing of the m_F levels.

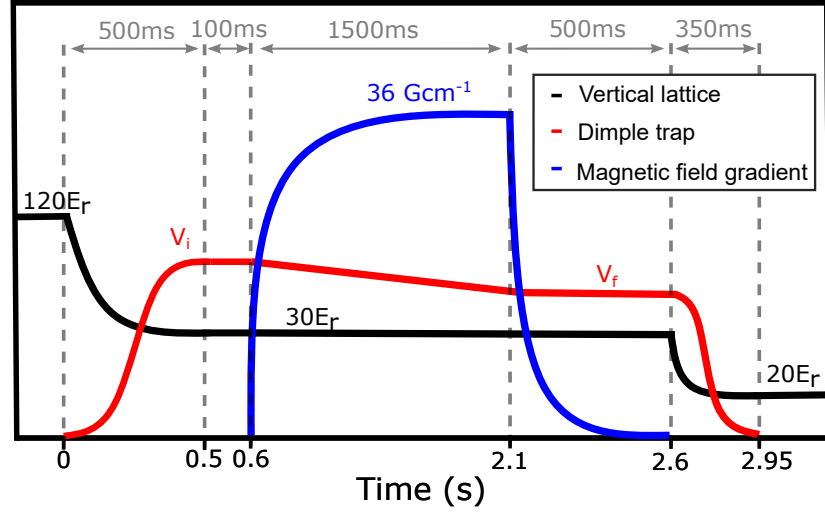


Figure 3.5: **Experimental sequence for the evaporation in a single antinode.** The black line is the vertical lattice depth. The red line is the dimple power and the blue line is the magnetic field gradient. After evaporating in the vertical lattice, the atoms are loaded into the dimple trap. Then the magnetic gradient is ramped on and the dimple power reduced. The field is turned off slowly and then the dimple is turned off and the vertical lattice reduced.

3.7 Cooling to quantum degeneracy

To cool the atoms down towards a Bose-Einstein condensate (BEC), we employ evaporative cooling in a tilted trap, together with a dimple trap with frequency 850 nm. The tilt evaporation method leads to run-away cooling and achieves higher phase-space densities compared to just evaporation through lowering the trap depth [31]. The dimple trap helps achieve higher phase-space densities [32] and reduces the displacement of atoms from the vertical lattice during the tilt evaporation. Figure 3.4 illustrates the different stages of the evaporation process. We first have an initial evaporation stage in the vertical lattice and load atoms into the dimple trap. After this, we apply a magnetic field gradient to tilt the potential.

As the dimple trap laser and the two beams used with the DMD (section 4) are shone through the microscope objective, we need to position the objective before the evaporation, which is different to the position we use for imaging. We take 30 ms to position the objective. After this, we start the evaporation sequence (Figure 3.5), with the vertical (black), dimple (red) and magnetic gradient (blue) ramps displayed. We

load the dimple trap within 500 ms ($\tau = 200$ ms) (Equation 3.1). At the same time, the vertical lattice depth is lowered from $V_z = 120 E_r$ to $V_z = 30 E_r$. The atoms are held within the dimple trap for another 100 ms before we turn on the quadrupole field within 1.5 s to create a magnetic field gradient of $\frac{dB}{dx} \approx 36 \text{ Gcm}^{-1}$, along with linearly reducing the dimple trap power by 20%. The strength of the dimple trap is used to control the atom number after evaporation. We use the vertical shim field to keep the quantisation axis in the vertical direction, while the gradient is ramped on. The quadrupole field is then ramped off in 500 ms and we subsequently ramp the dimple off in 350 ms while also ramping the vertical lattice down to $20 E_r$. The vertical lattice is lowered to reduce the harmonic confinement while remaining strong enough to not lose atoms into other layers. The time taken for this ramp was experimentally determined to produce the coldest clouds (Section 3.11), The temperature is affected by the position of the dimple relative to the vertical lattice which is critical because the further away the dimple is to the centre of the harmonic trap, the more time is needed to ramp down the power to avoid heating of the cloud through mass transport of the atoms. There is then a 30 ms hold time before the horizontal lattice are turned on.

We ramp the horizontal lattices on in 200 ms (Equation 3.1, $\tau = 70$ ms). The ramp time was experimentally determined to produce the coldest clouds by measuring the temperature using radial fits (Section 3.11). The lattice depth determines both the interaction and the tunnelling energy (Section 2.4). We ramp to the strongly interacting regime to form a Mott Insulator, at a lattice depth of $V_x, V_y = 20 E_r$, with the vertical lattice kept at $V_z = 20 E_r$, which gives $U = 800 \text{ Hz}$ and $J = 5 \text{ Hz}$. This is the lattice depth we primarily use to initialise the system and when measuring the temperature. We hold the cloud for 50ms before we start the imaging procedure.

3.8 Imaging

To image the atoms, we first freeze the distribution by ramping the lattices to approximately $V_x, V_y, V_z = 3000 E_r$. We then detect the atoms via fluorescence imaging through the microscope objective. We take a second image after we have turned the

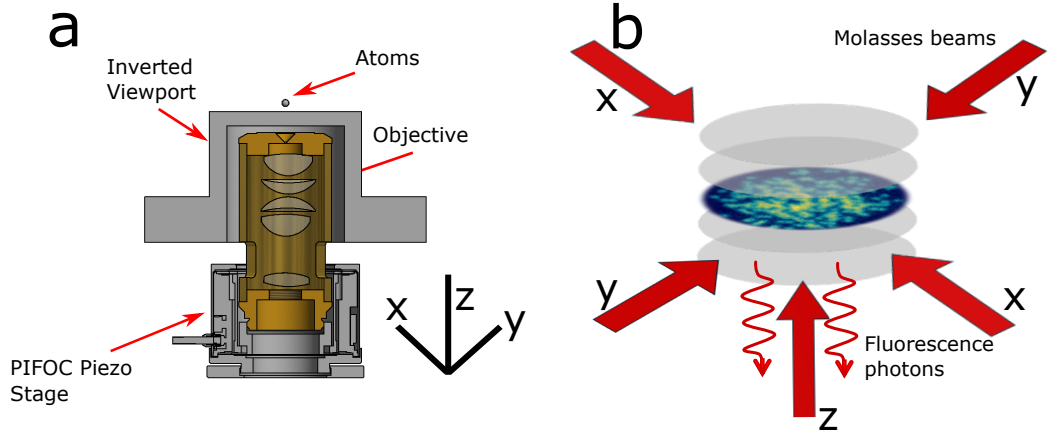


Figure 3.6: **Single atom imaging set-up.** **a**, 3D render of the microscope objective set-up [29]. **b**, imaging the single layer of atoms. The molasses beams are used in all 3 directions and the objective captures fluorescence photons. The vertical molasses only has one single beam going through the objective to the atoms, and not one coming from the top as it would interfere with the imaging.

lattices off and use it as a background image that we subtract from the original image to improve the atom reconstruction process.

To avoid excitations when increasing the lattice depth for imaging, we first increase the lattice depths to $V_x, V_y, V_z = 20 E_r$ and then to $50 E_r$ and finally to $3000 E_r$. Each ramp is linear and the times were experimentally determined by imaging a superfluid in a shallow lattice. If the time to reach $3000 E_r$ is too long, there will be tunnelling that leads to number squeezing and a higher observed atom number will be detected, than expected for a superfluid. If the ramp is too fast then there is heating that leads to atom loss. We found the optimal times for the freezing to be 0.5 ms for the ramps to $20 E_r$ and $50 E_r$. We use 2 ms for the final ramp to $3000 E_r$.

After freezing the distribution, we set the magnetic field to zero within 30 ms in preparation for optical molasses cooling which requires the zero field. Additionally, we also change the frequencies of the molasses cooling beam and the repumper. We then focus the microscope objective on to the imaging plane and wait 50 ms before shining in the molasses. We use optical molasses light to both generate fluorescence light and to cool the atoms to avoid losing the atoms during imaging. We use optical molasses cooling in each direction, with individual control over each power. There

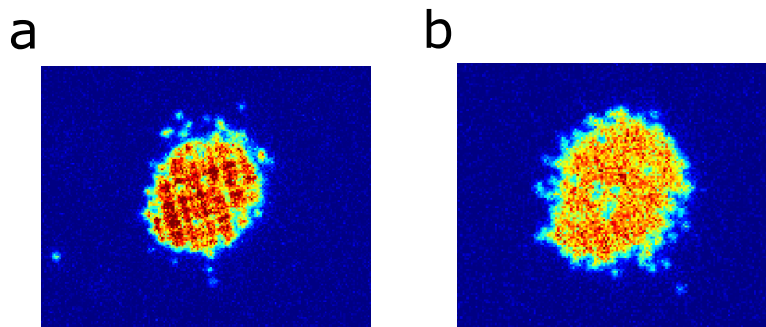


Figure 3.7: **Fluorescence images of Mott insulators with and without modulating the position of the molasses beam** **a**, initial Mott insulator from the imaging set-up. **b**, Mott insulator after quickly modulating the position of the molasses beam.

are a number of factors that affect the imaging including the lattice depth, imaging time, molasses parameters and the magnetic field. The initial imaging process was with 400 ms of imaging time and a 200 ms hold time before taking the background image. The background image has identical parameters, just without the lattice turned on. To optimise the imaging process, instead of taking a background image we take a second image with the lattice still on. By comparing the two pictures to each other, it is possible to see atom losses and hopping events, where the atoms have moved sites between the two images. The aim is to minimise or remove entirely any losses or hopping events during the imaging, while maximising the photon count from each atom. We first optimise the imaging process on a sparse cloud of thermal atoms, and then on a Mott insulator. To find the optimal values for each parameter, we first vary the frequencies of the main cooling beam and the repumper as this has the largest effect on the photon count and losses. After this, we adjust the shim coils while measuring the hopping and losses, to find the true zero field. The next step is to optimise the final lattice depth. If the lattice depth is too low we observe more losses. For increasing lattice depth there is a reduction in the single-atom photon count. To increase the photon count, we increase the power of the optical molasses. Eventually, when the power is too strong, there is an increase in the hopping and losses. We then changed the imaging time, and optimised. We chose an imaging time of 1 s while having minimum atom losses and hopping, with a single atom photon count of 4000 – 8000.

When we image the Mott insulators, we have variations in the fluorescence of the

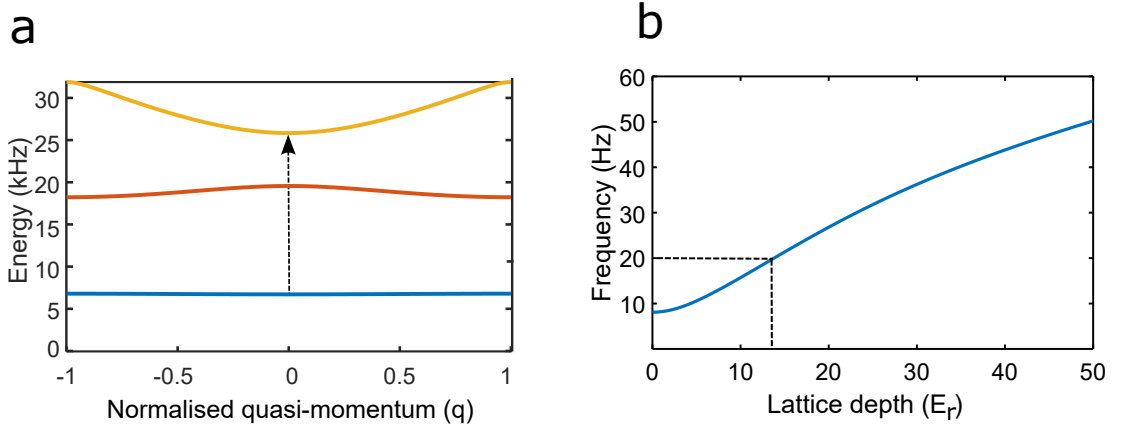


Figure 3.8: **Relation between the lattice depth and the band structure** **a**, band structure for a lattice depth of $V = 13 E_r$. The arrow indicates the energy gap to the second band. **b**, Relation between the excitation frequency and the recoil energy. The dotted line is the same lattice depth as used in the left graph.

images (Figure 3.7a). These differences are likely caused by fringes in the vertical molasses beam from stray reflections from inside the objective. To smooth out the fluorescence, we rapidly move the beam across the cloud using a piezoelectric mirror in the paths of the vertical molasses [33] (Figure 3.7b). The signal we send to the mirror is a triangle wave with frequency $f = 100$ Hz.

We reconstruct the atom occupation from the fluorescence images using the Lucy-Richardson deconvolution algorithm [34]. This involves finding single atoms at the edges of the images and calculating the lattice phase and the fluorescence from a single atom in order to reconstruct the entire image.

3.9 Lattice calibration

We use an intensity regulation process to control the power of the lattice beams. At low lattice depths around $2 E_r$ to $14 E_r$, precise control of the power is important for the superfluid-to-Mott insulator transition, whereas high intensities are used for the CODT and for the fluorescence imaging. To do this, we use a logarithmic photodiode which we calibrate by measuring the real power and the photodiode voltage for specific set voltages on the AOM.

To calibrate the lattice depth vs set voltage, we modulate the intensity of the lattice

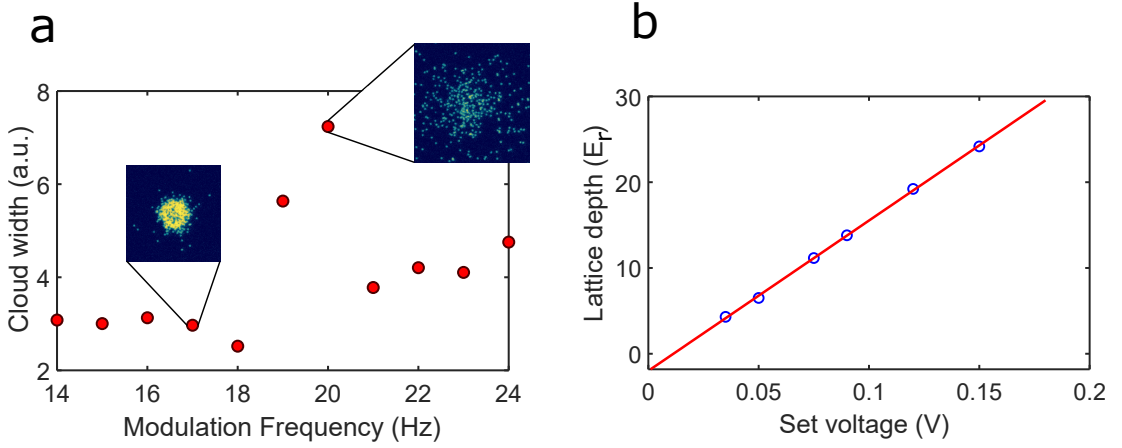


Figure 3.9: **Parametric heating for lattice depth calibration** **a**, The effect of the modulation frequency on the cloud width. When the modulation frequency matches the energy gap to the second band, the cloud is heated and its width increases. **b**, Calibration curve for the set voltage vs lattice depth.

by combining the set voltage sent to the AOM with a radio-frequency (RF) signal from a signal generator. When the modulation of the lattice matches the energy gap to the second band, the atomic cloud becomes excited. We numerically calculate the band structure for a range of lattice depths (Section 2.4), yielding the excitation frequency as a function of lattice depth (Figure 3.8).

Exciting atoms to the second band heats the cloud and we can measure this as an increase of its width (Figure 3.9a). We find the excitation frequency for a range of lattice depths from the weakly-interacting to strongly-interacting regime. We keep the other two lattice depths at $20 E_r$ when calibrating one lattice depth. After calibration, there is a linear relation between the lattice depth and the set voltage (Figure 3.9b). We typically have a 5% error in the calibration.

3.10 Lattice alignment

We need to align the horizontal lattices onto the vertical lattice to avoid mass transport of the atoms towards the horizontal lattices when they are turned on. To align the horizontal lattices with the vertical, we ramp one lattice on to a weak lattice depth ($5 E_r$) and then 100 ms later we turn the other horizontal lattice to a range of values

from $5 E_r$ to $50 E_r$. We measure the position of the cloud for each of the lattice depths. If the position of the cloud changes with increasing depth, the horizontal lattice is misaligned and dragging atoms over to it. We use a piezo-electric mirror to accurately position the lattice beam until the cloud is no longer moving with increasing lattice depth. This is done for both horizontal lattices.

3.11 Temperature

In order to extract the temperature and the chemical potential from the reconstructed image of a 2D Mott insulator, we perform a radial average of the atom occupations (Figure 3.10) and calculate the observed density and its variance [9]. In a Mott insulator, we anticipate a constant density within each shell, with the variance approaching zero. However, at the edges of the shells, non-integer densities and increased variance may be observed due to the superfluid fraction at the edge of the system.

For higher temperatures, the number of holes and doubly-occupied sites increases, leading to a decrease in density and an increase in variance. To measure the temperature and the chemical potential, we fit the density and the variance to the radial average of the atomic cloud using the following equations: [9]

$$\bar{n}_{det}(r) = \frac{1}{Z(r)} \sum mod_2(n) e^{\frac{1}{k_b T} [\mu_{loc}(r)n - E_n]} \quad (3.2)$$

$$\sigma_{det}^2(r) = \overline{n_{det}^2}(r) - \bar{n}_{det}^2(r) \quad (3.3)$$

where n is the density, $Z(r)$ is the partition function, k_b is the Boltzmann constant and $E_N = Un(n-1)/2$ is the interaction energy. In Figure 3.10, we present an example of the temperature fit of a Mott insulator with an $N = 2$ shell. The density approaches zero at the cloud's center, where no atoms are observed due to light-assisted collisions. The density increases towards one atom per site moving away from the centre before it reduces again at the edge of the cloud. Error bars are larger at the centre due to fewer data points in the radial average. For the depicted example, the temperature is $T = 0.121(7) U/k_b$, and the chemical potential is $\mu = 1.243(4)$. Typically, we achieve

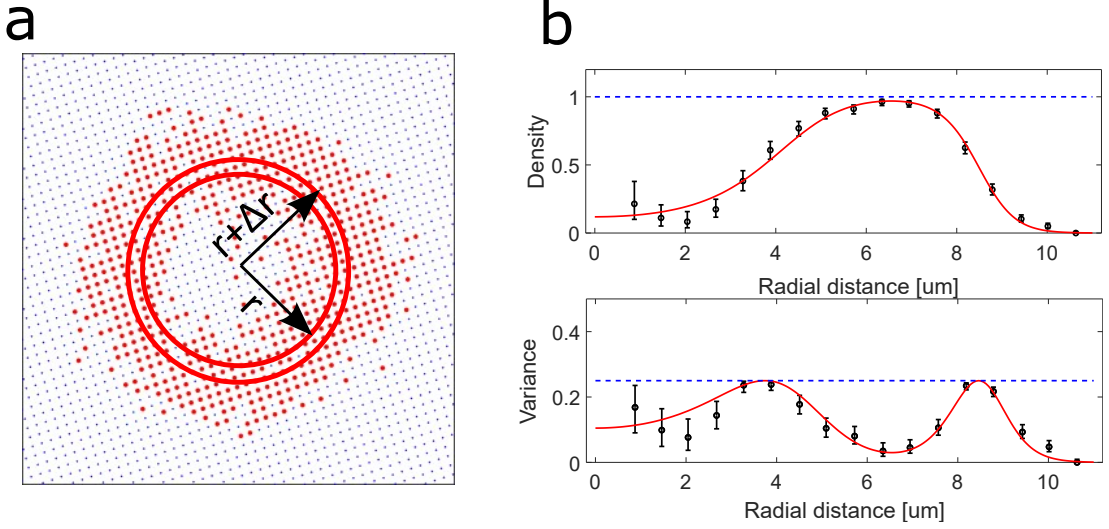


Figure 3.10: **Temperature measurement of a Mott insulator** **a** Reconstructed image of an $N = 2$ Mott insulator. For fitting the temperature, we take the radial average of the cloud by averaging the occupations between r and Δr . **b**, the density and variance fit on the radial average. The temperature extracted from the fit is $T = 0.121(7) U/k_b$ and the chemical potential is $\mu = 1.243(4)$.

temperatures $T < 0.1 U/k_b$ for $N = 1$ Mott insulators.

3.12 Time-of-flight imaging

By using time-of-flight (TOF) measurements you can map the spatial distribution to the momentum [35]. When the horizontal lattices are turned off, the atoms remain in the harmonic potential of the vertical lattice. After the atoms have evolved for one quarter of a period in the harmonic potential [36], we freeze the spatial distribution and this allows us to see the phase coherence as sharp peaks in the interference pattern. When there is no phase coherence, we expect to see no interference pattern.

We turn off the horizontal lattices in less than $50 \mu s$ and let the atoms evolve in the vertical trapping potential for 8 ms. If we ramp slower than $50 \mu s$, we do not see the distinctive phase coherence peaks in the superfluid regime. We determined the time to let the atoms evolve by freezing atoms in the superfluid regime for a range of times. As the system evolves, the atoms move away from the centre in all four directions. The atoms start to come back to the centre because of the harmonic trap. After one quarter

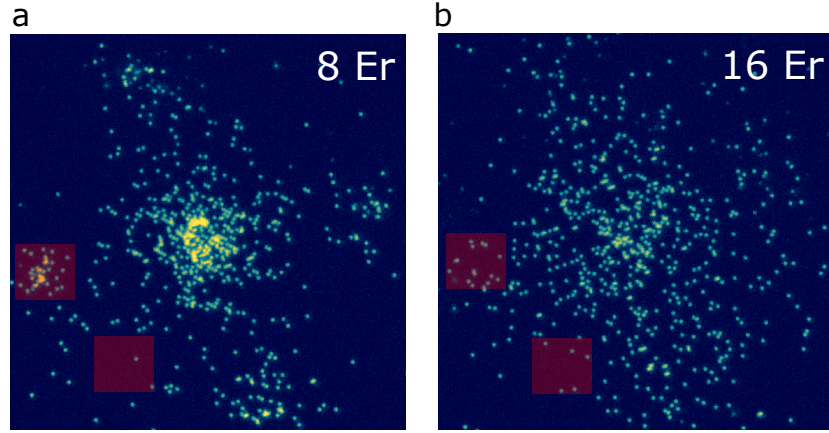


Figure 3.11: **Time-of-flight momentum imaging with the microscope a**, fluorescence image of an atomic cloud at $V_x = V_y = 8 E_r$ after turning the horizontal lattices off and letting the atoms evolve for one quarter of a period in the harmonic trap. **b**, fluorescence image of an atomic cloud at $V_x = V_y = 16 E_r$. The red shaded areas represent the atom occupations used to measure the visibility (Equation 3.4) to quantify the phase coherence in the system.

of a period they are the furthest away from the centre of the trap.

In the superfluid phase, we see four peaks away from the centre along the lattice directions. In the Mott insulator phase we do not see any phase coherence and instead see a sparse cloud of atoms that fills up the Brillouin zone. We measure the atomic distribution of a superfluid at a lattice depth of $V_x = V_y = 8 E_r$ and a Mott-Insulator at $V_x = V_y = 16 E_r$ (Figure 3.11). The visibility of the interference fringes can be measured to determine the level of phase coherence in the system [37]. This allows us to see the phase transition from Mott insulator to superfluid. The visibility is measured by taking the atom number difference from the interference peaks to a region diagonally from the cloud (Figure 3.11), and is given by

$$v = \frac{n_{max} - n_{min}}{n_{max} + n_{min}} \quad (3.4)$$

where n_{max} is the atom count in the phase coherence peak and n_{min} is the one in the diagonal space. When $n_{max} \gg n_{min}$, the visibility approaches one, and decreases as long-range phase coherence is lost. The red shaded areas in Figure 3.11 mark the two areas used for measuring the visibility. The visibility can also be found as the difference

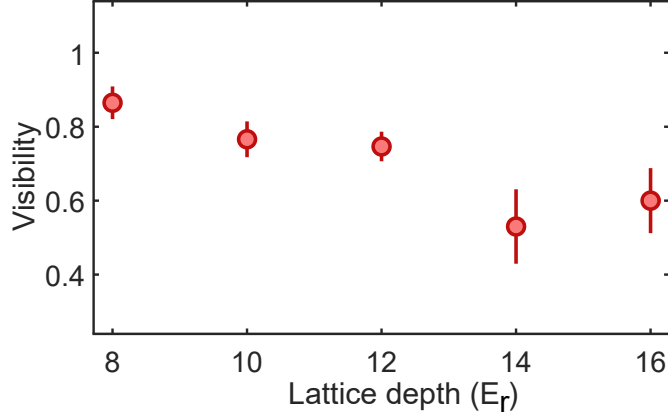


Figure 3.12: **Visibility measurement of the superfluid to Mott insulator transition** The visibility measured for different lattice depths (Equation 3.4). As the lattice depth increases, the visibility decreases.

in the interference pattern, which is calculated using the Green function [37]. A slow changing Green function across the cloud is needed for long-range phase coherence and having a sharp contrast in the density peaks.

The evolution time after turning the lattices off, brings the atoms to the edge of the field of view of the imaging system. There is a higher variation in the single atom fluorescence at the edges of the system as the vertical molasses does not provide a uniform intensity across the cloud, and because of this we see that the four phase coherence peaks are different from each other. To account for this, we only consider one of the peaks when measuring the visibility (Figure 3.11). We would be able to use all four peaks in the measurement if we reduced the time that the lattices are turned off for but the initial measurements were all done with waiting for one quarter of a period in the harmonic potential.

We measure the visibility for a range of lattice depths to show the Mott Insulator to superfluid transition (Figure 3.12). Each data point uses 5 to 10 images averaged to measure the visibility. The fluorescence images are binned in 5×5 pixels before averaging and calculating the visibility. The error bars are calculated by measuring the visibility for each individual image.

3.13 Heating

When we ramp down to the superfluid regime from the Mott insulator and then back, we find that the temperature of the Mott insulator has increased from $T = 0.1U$ to $T \approx 0.2U$. We believe that this is primarily caused by technical noise. We measured the spectrum of the rf from the AOM drivers and found a 12 kHz modulation was caused by the amplifier power inside the driver. To minimise noise on the lattice intensity, we included isolation amplifiers on the control set point before the PI regulation boxes for the AOM drivers and then common mode chokes before the drivers. The isolation amplifiers reduce the ground noise on the set voltage and the common mode chokes were designed specifically to reduce noise around 12kHz.

Chapter 4

Multi-wavelength single-site addressing

In this chapter, we discuss the set-up for making spatial light potentials using multiple wavelengths using the DMD. We will also show examples of the effect of such potentials on atoms in a Mott insulating state. We can make repulsive or state-dependent potentials depending on the wavelength of the light. We discuss the theory behind transferring single atoms to another state and the experimental progress made. We discuss the technique of modifying the optical lattice potential using a blue-detuned repulsive light and how to change these potentials in position and shape within the same experimental sequence. The experimental set-up for the DMD was built together with Dr. Andrea Di Carli and Clemens Ulm, who also worked on the feedback algorithm [38]. Lennart Koehn and Dr. Arthur La Rooij have both worked on the feedback algorithm and on the time-varying potentials.

4.1 Introduction

To be able to explore more exotic systems compared to the 2D square lattice, we require more control over the atoms and the potential. Light shaping has been developed with optical tweezers and with box potentials for cold atoms [39, 40]. We use shaped light incident on the optical lattice to alter the potential or to induce a local differential

light shift on the atoms. Blue-detuned or red-detuned light, projected onto specific lattice sites changes the energy offset ϵ_i . The blue-detuned light will raise the potential of the lattice site, while the red-detuned light will lower the potential. Many models being explored theoretically and experimentally require such control of the underlying potential of the lattice [13, 41–43].

^{87}Rb atoms experience a differential light shift at a wavelength of 787 nm, where the $F = 1, m_F = 1$ state experiences zero light shift. This allows us to spatially address atoms and bring them in and out of resonance with a microwave pulse to transfer specific atoms between the $F = 1$ and $F = 2$ states. This gives the option to create spin impurities in the system [33, 44] and prepare systems with atoms on specific sites which can be important, for example when investigating edge states in the Lieb lattice [41].

To use these potentials with single-site resolution, we use a ViALUX V-9001 DMD. The light is incident on the DMD and then expanded before the microscope objective to give 18×18 mirrors on the DMD per lattice site. This oversampling allows us to precisely control the power on each site. We use light at 666 nm blue-detuned potential for dynamically changing the potential of the lattice, and 787 nm light to create a differential lightshift.

4.2 Multi-wavelength set-up

We make use of two wavelengths incident on the DMD. The path for the two beams is shown in Figure 4.1. The beams emerge from two separate optical fibres and are expanded before the DMD and a dichroic mirror is used to combine them. The beams are expanded such that the light potential covers a large area on the DMD, and covers the entire cloud of atoms. The two beams require different angles of reflection off the DMD to have as much optical power in one diffraction order as possible. To achieve beam overlap after the DMD, only one beam can be in the blazing condition, where a single diffraction order is maximised. Due to the limited laser power available, we chose to set up the beam of the 787 nm laser in the blazing condition. The 666 nm laser beam was not in the blazing condition but positioned to have the first diffraction order

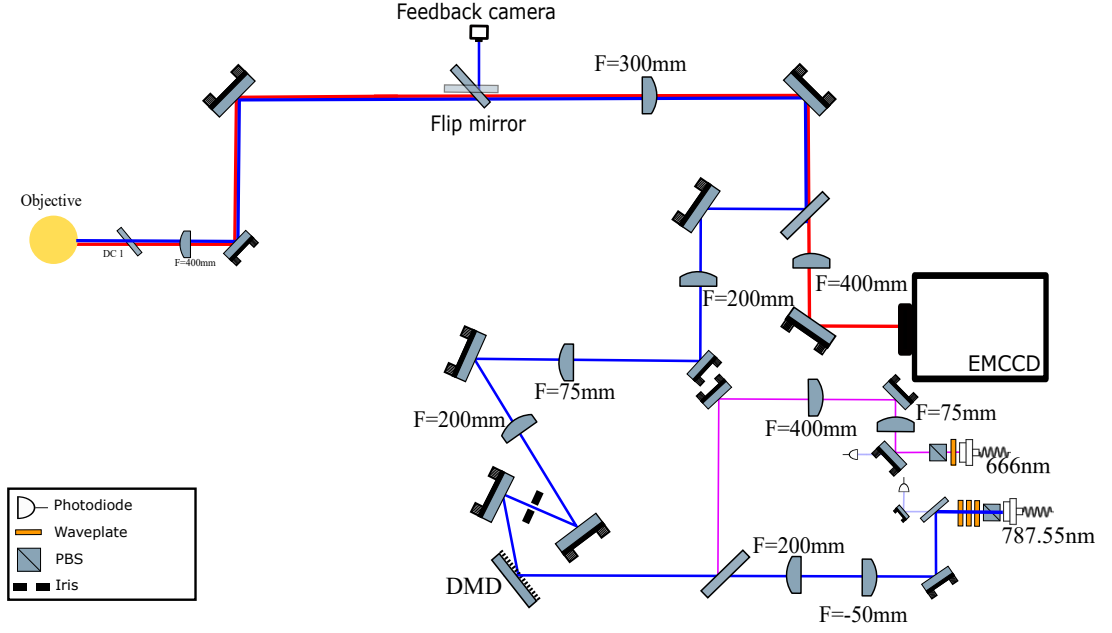


Figure 4.1: **Schematic of the path for the 787 nm and 666 nm beams.** The two beams are expanded separately before hitting the DMD. After the DMD the beams are then overlapped with the imaging path, before they are sent through the objective to the atoms.

in the path of the 787 nm after the DMD [38].

After the DMD, we block the other diffraction orders and then have a pair of lenses to demagnify the beam. The beam then needs to be overlapped with the imaging path, which we do with a dichroic mirror. The imaging path projects fluorescence light from the atoms onto an EMCCD camera. The imaging plane is relayed by a $F = 300$ mm and $F = 400$ mm lens pair. Since there is a $F = 300$ mm lens in the imaging path, before overlapping the beams we include a $F = 200$ mm lens to image the DMD on the first image plane of the relay. After the $F = 300$ mm lens, a flip mirror can direct the DMD light onto a monitor camera, which is placed such that it is in the image focus. This monitor camera is used in a feedback algorithm on the DMD pattern to remove inhomogeneities in the light from the Gaussian beam profile and any aberrations.

The focus of the microscope objective is adjusted so that the images of atoms are in focus on the EMCCD camera. To keep the image displayed on the DMD in focus with the atoms, we need to refocus the microscope objective when using the different wavelengths. To do this, the objective is mounted on a single-axis piezo translation

stage with a $100\ \mu\text{m}$ travel. The $666\ \text{nm}$ beam is used during the evaporation so we optimise the dimple trap, that also goes through the objective and is used during the evaporation, for the objective position needed for the $666\ \text{nm}$ beam. After the evaporation, we reposition the objective for the imaging.

We need to identify which mirrors on the DMD correspond to specific lattice sites of the optical lattice and determine which mirrors align with particular pixels on the monitor camera. To measure the position of the potentials displayed on the DMD to the optical lattice, we display 5 circles and measure the positions of the circles on the atoms. Using this data, we determine the coefficients of an affine transformation that maps the pattern on the DMD to the desired lattice potential. The affine transformation takes the form

$$T = \begin{bmatrix} n_1 & n_2 & 0 \\ n_3 & n_4 & 0 \\ 0 & 0 & 1 \end{bmatrix}, \quad (4.1)$$

which covers translation, rotation, sheer and scale.

We do two separate measurements of the position of the circles for the two wavelengths, as the positions are slightly different. For the blue-detuned light, as it is generates a repulsive potential, we create holes in the cloud of atoms and calculate their positions (Figure 4.2). With the $787\ \text{nm}$ light, we create circles that have an attractive potential for a cloud of $F = 2$ atoms. We take 3 sets of 10 images, where we average the 10 images and then find the centre of the averaged pictures. We then take the average of the three centres and calculate the affine transformation between the co-ordinates on the DMD and the position on the atoms using these 5 points. The transformation is then used to create patterns that are aligned precisely on to the atoms. A pattern is created to be placed on specific lattice sites, and the transformation is then used to calculate the position needed on the DMD.

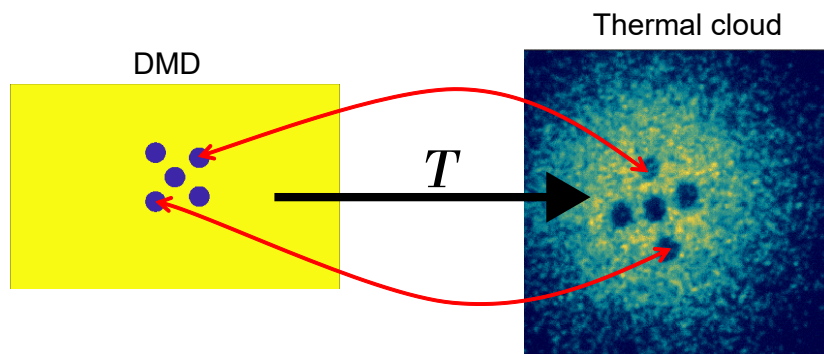


Figure 4.2: **Illustration of the affine transformation from the DMD plane to the atom plane.** The circles are displayed on the DMD and the positions on the atoms are measured. An affine transformation is calculated from the positions on the DMD to the position on the atoms.

4.3 Phase, feedback and dynamic control

We observe a small phase drift of the optical lattices [12] between successive realisations of the experiment, resulting in position shift of approximately $0.05d$ on average, where d is the lattice spacing. This shift corresponds to displacing the pattern on the DMD by a few mirrors. We determine this position shift from the position of single atoms in the fluorescence image, and use it to adjust the position of the DMD pattern for the next measurement to follow the phase drift. In this way the light stays in the same place with respect to the optical lattice, with an estimated deviation of $< 0.05d$.

The DMD's fast refresh rate of $8\mu\text{s}$ allows us to change between different patterns on the DMD dynamically, and combined with the oversampling of mirrors for a single lattice site, this creates the possibility to change between different patterns smoothly and adiabatically for the atoms. We developed a custom software to determine the intermediate DMD frames when specifying the initial and final positions of a pattern. An initial frame is displayed during the system preparation, and after a trigger pulse, a sequence of frames are displayed moving the pattern by a discrete number of lattice sites. It is necessary to program the DMD in 'uninterrupted' mode to suppress the dark time between successive frames. The transition time between frames is $8\mu\text{s}$ during which the mirrors are released and the next configuration of mirrors is switched on. There is a minimum software delay of $100\mu\text{s}$ to swap between frames.

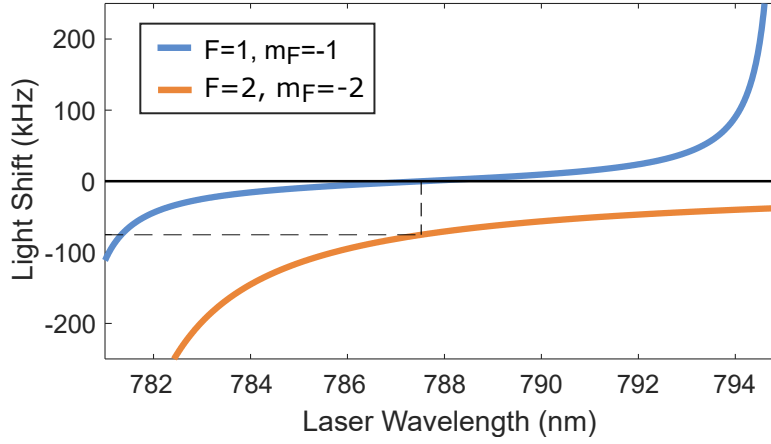


Figure 4.3: **Light shift for $F = 1, m_F = -1$ and $F = 2, m_F = -2$ for wavelengths between the $D1$ and $D2$ lines.** The light shift is calculated for a power $P = 200 \text{ Wcm}^{-1}$. At $\lambda = 787.55 \text{ nm}$ there is zero light shift on the $F = 1$ state.

The DMD is illuminated by Gaussian beams, meaning that the envelope of the shaped light potential still has a Gaussian profile. Using the monitor camera, we can image the light and observe this intensity profile. As we have 18×18 pixels per lattice site, we can remove pixels from areas with higher intensity to make each lattice site have the same intensity. To generate smooth potentials we can use this removal technique in a feedback protocol.

This feedback was not used for the experiments presented in Chapter 5 as small differences in the intensity of the potential barrier did not have an effect for those measurements. The disorder patterns (Chapter 6) require high accuracy between different sites and so the intensity feedback is necessary. The feedback uses 20 iterations, in each of which it takes an image with the monitor camera then adjusts the DMD pattern to make the image closer to a target image [38].

4.4 Addressing beam

An addressing beam is used to generate state-selective potentials where we use light a wavelength of $\lambda = 787.55 \text{ nm}$, which induces a differential light shifts (Figure 4.3). At this wavelength, there is no light shift on atoms in $F = 1, m_F = -1$ state with $\sigma-$ light as there is equal contributions from the $D1$ and $D2$ lines. Atoms in the $F = 2, m_F = -2$

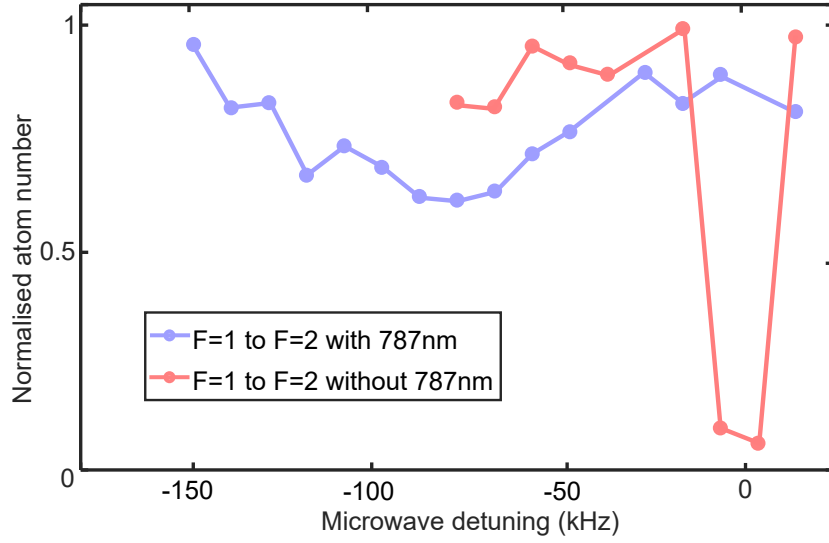


Figure 4.4: **Microwave detuning for the transfer from the $F = 1$ state to the $F = 2$ state with and without the light shift from the addressing beam.** The addressing beam is covering the whole cloud and shifts the transition frequency for all atoms (blue line). As the power is not constant within the cloud, each atom is given a different light shift and the width of the transfer is broadened. Without the addressing beam, the width of the transfer is given by the frequency modulation for the microwave transfer (red line).

state still experience a light shift, and this creates the differential light shift. Atoms illuminated by the state-selective beam will require a different frequency of microwave pulse to flip them to the other hyperfine state.

The light shift is dependent upon the polarisation of the beam. Due to the set-up in the lab, we cannot measure the polarisation of the beam after the last optical element before the atoms. We optimised the polarisation of the addressing beam by measuring the light shift of the atoms, assuming that the shift is maximal for perfectly circular polarisation. We started by applying a light shift to the entire cloud of atoms to measure the overall lightshift on the atoms (Figure 4.4). The first measurement was done without using the feedback algorithm on the intensity. We prepare a Mott insulator at $V_x = V_y = 20 E_r$ in the $F = 1, m_F = -1$ hyperfine level, with every mirror on the DMD active. The addressing beam is turned on adiabatically in 2.5 ms and a 10 ms microwave pulse is applied. The frequency of the microwave pulse is changed to find the transition to the $F = 2, m_F = -2$ level. A blowout pulse on the $F = 2$ to

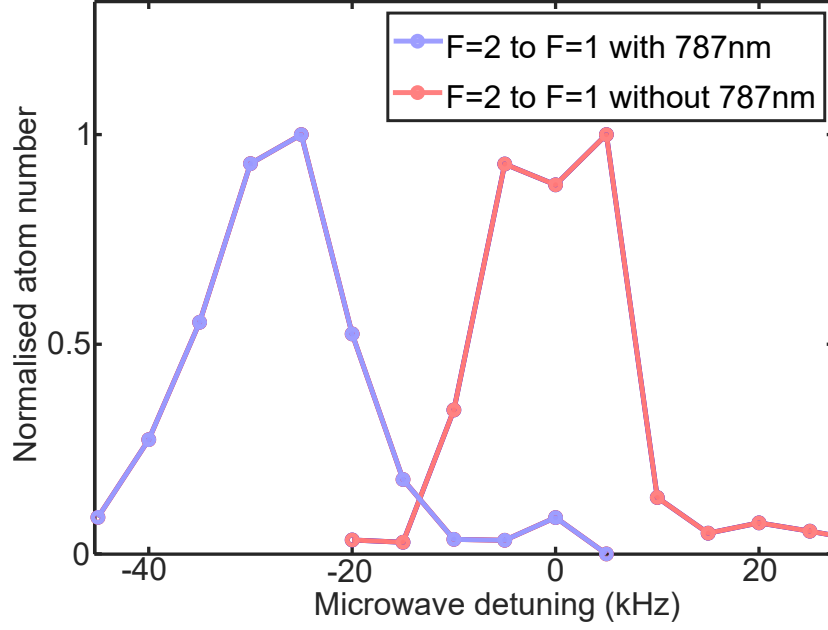


Figure 4.5: **Microwave detuning with intensity feedback on the addressing beam.** The intensity feedback means that the width of the frequency to flip the entire Mott insulator is much narrower.

$F' = 3$ is used to remove transferred atoms. The light shift on the atoms is directly proportional to the intensity of the light. As we did not use the feedback algorithm, the 787 nm light potential has a non-uniform intensity and we do not see a narrow peak for the microwave transition but rather a broad peak (Blue dataset in Figure 4.4) where different areas of the cloud are transferred at different frequencies.

By using intensity feedback to create a beam with uniform intensity, the width of the microwave transfer is narrower as the atoms experience the same light shift. We start with atoms in the $F = 2$ and transfer light shifted atoms into the $F = 1$ and blow away the atoms left behind (Figure 4.5). The feedback takes the light down to the lowest intensity to create a flat profile, meaning that the lightshift is only 30 kHz compared to without using the feedback. Rather than having all the mirrors active on the DMD, we used a square pattern that covers the entire cloud, that is positioned in the highest intensity region of the Gaussian beam on the DMD. The transition with the addressing beam after feedback is shifted by 30 kHz which is far enough that we can target specific lattice sites with the addressing beam and transfer them without

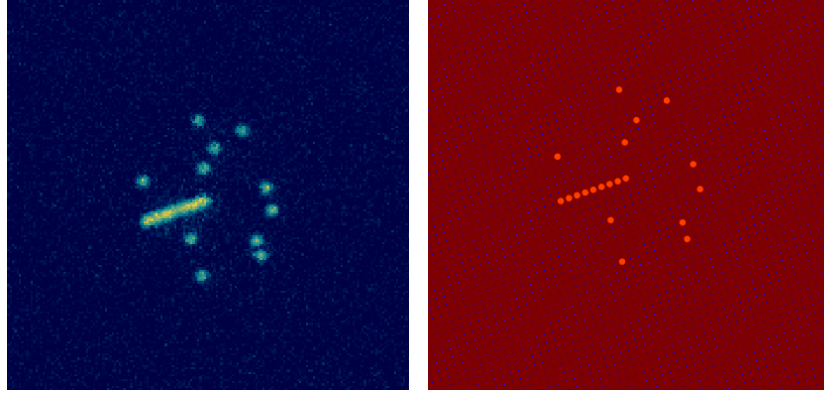


Figure 4.6: **Single line of atoms created using the addressing beam, with the fluorescence image and the reconstructed atom occupation.** We light shift a single-line of atoms in the Mott insulator with the addressing beam and then use a microwave transfer to transfer non-targeted atoms to the $F = 2$ and then remove them using a blowout. The first panel shows the fluorescence from the atoms, and the second panel shows the reconstructed atom occupations.

affecting the other sites.

To check how well we can select specific sites with the addressing beam, we prepare single lines of atoms (Figure 4.6). The sequence for spin flipping atoms started with first making sure every atom in the Mott insulator was in the $F = 1, m_F = -1$ state. We did this by applying a microwave pulse to take all atoms from the $F = 1, m_F = -1$ to the $F = 2, m_F = -2$. We then repumped the atoms in the $F = 1$ on the $F = 1$ to $F' = 2$. After this, we used a second microwave pulse to bring all the atoms back in the $F = 1, m_F = -1$. We then turned on the 787 nm beam adiabatically in 2.5 ms and transfer the atoms that aren't light shifted into the $F = 2$. We then used the blowout beam on the $F = 2$, leaving behind the single line. We are able to prepare single lines of atoms but there are a lot of sparse atoms remaining in the picture which is likely due to an inefficient blowout beam.

Our removal efficiency with the "blowout beam" is around 95%. We speculate that this is caused by atoms falling out of the cycling transition $F = 2, m_F = -2$ to $F = 3, m_F = -3$ and going into the $F = 1$ state. To improve the efficiency, we used multiple blowout processes on the Mott insulator. There still remain a few atoms after the second blowout process, which is likely atoms that have fallen into

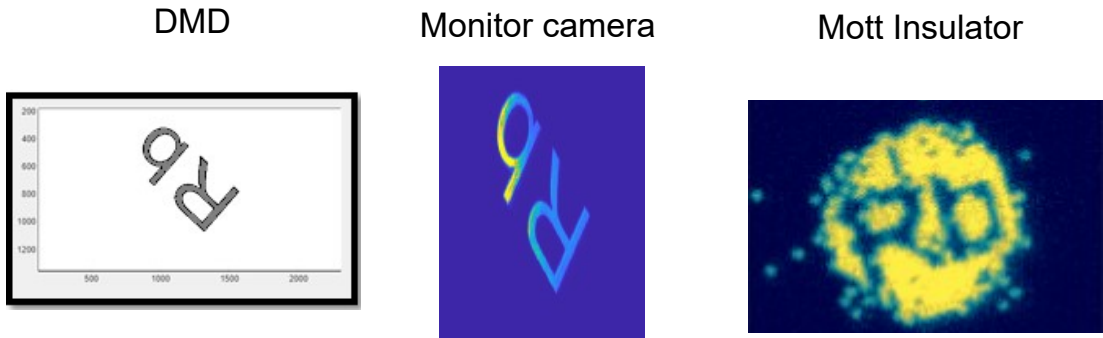


Figure 4.7: **The repulsive potential pattern shown at the three different stages of the experiment.** The image is first displayed on the DMD and then imaged on the monitor camera. The light is then used to shape the potential of the lattice during evaporation and produce the Rb logo in the strongly interacting system.

the $F = 1, m_F = 0$ state, that we did not transfer to the $F = 2$ with the microwave transition.

We test the effect of the lattice depth on the microwave transition with the addressing beam. Starting in the $F = 2$ state, we transfer the entire Mott insulator to the $F = 1$ state and then by blowing away the atoms that were not transferred, we can measure if the lattice depth has an effect on the efficiency of the process. By going to a deeper lattice ($50 E_r$), there is less holes in the Mott insulator meaning that there is a higher transfer efficiency with the addressing beam.

4.5 Repulsive potential

We use blue-detuned light at a wavelength of 666 nm to alter the potential of the optical lattice. When the light is sent to a specific lattice site, it increases the potential of the lattice site. This gives us the capabilities to put potential barriers onto the lattice potential, and create small potential offsets between sites. We first display the pattern on the DMD and then image it on the monitor camera before imaging the Mott insulator (Figure 4.7). We have the 666 nm light on during the evaporation for this image.

We use the repulsive potentials in two different ways. In Chapter 5, we use it without feedback to create potential barriers and in Chapter 6 we use it to generate a disorder

pattern. For the potential barriers, we turn all the DMD mirrors on corresponding to a specific site, as small changes in the potential barrier height do not affect the physics. With the disordered pattern, the differences between the intensity on each lattice site is important so that intensity feedback is needed. This means that not all the mirrors are on, and instead only the central mirrors are used.

It is important to know the strength of the repulsive potential sent to individual sites. For the potential barriers, we want the barrier height to be around $\epsilon = 3U$ and for the disorder pattern we need to know the difference between the highest intensity and the lowest intensity. To calibrate the strength of the light sent to a site, we projected a rectangular light pattern onto the atoms covering 5×4 lattice sites. We started with an $n = 2$ Mott insulator so that when the light shift induced by the repulsive potential is equal to U , you will see atoms in the centre of the $n = 2$ shell and as you increase it to $2U$ you will go back to seeing no atoms. The Mott insulator shell structure is illustrated in Fig. 2.1. The power of the beam was controlled by intensity regulation with an AOM before the DMD. The calibration is shown in Fig. 4.8. The potential depths of the optical lattices were $V_x = V_y = 20(1) E_r$ and $V_z = 35(5) E_r$, such that $U/h = 940(100)$ Hz.

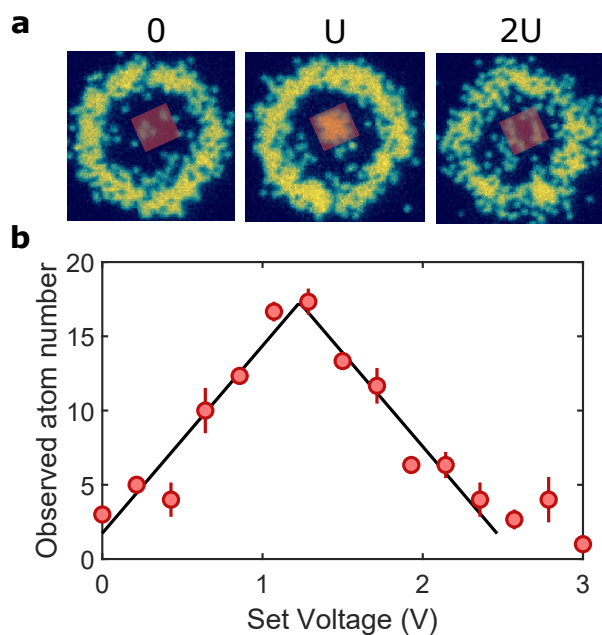


Figure 4.8: **Calibration of the repulsive potential.** **a**, Fluorescence image of atoms in a Mott-insulating state with an inner $n = 2$ shell (visible as mostly empty sites), illuminated with a square repulsive potential in a region of 5×4 sites, indicated by the red square. For the three images, three different intensities of the blue-detuned light were used, corresponding to potential heights of 0, U , and $2U$. **b**, Observed atom number within the region highlighted by the red square in **a**, as function of the set voltage of the laser intensity regulation. Each data point is obtained by averaging the counted atom number in three images, the error bars are standard errors. The peak of the graph represents a potential height U at set voltage of $1.23(8)V$ [45].

Chapter 5

Commensurate and incommensurate 1D interacting quantum systems

This chapter is based on the work published in Di Carli, A., Parsonage, C., La Rooij, A. et al. 'Commensurate and incommensurate 1D interacting quantum systems', *Nat Commun* 15, 474 (2024). The article is cited as Ref. [45].

5.1 Introduction

In this chapter, we make use of the DMD to control the commensurability of bosonic quantum systems by using the dynamic potentials discussed in Chapter 4. Starting with a commensurate system, where there is an equal number of atoms to lattice sites, we reduce the system size while maintaining atom number to deterministically prepare a low-entropy incommensurate quantum state. An incommensurate system is one where the atom number is not an integer multiple of the number of lattice sites. We probe the properties of the incommensurate system from the weakly to strongly interacting regime and explore nontrivial site occupation probabilities in the ground state [46]. Finally, we study the particle mobility of the incommensurate system when subjected to a bias potential.

It is experimentally challenging to control the number of particles in a lattice [47] and the lattice filling, which can dramatically change the properties of the quantum system. The addition or removal of a particle in a commensurate lattice is analogous to doping in semiconductors, and it is relevant to the physics of doped antiferromagnet high- T_c superconductors [48]. Recent experimental studies using quantum-gas microscopes have shed light on the role of doping in Fermi-Hubbard systems [49], by observing bulk transport properties [50–52], string patterns [53], incommensurate magnetism [54], magnetic polarons [55–57], and hole pairing via magnetic coupling [58].

The lattice filling is equally relevant for bosonic many-body quantum systems. In the case of a commensurate particle number, i.e., an integer filling fraction, a homogeneous system can attain a Mott-insulating phase [6, 15], while systems with incommensurate fillings in the strongly-interacting regime cannot form a Mott insulator. Incommensurate fillings have had interesting quantum phases predicted, such as supersolid and crystalline phases in one-dimension [59, 60]. The supersolid phase appears even for short-range interactions in the incommensurate system. In the presence of a disordered potential, the Bose-Glass phase can appear with the incommensurate filling even in the presence of strong interactions [15, 61–63]. Incommensurate fillings have been discussed with defect-induced superfluidity [64], where the removal or addition of a single particle from the commensurate case changes the excitation spectrum from gapped to gapless. Dynamic control over the shape of the light potential using a digital micromirror device (DMD) can be used to prepare incommensurate systems, and has recently been used to stir quantum gases to generate vortices [65–67] and to switch between two optical potentials [57, 58].

5.2 Preparation of (in)commensurate systems

To prepare our 1D commensurate systems, we follow the same experimental procedure described in Chapter 3 up until the final evaporation down to the BEC. Before the evaporation starts, we turn on 666 nm light over 100 ms, that is shaped by the DMD into two potential barriers projected onto the atoms. After this, we evaporate into the

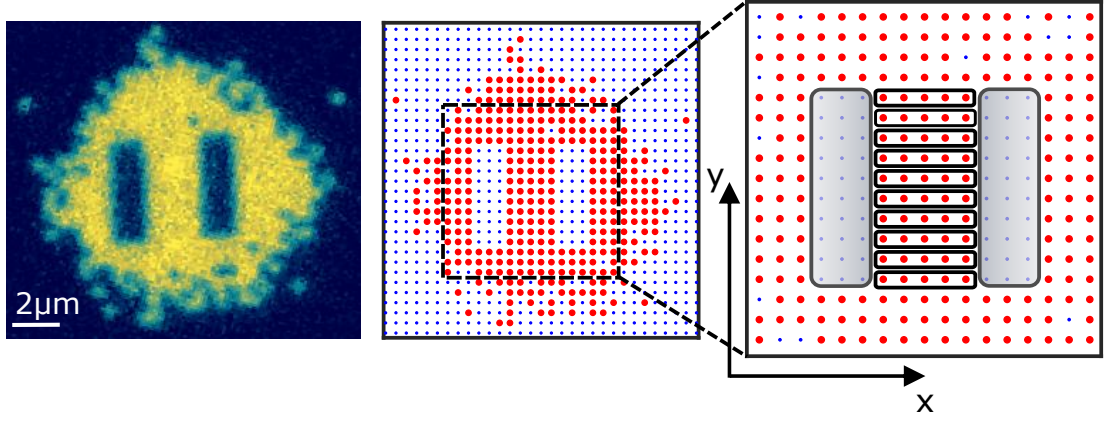


Figure 5.1: **1D system preparation.** a, Left: fluorescence image of a Mott insulator of ^{87}Rb atoms in the presence of two repulsive potential barriers, visible as hollow rectangles in the centre, Middle: corresponding atom distribution. Right: Magnification of the central region, highlighting the individual 1D systems with five atoms and the location of the repulsive potential (grey shaded areas). Figure published in Ref. [45].

potential with the two barriers in place to avoid any heating effects from projecting the barriers later in the sequence. We then change the lattice potential of both horizontal beams from 0 to $V_x = V_y = 50(2) E_r$ within 500 ms. This creates a 2D Mott-insulating state with unit filling between the barriers (Figure 5.1). The potential barriers are positioned such that we have 5 lattice sites between the two barriers. We use $50E_r$ as the lattice depth to initialise the Mott insulator as this is deep enough to avoid tunnelling over the duration of the experiment. The ramp duration to $50E_r$ is 500 ms instead of the 200 ms used when we ramp to $20E_r$ as described in Chapter 3. This was experimentally determined to produce the coldest Mott insulators. During the quantum phase transition from a superfluid to a Mott insulator, the open geometry in the y -direction of the repulsive potential allows for the redistribution of residual entropy towards the outer regions thus enhancing the preparation fidelity in the centre.

The experimental procedure is illustrated in Fig. 5.2a together with a phase diagram in Fig. 5.2b. Initially, our commensurate 1D system in a Mott-insulating state (Fig. 5.2a, panel i) is brought into the superfluid regime (Fig. 5.2a, panel ii). The position of the repulsive potential barrier is then moved to reduce the number of available lattice sites while retaining the atom number (Fig. 5.2a, panel iii). As a result, when the 1D system is brought back into the strongly interacting regime, it can no longer

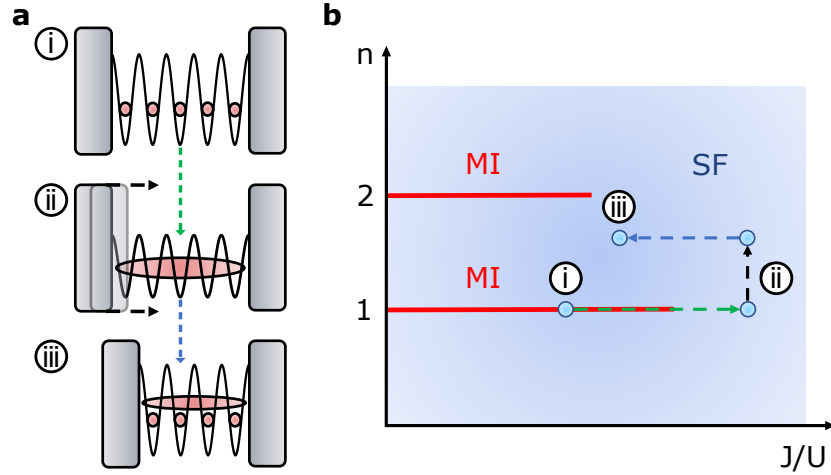


Figure 5.2: **Experimental scenario and phase diagram.** **a**, Sketch of the procedure to generate an incommensurate (doped) 1D quantum system: (i) Initial preparation of a Mott insulating state, (ii) transition to the superfluid regime, and reduction of the number of lattice sites by moving the potential barrier, (iii) transition into the strongly interacting regime. **b**, Illustration of the phase diagram for the 1D Bose-Hubbard model for finite particle number indicating the path followed through stages (i)-(iii). Figure published in Ref. [45].

form a Mott insulator with unit filling, as shown in the phase diagram (Fig. 5.2b).

To characterise the commensurate and incommensurate 1D systems at each stage of the experimental sequence (Fig. 5.3a), we record the on-site atom number parity with the fluorescence imaging (Fig. 5.3b-e), as due to light-assisted collisions we measure the atom number modulus two [9].

We calculate the probability of finding empty sites (sites that had no atom or an even number of atoms) as a function of the lattice site (Fig. 5.3f-i) and a histogram of the number of empty sites (Fig. 5.3j-m) per 1D system. We post-select the datasets by excluding 1D systems (white dashed lines Fig. 5.3b-e) in which the wrong parity is measured or in which an atom is detected at the position of the potential barrier. After this post-selection we retain on average 70% of the 1D systems at the end of the sequence, creating effectively a low-temperature subset of the measured datasets [68]. For all datasets presented in this chapter, we have used the eight central 1D systems between the barriers because of their slightly lower entropy and to discount any possible effects from the edge of the potential barrier. Before taking each data set,

the temperature of Mott insulating systems is measured, following the procedure in Chapter 3.11. We measured the initial temperatures to be $0.10(3)U$. We also measured the temperature of the Mott insulator following the same procedure in Fig. 5.2b but without compressing the system to see the effect of the lattice ramps on the final temperature. The temperature of the clouds rises to around $0.15(5)U$ after the lattice ramps which is the temperature we use for the theory simulations later in section 5.7. The temperature is an upper bound because the effective temperature for the 1D systems is lower as a result of the reduced entropy in the centre region (Fig. 5.1) and the post-selection.

We initially measure the preparation fidelity of five atoms on five lattice sites in the strongly interacting regime. In this scenario with commensurate filling, each atom is localised on a single lattice site. We adjust the position of the bars so that there is not an increased probability to find holes on the edge of the system or atoms on the barrier. This is done without any post selection. We typically take one set of 10 images before adjusting the position of the barriers by changing the displayed pattern on the DMD by 0.1 lattice sites. After this, we measure $96(2)\%$ of the systems with the expected atom number (Fig. 5.3j), and in $4(2)\%$ of the cases we find two empty sites equally distributed across the system (Fig. 5.3f). We attribute these to our non-zero initial temperature and to excitations arising from technical noise.

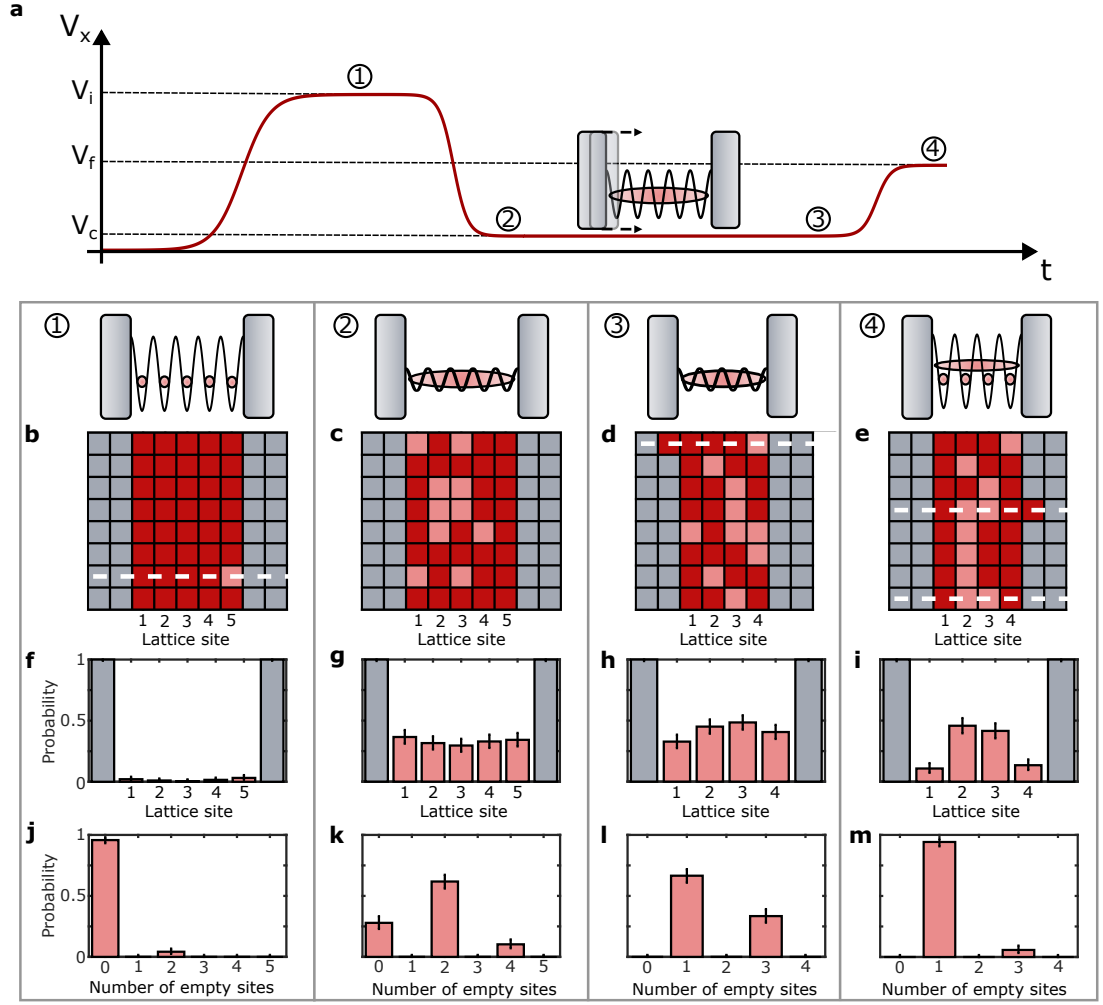


Figure 5.3: **Experimental procedure for doping a Mott insulator.** **a**, Time-dependent variation of the x -lattice potential, V_x . Numbers in circles indicate the stages at which measurements are performed: (1) after preparation of a commensurate system in a Mott-insulating state at $V_i = 50(2) E_r$; (2) after preparation of a superfluid state in a shallow lattice, $V_c = 2.8(4) E_r$; (3) after creating an incommensurate system by dynamically compressing the superfluid, (4) after increasing the lattice depth to reach the strongly interacting regime again, $V_f = 16(1) E_r$. **b-e**, Reconstructed lattice occupation of one experimental realisation, showing the repulsive potential (grey), atoms (dark red) and observed empty sites (light red) that result from both holes and doublons. White dashed lines indicate rows excluded from the statistics by post-selection. **f-i**, Observed probabilities of detecting an empty site. **j-m**, Probability vs number of empty sites for the same system. Each histogram is obtained by averaging over 260-380 independent 1D systems, and all error bars are the 95% Clopper-Pearson confidence intervals. Figure published in Ref. [45].

To enter the superfluid regime, the x -lattice potential is decreased from $V_i = 50(2) E_r$ to $V_c = 2.8(4) E_r$ within 150 ms, thereby increasing J/U . We keep the y -lattice at $V_y = 50(2) E_r$ to prevent tunnelling between the 1D systems. The atoms within the superfluid 1D system become delocalised and due to the atom number fluctuations, we observe an increased number of empty sites which have a uniform spatial distribution (Fig. 5.3g). The boundary effect will reduce the chance of atoms appearing on the edge of the system, but there is an increase in doubly-occupied sites that are more likely to occur in the centre of the trap, making the uniform distribution after imaging. We check that the atom occupations are equally spread over the 5-site system and that there aren't atoms on top of the potential barriers. If there is a higher chance of holes appearing at the edge of the system or that atoms are on top of the barriers, then we again adjust the position of the barriers until the occupation is near flat. We found that the superfluid was more sensitive to the position of the barriers than the strongly interacting regime. After adjusting the barriers with the DMD, we then measured the initial preparation fidelity to check that it had not decreased. After bringing the atoms to the superfluid phase and checking the hole probability is equally distributed, we move the position of one of the potential barriers in 18 discrete steps, within 200 ms. The system size is reduced to four sites while retaining the five initial atoms per line, creating a doped system with incommensurate filling. As a consequence, we observe an odd number of empty sites (Fig. 5.3l) and check that the atom occupation is not asymmetrical after moving the wall in or that there is a chance of atoms on top of the wall. Then, the x -lattice potential is increased to $V_f = 16(1) E_r$ within 200 ms to bring the incommensurate systems back into the strongly interacting regime, leading to the suppression of holes (Fig. 5.3m). The distribution of empty sites, which now correspond to sites occupied by two atoms, shows a higher probability on the central two sites (Fig. 5.3i). The occupation of the central sites is energetically favourable due to the boundary, as predicted by our simulations of the single-band Bose-Hubbard model (see section 5.7).

We verified that compressing the quantum gas in the superfluid regime using the dynamic DMD potential does not result in significant atom loss when using a 'frame

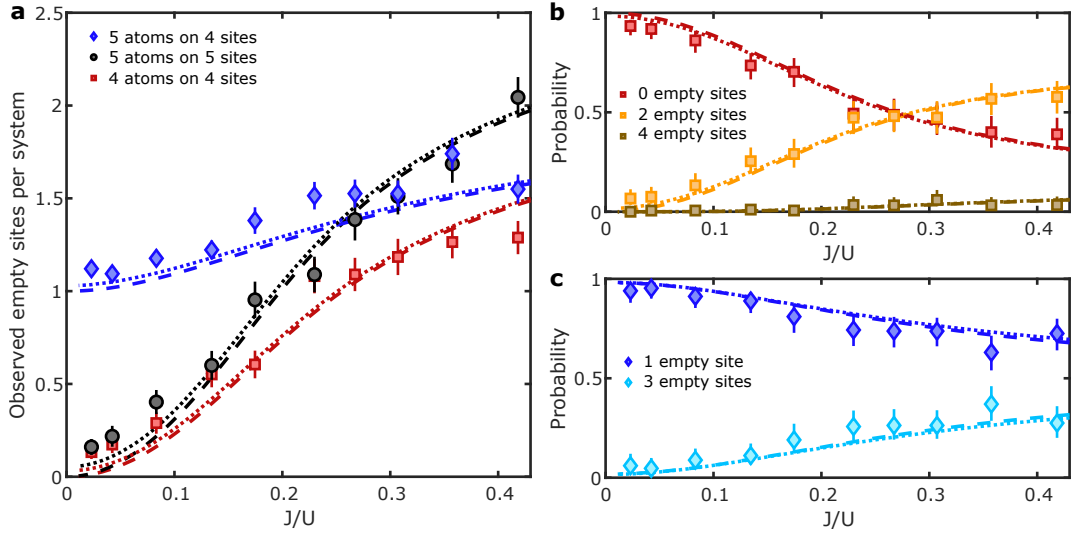


Figure 5.4: **Strongly and weakly interacting commensurate and incommensurate 1D systems.** **a**, Number of empty sites per 1D system vs J/U for 5 atoms on 5 lattice sites (black circles), 4 atoms on 4 sites (red squares), 5 atoms on 4 sites (blue diamonds). Observed empty sites result from both holes and doublons. Error bars show the standard error. Our numerical simulations show the number of empty sites for $T = 0$ (dashed lines) and for $T = 0.15U$ (dotted lines). **b**, Probabilities of zero (red), two (orange) and four empty sites (brown) per 1D system vs J/U in a commensurate system with 4 atoms on 4 sites. **c**, same for an incommensurate system with 5 atoms on 4 sites, showing the probabilities of finding one (blue) and three (cyan) empty sites. Each data point is obtained by averaging over 110 – 190 independent 1D quantum systems, and error bars in **b** and **c** are the Clopper–Pearson 95% confidence intervals. Figure published in Ref. [45].

duration’ of 10 ms. To quantify the atom losses, we reverse the position of the repulsive potential barriers to its original position over the same timescale as for the compression, then transfer the system back into the Mott-insulating state. We found that with static barriers we detected on average 4.81(5) atoms on five sites, while when moving and reversing the potential barriers we detected on average 4.64(7) atoms. We also tested 5 ms frame durations and having only 10 frames per lattice site instead of 18 and found no statistically significant difference experimentally.

5.3 Strongly and weakly interacting systems

We study the difference between an incommensurate and commensurate 1D system when transitioning from the weakly to the strongly interacting regime. Specifically, we prepare an incommensurate system with five atoms on four lattice sites, and compare it to one with commensurate fillings of five and four atoms on five and four sites, respectively (Fig. 5.4a). We use the same experimental procedure to prepare the commensurate and incommensurate systems, the only difference being that repulsive barriers are not moved for the commensurate ones. The number of observed empty sites is compared to our numerical simulations (Section 5.7), taking into account the time-varying potential during the entire experimental procedure, for both $T = 0$ and $T = 0.15 U$ (Fig. 5.4).

In the strongly interacting regime, $J/U \ll 1$, we observe on average less than 0.2 empty sites in the commensurate system, as it attains a Mott-insulating state. In contrast, in the incommensurate system, we observe close to one empty site (Fig. 5.4a), due to the appearance of a doubly occupied site resulting from one delocalised atom on a localised background. As we increase J/U to enter the weakly interacting or superfluid regime, the number of observed empty sites increases in all three cases, in good agreement with the numerical simulation. Using the same data sets, we evaluated the probabilities of detecting empty sites in each 1D system (Fig. 5.4b and c). As J/U is increased, we observe that for the commensurate system with 4 atoms on 4 sites, the probability of observing zero empty sites decreases below 0.5 while the occurrence of two empty sites increases accordingly. This is well captured by the numerical simulation that take into account the intensity ramps used to change the lattice depths. In the case of incommensurate filling, the increase in the observed number of empty sites is less pronounced, as the expected number of empty sites per 1D system in the superfluid is only ≈ 1.6 at zero temperature.

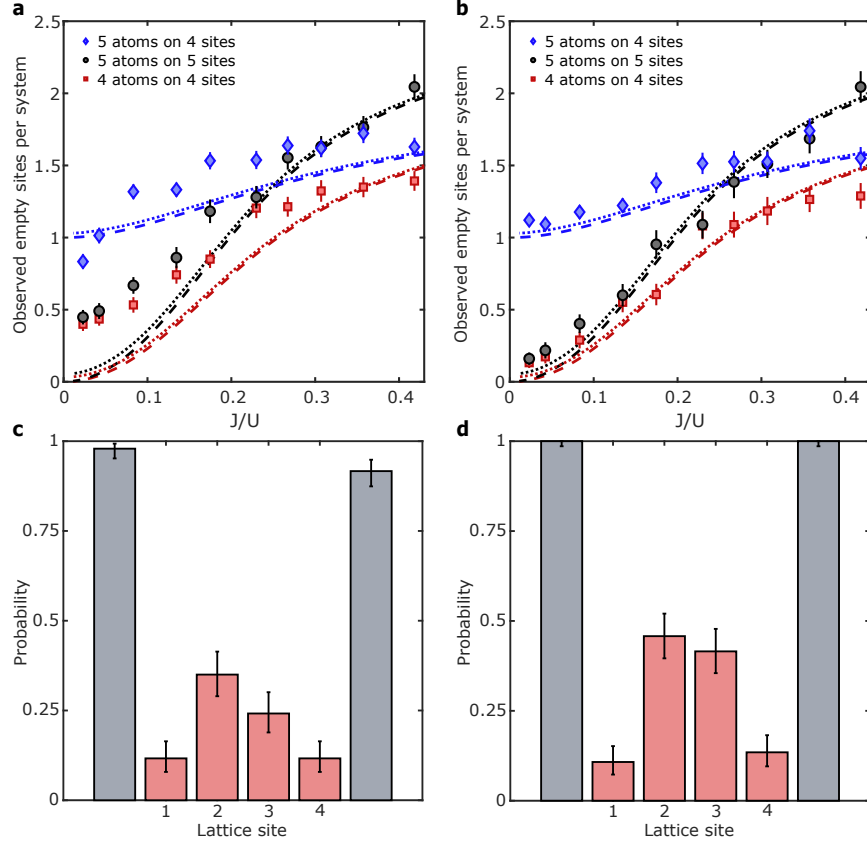


Figure 5.5: **Effect of post-selection.** **a**, Datasets of Fig. 5.4a, but without post-selection, **b** same datasets with post-selection for comparison, **c**, probability of detecting empty sites for 5 atoms on 4 sites without post-selection (datasets from Fig. 5.3i), **d** same datasets after post-selection. Figure published in Supplementary Information of Ref. [45].

5.4 Effect of post-selection

We show the effect of post selection on the hole histograms and the data used to study the weakly to the strongly interacting systems (Figure 5.5). The effect can be seen clearly in the strongly interacting commensurate systems, where an additional atom or hole both lead to an increase in the observed atom number. In the incommensurate system, a loss of one atom leads to a decrease in the observed empty sites while an extra atom increases the number of observed empty sites. These two results mean that the effect of the post selection is not as clear. Fig. 5.5c shows the distribution of empty sites in the incommensurate strongly interacting system without post selection. The

asymmetry in the centre of the system, where there is a higher chance of a doublon on site 2 over site 3, matches with the higher chance of finding an atom on the right wall. The increase of atoms on the wall is likely due to phase drift throughout the dataset which effected the dynamic wall more than the static wall. The post selection decreases the asymmetry in the system and creates a sharper contrast between the central and outside sites. For Fig. 5.5c, atoms on the barrier accounted for 5% of the datasets. Later, when we apply a bias potential to the incommensurate system (datasets shown in Fig. 5.9), this rises to around 20% at the maximum potential gradient. We also investigated post-selection based on a temperature measurement from the outside of the cloud, but found no correlation between the temperature and the parity of the 1D systems.

The fidelity of our initial system preparation is such that we observe zero empty sites in typically 75% of cases, an incorrect parity in 20% of cases and two empty sites in 5% of cases. After the whole experimental procedure (Step 4 in Fig. 5.3a), we find that the observed parity is wrong in 25%-40% of the cases, which we attributed to loss of two atoms and particle-hole pair excitations due to heating from intensity noise of the trapping lasers, especially during the intensity ramps. As the parity is conserved with two-atom loss, it is not detected in the post-selection. Assuming that the probability to lose an atom in our 1D systems is around 30%, then the probability of losing two atoms is close to 10%.

We also find that the incommensurate systems require more post-selection indicating the system is more susceptible to losses which we attribute to the fact that these systems have a non-gapped excitation spectrum and are more susceptible to technical noise. Overall, we retain approximately 70% of systems for the data sets shown in Fig. 5.4. For the experiments presented in Fig. 5.6, when we compress the system by more than one site, we retain on average 60% of the datasets. When applying the bias potential in Fig. 5.9, we find that about 55% of the incommensurate systems have the correct parity, and 60% – 75% for the commensurate systems.

5.5 Atom number, variance and site occupations vs density

The specific number of atoms and sites available in an incommensurate system can lead to non-trivial ground-state occupations that depend on the system size. We have so far considered 5 atoms on 4 sites, and we now compare different incommensurate states with 4, 5 and 6 particles to a Mott insulator with unit or double site occupancy in the strongly interacting regime. For each 1D system, we evaluate as a function of the average particle density, n , the detected atom number normalised by the number of sites before dynamic compression, \tilde{N} , (Fig. 5.6a). We also calculate the variance, σ , from the mean atom number parity (Fig. 5.6b). When compressing the system by two sites, we move both potential barriers in by one site rather than moving one barrier in by two sites. We experimented with moving just one barrier but found that it lead to increased atom loss and asymmetrical distributions. We attributed this to needing more time than we used to compress the system across both sites than thought to remain adiabatic. As expected, we observe Mott-insulating states with $n = 1$ (4 atoms on 4 sites), where $\tilde{N} \approx 1$ and $n = 2$ (4 atoms on 2 sites), where $\tilde{N} \approx 0$, as doubly occupied sites are detected as empty sites due to light-assisted collisions. We saw an increased loss of parity when compressing 4 atoms down to two sites and a higher than expected variance. To reduce the loss, we tried different final lattice depths and found that only when going to $12 E_r$ we saw a lower parity loss compared to the $16 E_r$ we have used for the other datasets. This suggests that the increased losses arise during the lattice ramps that can more easily excite this system, or because the barrier height has less difference energetically to the $n = 2$ Mott insulator compared to the $n = 1$. The observed atom number decreases with increasing density, in agreement with our numerical calculations for the ground states at $T = 0$ indicating adiabatic state preparation. The variance, σ , is a measure for the compressibility for short-range density fluctuations [69]. The compressibility shows how the density responds to a local change in the chemical potential so that if the variance in the density is very low in the harmonic potential then so is the local compressibility. The variance is lowest at integer

densities in the incompressible Mott-insulating state. It attains its maximum value of $\sigma = 0.25$ for non-integer densities [9]. Light-assisted collisions mean that for large fluctuations in the atom number, the density tends to $n = 0.5$, which gives the variance a maximum value of $\sigma = 0.25$. This is in agreement with the numerical calculations at zero temperature (Fig. 5.6b).

The numerical simulations (Section 5.7) have been developed together with Dr. Callum W. Duncan and Prof. Andrew J. Daley based on experimental parameter that the experimentalists provided [45]. The numerical simulations compute the full wave function by exact diagonalisation [70], and for comparison with the experimental results we calculate the local parity operator, \hat{s}_i , of the i th site,

$$\hat{s}_i = \frac{1}{2} \left[(-1)^{\hat{n}_i} + 1 \right], \quad (5.1)$$

with the local number operator \hat{n}_i . We use the lattice occupation to measure the parity of the atom number at a single lattice site, $s_i = \langle \hat{s}_i \rangle$, and the mean atom number parity on M lattice sites, $\bar{n} = \sum_{i=1}^M s_i / M$, where M is given by the size of the 1D systems multiplied by the number of realisations. From this, we calculate the variance of the atom number via $\sigma = \bar{n}(1 - \bar{n})$, shown in Fig. 5.6b.

In the case of two additional atoms on a localised background, the symmetry of the system plays an important role. For 5 atoms on 3 sites ($n = 5/3$), it is energetically unfavourable for both additional atoms to be on the same lattice site. We observed that doubly occupied sites have a higher probability to be found on the outer sites compared to the central site (Fig. 5.6e). The state $|2, 1, 2\rangle$ is favourable, see Fig. 5.7b, as it couples to both $|1, 2, 2\rangle$ and $|2, 2, 1\rangle$, reducing the kinetic energy of the ground state, which is analytically given by $\frac{1}{\sqrt{2}} |2, 1, 2\rangle + \frac{1}{2} |1, 2, 2\rangle + \frac{1}{2} |2, 2, 1\rangle$ in the limit of $U/J \rightarrow \infty$. This state is robust against the presence of a weak harmonic confining potential and the small offsets from the adjacent potential walls. This is in contrast to the state with 6 atoms on 4 sites ($n = 6/4$), for which we observe the additional atoms mostly on the inner two sites (Fig. 5.6d). Specifically, out of the systems post-selected to have two empty sites, we observe the empty sites (corresponding to sites with two atoms) next to each other in 76(7)% of the cases. In 55(7)% of the cases the

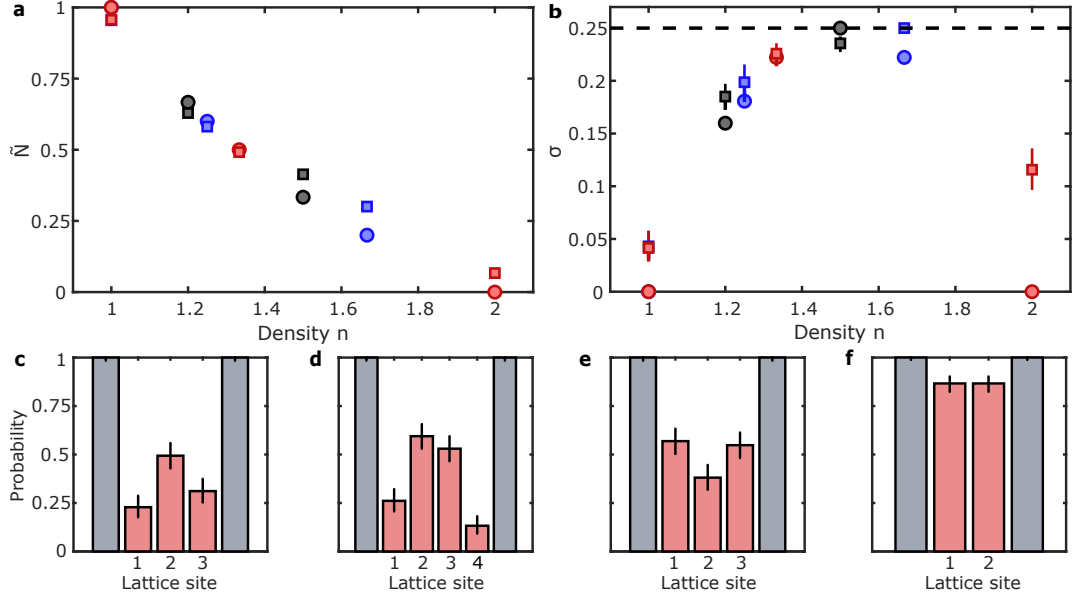


Figure 5.6: **Atom number, variance, and site occupation of commensurate and incommensurate systems.** **a**, Observed atom number normalised by the initial number of atoms, \tilde{N} , vs density, n , for systems of 6 atoms prepared on 6 sites dynamically compressed to 5 and 4 sites (black), 5 atoms on 5 sites compressed to 4 and 3 sites (blue), and 4 atoms on 4 sites compressed to 3 and 2 sites (red). Experimental values are shown as squares, theoretical ones as circles. The statistical errors of the experimental values are smaller than the size of the datapoints. **b**, Atom number variance, using the same densities as in **a**. **c-f**, Site-resolved probability to detect an empty lattice site with increasing density, for 4 atoms on 3 sites, 6 atoms on 4 sites, 5 atoms on 3 sites and 4 atoms on 2 sites, respectively. Error bars in **b-f** are the 95% Clopper-Pearson confidence intervals. Figure published in Ref. [45].

two empty sites are in the centre, corresponding to the observation of state $|1, 2, 2, 1\rangle$, see Fig. 5.7a. Unlike the $n = 5/3$ system, the $n = 6/4$ system is very sensitive to additional potential offsets, such that the inclusion of the harmonic confinement and wall potentials leads to a favoured occupation of the central sites, while in a perfect box potential the predicted density profile is flat. All our observations are well explained by the single-band Bose-Hubbard model, while being consistent with previous numerical calculations beyond the single-band model [46]. The inclusion of higher bands was shown to result in repulsion effects and fragmentation of the on-site density. While such effects will be present here, their observation would require the ability to probe the atomic wave function with sub-lattice-site resolution, hence it is not done in this

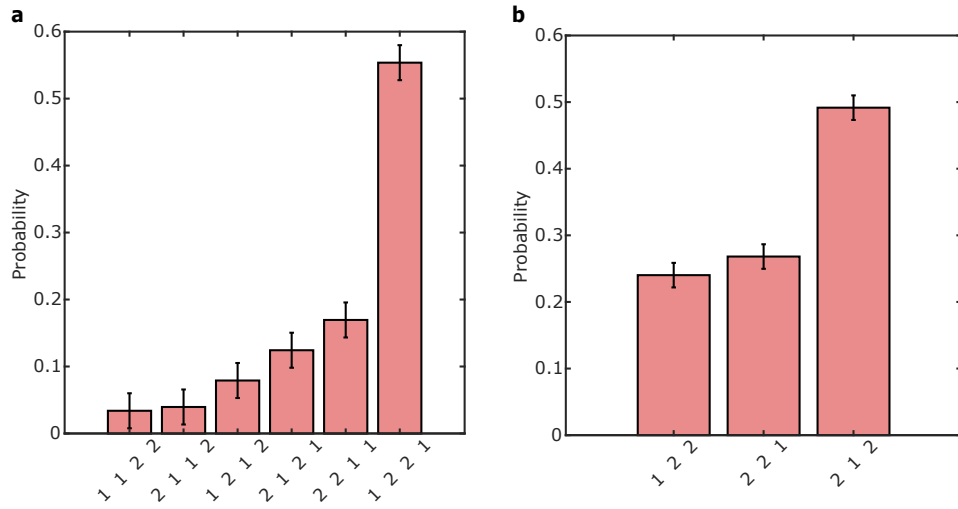


Figure 5.7: **State detection probabilities for incommensurate systems with two additional particles.** **a**, Probability to detect the different number states for a system with 6 atoms on 4 sites. **b**, same for the system with 5 atoms on 3 sites. Figure published in Supplementary Information of Ref. [45].

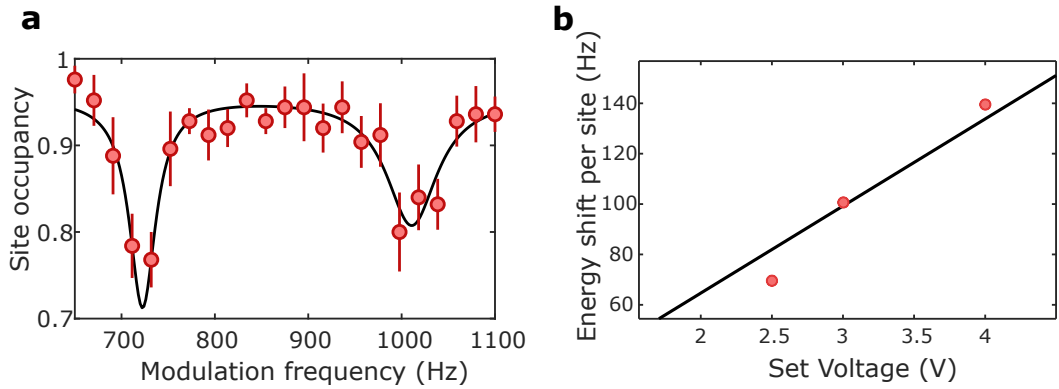


Figure 5.8: **Calibration of the magnetic gradient field.** **a**, Observed occupancy within the centre 5×5 sites of a $n = 1$ Mott Insulator at $U/h = 830(100)$ Hz versus the modulation frequency. The line is a fit with a double Lorentzian to obtain the peak positions. Each data point is obtained by averaging over the atom number counted over five images. The error bars are the standard error. **b**, Energy shift per lattice site for three different magnetic gradient field strengths. The line is a straight line fit through the origin. Figure published in Supplementary Information in Ref. [45].

thesis.

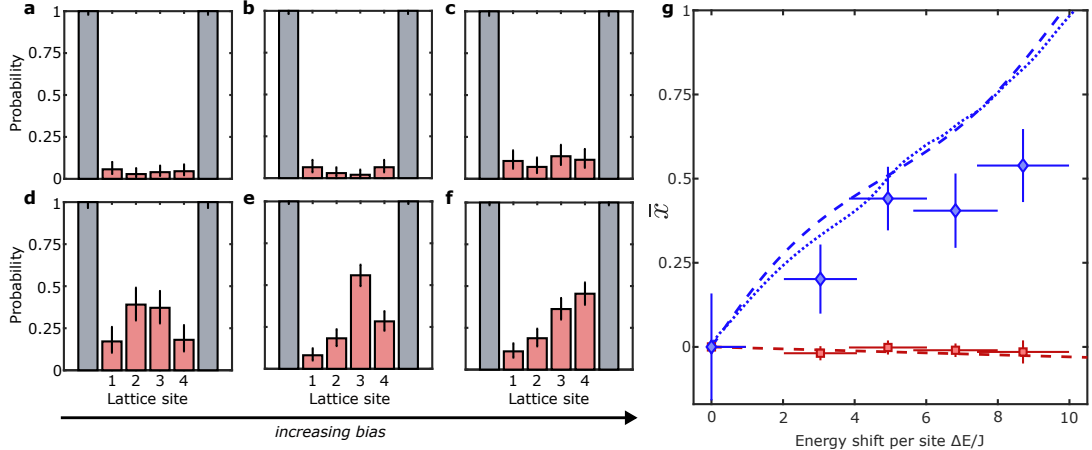


Figure 5.9: **Mott insulator and doped insulator in a bias potential.** a-c, Probability distributions of detecting an empty site in a commensurate system (four atoms on four sites) for maximum energy shifts per lattice site $\Delta E/J = 0(1), 5(1), 9(1)$ resulting from the bias potential. d-f, same distributions of an incommensurate system for the same potential (five atoms on four sites), where the empty site can result from the detection of a doublon. g, Centre-of-mass shift, \bar{x} , measured in lattice sites, relative to the original distribution as a function the energy shift ΔE , for a commensurate (red squares) and incommensurate (blue diamonds) system, together with the corresponding numerical simulations of the ground state (dashed lines) and the ensemble average (dotted lines). Errors of $\Delta E/J$ and \bar{x} are calculated via error propagation from the gradient calibration and from the counting statistics, respectively. Each histogram is obtained by averaging over 100 – 300 1D systems. Figure published in [45].

5.6 Particle mobility in a bias potential

It is expected that doped insulators will behave differently from undoped ones when subject to external probes, e.g., when measuring their compressibility and particle mobility. To show this we investigate how the commensurate and incommensurate systems change when subject to a gradient potential of the form $\hat{H}_g = \Delta E \sum_{i=1}^N i \hat{n}_i$, where ΔE denotes the energy shift per lattice site and \hat{n}_i the local number operator. We use a deep lattice, $V_x = 16(1) E_r$, $J/h = 9(1)$ Hz, and a magnetic bias field that is slowly increased within 500 ms using the same hyperbolic tangent function that is used for the lattice ramps, with $\tau = 200$ ms to maintain adiabaticity. We calibrate the bias field by applying it to a Mott insulator without any barriers, and then modulate the lattice intensity at a range of frequencies. When the modulation frequency matches the interaction energy plus or minus the gradient potential, the atoms will be excited

to an occupied neighbouring site. This reduces the observed occupancy, creating two peaks in a scan of the modulation frequency (Figure 5.8a). We only measured the occupancy in the central 5×5 sites to reduce the effect of the harmonic potential on the calibration. We calculated the energy shift from the external potential for three different strengths and fitted the data (Figure 5.8b). The peaks fitted for the calibration were asymmetrical, with a clearer signal for the left peak (when the modulation matches the gradient minus the interaction energy).

When the bias field is applied to a commensurate system of four atoms on four sites, the distribution of the the empty sites remains almost unchanged (Fig. 5.9a - c) [71]. In the incommensurate system of five atoms on four lattice sites, the probability of finding the additional atom (detected as an empty site), is skewed in the direction of the force produced by the gradient (Fig. 5.9d - f), showing that the doped insulator has a different and nonzero compressibility compared to the undoped state. We quantify this effect by computing the centre of mass, \bar{x} , of the histograms in Figs. 5.9a to 5.9f as a function of ΔE . We compute the centre of mass in the case of the incommensurate system using $\bar{x} = \sum_{i=1}^4 i w_i / \sum_{i=1}^4 w_i$, where w_i is the probability to find an empty site (i.e., the extra atom on a doubly occupied site) on lattice site i . To match this for the commensurate system, we use $\bar{w}_i = 1 - w_i$ instead of w_i , such that for the histograms of both commensurate and incommensurate systems the centre of mass shift of the atoms is calculated.

While there is no change of the centre of mass for the commensurate system (Fig. 5.9g, red squares), for the incommensurate system (Fig. 5.9g, blue diamonds), \bar{x} increases with ΔE , showing that the incommensurate (doped) system is compressible [72, 73]. The centre-of-mass shift is sensitive to the specific shape of the potential barriers and the harmonic confinement, which is accounted for by the numerical simulation of the system dynamics (see Section 5.7).

5.7 Numerical simulations

For strongly interacting systems towards the Tonks-Girardeau limit with filling above unity, it is known that higher bands need to be accounted for as the on-site repulsion

results in a fragmentation of the density of the particles in the ground state within individual sites [46]. However, for the case considered here, the quantum gas microscope can resolve between single sites and not for the particle density within a site. Therefore, we consider the single-band (lowest energy) Bose-Hubbard model to model the atoms in the one-dimensional optical lattices (Chapter 2). We calculate J and U from the Wannier functions (Section 2.4), while ϵ_i accounts for the weak harmonic confinement and the impact of the wall potential, taking into account the calibrated height of the potential barriers and the point-spread function of the microscope.

We emulate the dynamics of the experiment numerically, accounting for the full Hilbert space of the finite lattice with fixed particle number in all cases. The state is initialised in the Mott insulator of the lattice with commensurate filling and we numerically implement the same protocol for higher filling factors. For the ramps between deep and shallow lattice potentials, we evolve the system through the implementation of the unitary evolution operator for discrete time steps, with a maximum error for individual steps of 10^{-6} . We simulate the discrete steps of the potentials caused by the discrete frames of the DMD pattern when moving the barriers. To account for an initial thermal distribution of the state, we evolve each initial eigenstate individually and calculate the final non-zero temperature state as the sum of the evolved states weighted by the Boltzmann distribution. Figure 5.10 shows the eigenstate energies across the experimental sequence, with the corresponding atomic densities. There is a slight asymmetry in the final result due to the compression on one side of the system. Overall, we find good agreement between the zero temperature numerical results and the experiment.

The imaging quench to a deep lattice was simulated across a range of starting J/U values for both commensurate and incommensurate densities to ensure that it does not introduce non-adiabatic effects and results in a frozen density profile. As the same imaging quench is used in each of the experimental realisations, we exclude it from the simulation.

There is a small probability that the initial one-dimensional system of the experiment has one more or one less atom than the number of lattice sites. We have simulated

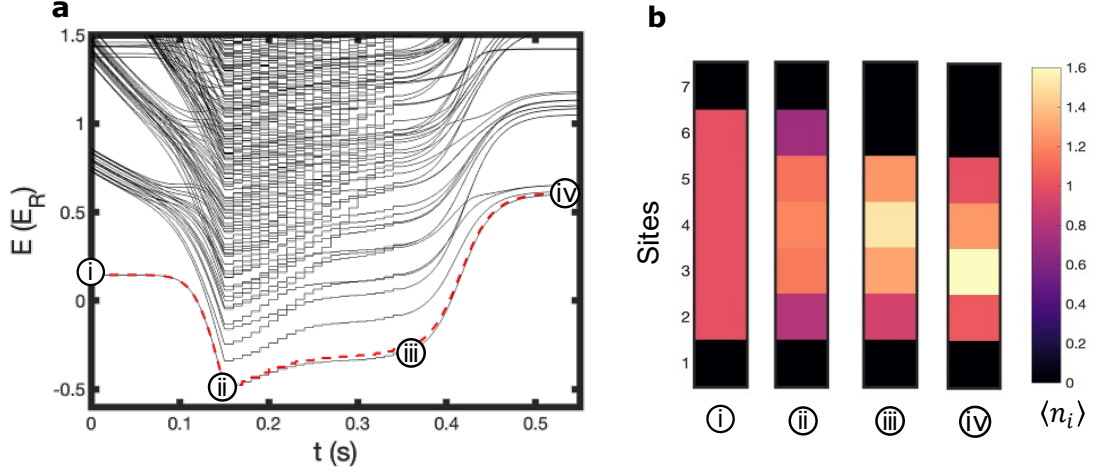


Figure 5.10: **Numerical simulations.** **a**, the black lines are the eigenstate energies and the red line is the energy of the dynamical zero temperature state. **b**, atom density at each individual site over the four points of the experiment. The calculations have 7 sites as it includes the two walls as sites with potential offsets.

the impact of this non-perfect state preparation to confirm that the observation of additional empty sites is not due to excitations from non-adiabatic effects, as these would not be captured by our numerical protocol with fixed atom number. We emulate the imperfect preparation by simulating the case of one additional atom and one less atom. We then combine the results with those assuming a perfect initial state preparation, to mimic what we observe experimentally using the post-selection process. The combination of the results is weighted to match the experimental data, assuming that the incorrect state preparation arises from an equal number of holes and doubly-occupied sites.

Details of potential shape

In our numerical simulations we take into account the point spread function of the imaging system, which is calculated assuming it is diffraction limited, causing a broadening of the repulsive potential barriers and an energy offset, ϵ_{off} , on the lattice site closest to the barrier (Fig. 5.11). For a repulsive barrier producing a maximum light shift of $\Delta_{LS}/h = 3.3(5) \text{ kHz} = 3.5(5)U$, the energy offset is $\epsilon_{\text{off}} = 0.027(4)\Delta_{LS} = 2\pi\hbar \times 90(10) \text{ Hz}$. This offset becomes significant when we apply the bias potential

(measurements presented in Fig. 5.9) as this energy offset opposes the centre of mass shift. For the lattice depth $V_x = 16(1) E_T$ used in Fig. 5.9, the energy offset on the outermost site of the system is $\epsilon_{\text{off}} \approx 0.1 U \approx 10J$.

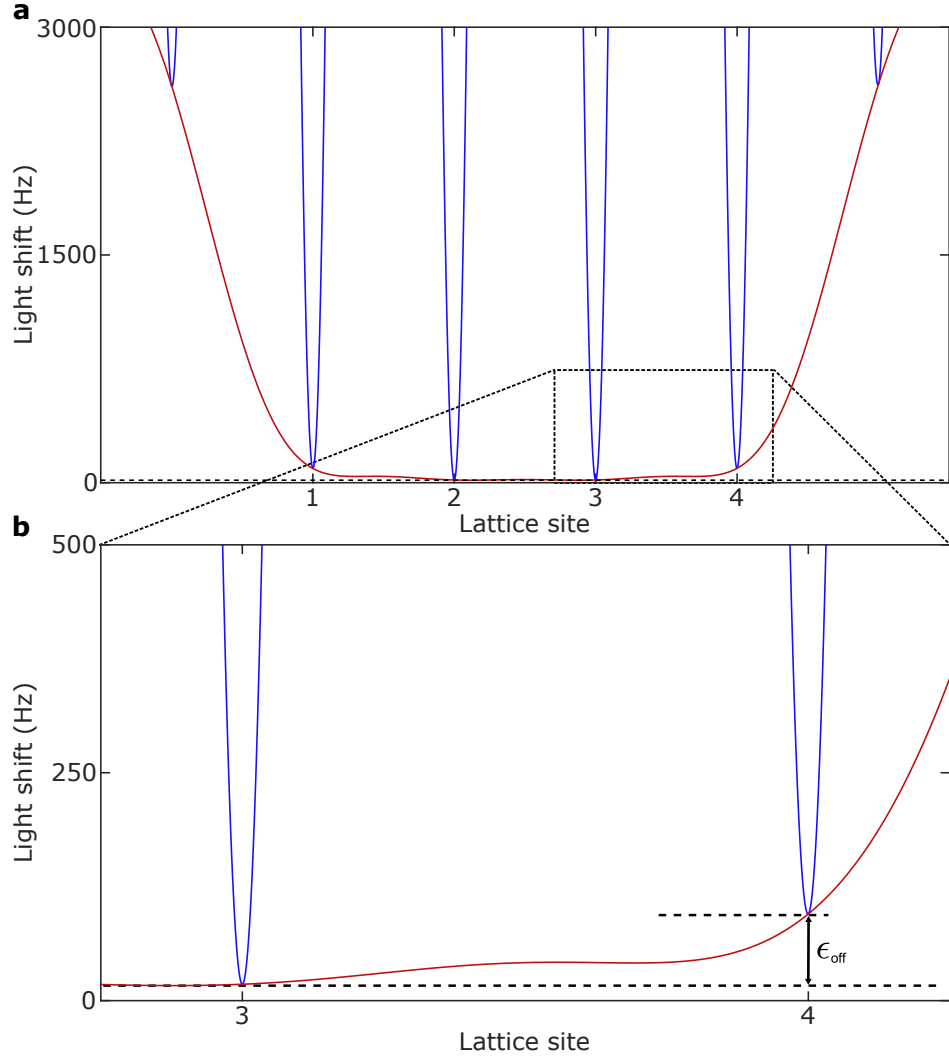


Figure 5.11: **Effect of the point spread function on the potential shape.** **a**, Lattice potential of the projected repulsive potential barriers (red) and that of the combined potential including the optical lattice (blue). **b**, Magnified view of the outer two lattice sites to show the energy offset ϵ_{off} . Figure published in Supplementary Information of Ref. [45].

Strong-interactions limit

The standard Bose-Hubbard model can be solved in the limit of strong interactions via perturbative approaches, instead of using Trotter-Suzuki decomposition in this work to simulate the system dynamics [74]. For fixed atom and lattice site numbers, as studied in this work, we can use the limit of $U/J \rightarrow \infty$ (deep lattice) to further restrict the finite Hilbert space. From this, analytical solutions for the low-energy states can be found [70]. For example, in the case of 5 atoms on 3 sites, as we take $U/J \rightarrow \infty$ it is natural to assume that the possibility of three atoms occupying a single site is vanishingly small due to its high onsite-interaction energy of $6U$. As we have fixed atom and site number, states with two atoms in a single site must be allowed, giving the restricted Hilbert space for the low energy states of $\{|221\rangle, |212\rangle, |122\rangle\}$. The Hamiltonian is then the kinetic energy term only, with the interaction term being a constant diagonal offset for each basis state. The ground state is then given by

$$|\psi\rangle_{\text{GS}}^{5\text{on}3} = \frac{1}{\sqrt{2}} |212\rangle + \frac{1}{2} (|221\rangle + |122\rangle), \quad (5.2)$$

with the favouring of the atoms being located on the edge of the system. This is in good agreement with the experimental data for 5 atoms on 3 sites (Figure 5.6c).

A similar process can be repeated for each configuration considered in the main text. For example in the case of 6 atoms on 4 sites, we obtain:

$$\begin{aligned} |\psi\rangle_{\text{GS}}^{6\text{on}4} = & \frac{1}{2} (|2121\rangle + |1212\rangle) + \frac{1}{\sqrt{5}} (|2112\rangle + |1221\rangle) \\ & + \frac{1}{2\sqrt{5}} (|2211\rangle + |1122\rangle), \end{aligned} \quad (5.3)$$

and the case of five atoms on four sites

$$|\psi\rangle_{\text{GS}}^{5\text{on}4} = \mathcal{N} \left[|1211\rangle + |1121\rangle + \frac{2}{1 + \sqrt{5}} (|2111\rangle + |1112\rangle) \right], \quad (5.4)$$

with $\mathcal{N} = (1 + \sqrt{5}) / \left(2\sqrt{2 + \frac{1}{2}(1 + \sqrt{5})^2} \right)$. With 6 atoms on 4 sites, we would observe a flat distribution for the hole probability, which is in contrast to our experimental

results as explained earlier (see section 5.5). The results for five atoms on four sites give an increased chance for the atom to be found in the centre, matching our experimental results (see section 5.2).

5.8 Discussion

We have studied the effects of commensurability in one-dimensional bosonic quantum systems. Key to this is our ability to produce engineered dynamical light potentials at the scale of single lattice sites. Starting from a commensurate filling with a known atom number between static potential barriers, we moved the barriers to change the number of available lattice sites, producing incommensurate systems. To characterise our degree of control of the state preparation, we characterised these systems by measuring the occurrence of holes and doublons from strong to weak interactions. For incommensurate systems, featuring delocalised atoms on a localised background, we observed non-trivial site occupation probabilities, in agreement with our numerical calculations. Studying the spatial distribution of our systems in a potential gradient, we observed particle mobility and compressibility of the incommensurate systems, while the commensurate ones remain in an incompressible Mott-insulating state. To enable the study of larger systems, a weaker external confinement would be required, which can be achieved by programming a deconfining potential using the DMD. This would also allow us to study systems doped with holes instead of particles. Introducing disorder to incommensurate systems leads to a way to further explore the transitions between superfluid and Bose glass for few-boson systems and the effect on compressibility [15, 61, 63]. For ladder systems, control over the atom number can lead to further interesting effects including the realisation of a ‘rung Mott insulator’, predicted in a two-leg ladder with half filling [75, 76], where atoms are localised over two sites on each leg (Section 7.0.2). Our methods for generating dynamically controlled potentials can also be used to adiabatically prepare low entropy states with controlled incommensurability or doping in both bosonic and fermionic systems.

Chapter 6

Disordered systems

6.1 Introduction

In this chapter, we use the DMD to generate reproducible random patterns that locally offset the lattice potential to realise the disordered Bose-Hubbard model.

The Bose-Hubbard model is an effective model and basis for quantum simulation of real materials but it misses the effect of impurities in crystals that can be present in real materials. Disorder is present in most real-world materials to varying degrees and has effects on the thermalisation and transport [77]. Disorder has been studied across a wide range of areas in condensed matter physics, with interacting and non-interacting gases, in both experiment and theory. For non-interacting atoms, any disorder leads to Anderson localisation which occurs because of wave interference from scattering on the disordered medium [78]. Anderson localisation has been observed in cold-atom systems with quasi-periodic lattices and external potentials [79–82]. When interactions are added, Anderson localisation no longer occurs as the system tries to minimise the interaction energy which counteracts the localisation [83, 84]. The interplay between disorder and interactions opens up more complex physics, such as the occurrence of the Bose glass phase for interacting bosons in a disordered medium, and spin glasses in fermionic systems [62, 85–87]. The Bose glass phase is theorised to exist between the superfluid and Mott insulator for any amount of disorder, and is a ground-state phase that is insulating and compressible [88, 89]. It has no long-range phase coherence

unlike the superfluid, but has a gapless energy spectrum. The Bose glass has a non-zero Edwards-Anderson parameter that can be used to distinguish between the Mott insulator and the Bose glass [90]. It has been observed in 2D in a lattice with an external potential and in a quasi-crystal [91, 92].

By tuning the strength of the disorder and the lattice depth, we have taken initial steps to exploring the transition from the superfluid or Mott insulator to the Bose glass [91, 93, 94]. By using time-of-flight imaging, we can differentiate between the superfluid and the Bose glass states by observing the system's long-range phase coherence [92, 95]. The phase coherence could also be determined by measuring the superfluid fraction from Leggett's formula [96]. By calculating the Edwards-Anderson parameter (see Eqn. 6.2), we can tell apart the Mott insulator from the Bose glass [90]. We demonstrate the preparation of the Bose glass phase in a 2D harmonic trap and initial work towards probing the phase diagram for the disordered Bose-Hubbard model.

One of the areas of interest in this context is the effect of disorder on thermalisation and ergodicity. For a system to be ergodic, all microstates of the system must be equally probable over a long period of time. Thermalisation requires redistribution of particles and energy in the system and so localisation directly counteracts that. Localised systems can be used to encode quantum information in the initial state that is not lost at long times [77]. Many-body localisation is caused by disorder in an out-of-equilibrium state where the state of the system does not thermalise. Many-body localisation was shown for fermionic and bosonic systems with external potentials [13, 97, 98]. The Bose glass is a groundstate phase rather than an out-of-equilibrium system and the exact nature of how it might connect to many-body localisation is not well-understood. A method to explore the ergodicity of the Bose glass involves crossing the phase transition from the Bose glass to the superfluid. If the Bose glass is non-ergodic, there will be significant heating from changes in the Bose-glass regime and the system will not be able to restore phase coherence [92].

The majority of ultracold atom experiments with disordered systems make use of speckle patterns or quasi-crystals, where you do not have exact control over the disordered system you generate [99–102]. By using the DMD, we can program reproducible

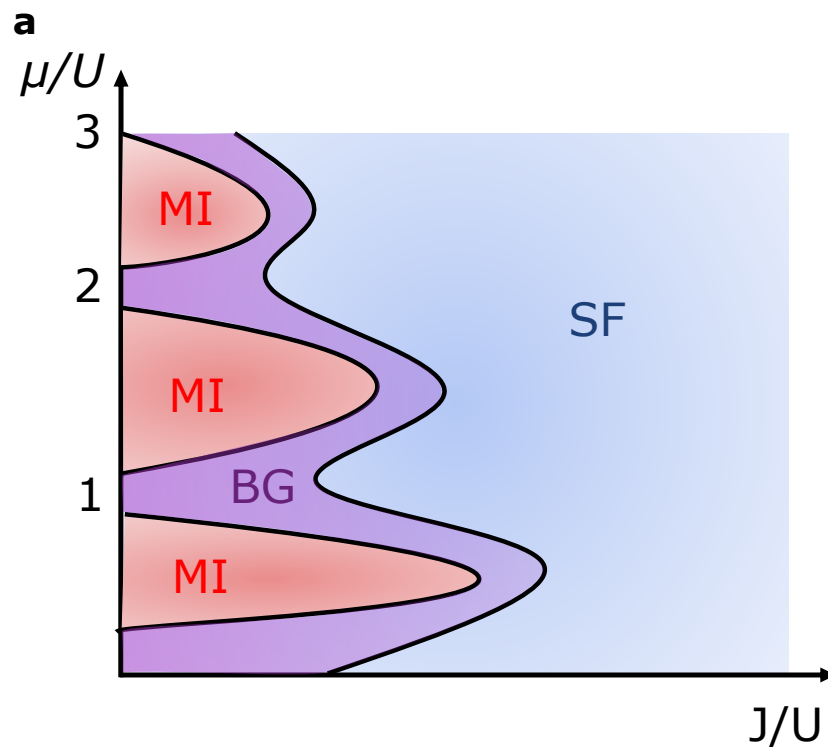


Figure 6.1: **Illustration of the phase diagram of the disordered 2D Bose-Hubbard model.** The Bose-glass is theorised to exist between the superfluid and the Mott insulator for increasing disorder, leading to no direct transition between the superfluid and the Mott insulator. If the disorder strength is greater than the interaction energy, then the Mott insulator cannot form.

disorder patterns that match the patterns used in the theory calculations. We can also explore the effect of a different number of disordered patterns on the measurement of the Edwards-Anderson parameter. This work was started at the end of my PhD and has been continued after finishing writing the thesis.

6.2 Preparation of the Bose-glass state

The Bose-glass phase is theorised to exist between the Mott insulator and superfluid states for any amount of disorder in the system. This means that there is no direct transition between the two phases in the presence of disorder (Figure 6.1). The disordered Bose-Hubbard model is given by

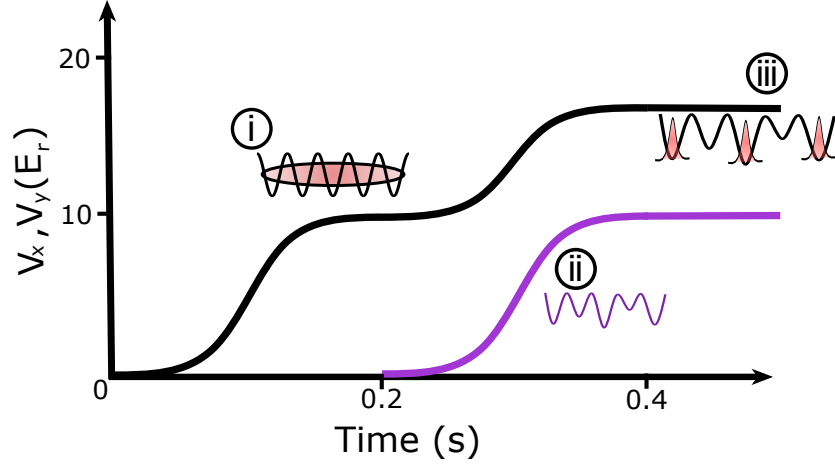


Figure 6.2: **Experimental procedure for preparing a Bose-glass.** First, the depths of the horizontal lattices are set to $V_x, V_y = 10 E_r$ to prepare a 2D superfluid where the atoms are delocalised over the lattice sites. Then the light with the disorder pattern is turned on while going to a deeper lattice. The disorder pattern creates the potential offsets between different lattice sites that leads to regions of localisation.

$$\hat{H} = -J \sum_{i,j} \hat{a}_i^\dagger \hat{a}_j + \sum_i \frac{U}{2} \hat{n}_i (\hat{n}_i - 1) + \sum_i (\epsilon_i - \mu) \hat{n}_i + \sum_i \Delta_i \hat{n}_i, \quad (6.1)$$

where Δ_i is the disorder potential offset on each site. Δ_i creates random energy offsets on each lattice site, with a uniform box distribution $\Delta_i \in [0, \Delta]$, where Δ is the disorder strength.

We generate the disorder pattern on the DMD and use the feedback algorithm (Chapter 4) to compensate for the Gaussian beam intensity distribution. To have access to more optical power for the disorder we use an octagon shape for the pattern. As the feedback algorithm regulates to the lowest value of the Gaussian light incident on the DMD, using a smaller shape that still covers the entire atomic cloud gives us more optical power. In the phase diagram for the disordered Bose-Hubbard model, as the disorder causes the Mott lobes to decrease in size, we can monitor the formation of the Bose-glass by preparing a deep lattice, $V_x, V_y = 14 E_r$, with increasing disorder strength. As we have a varying chemical potential, for increasing disorder strength the Bose-glass will first appear at the edges of the system and then eventually the whole system will be a Bose-glass once $\Delta > U$.

To realise the Bose glass phase, we first prepare a 2D superfluid with a lattice depth

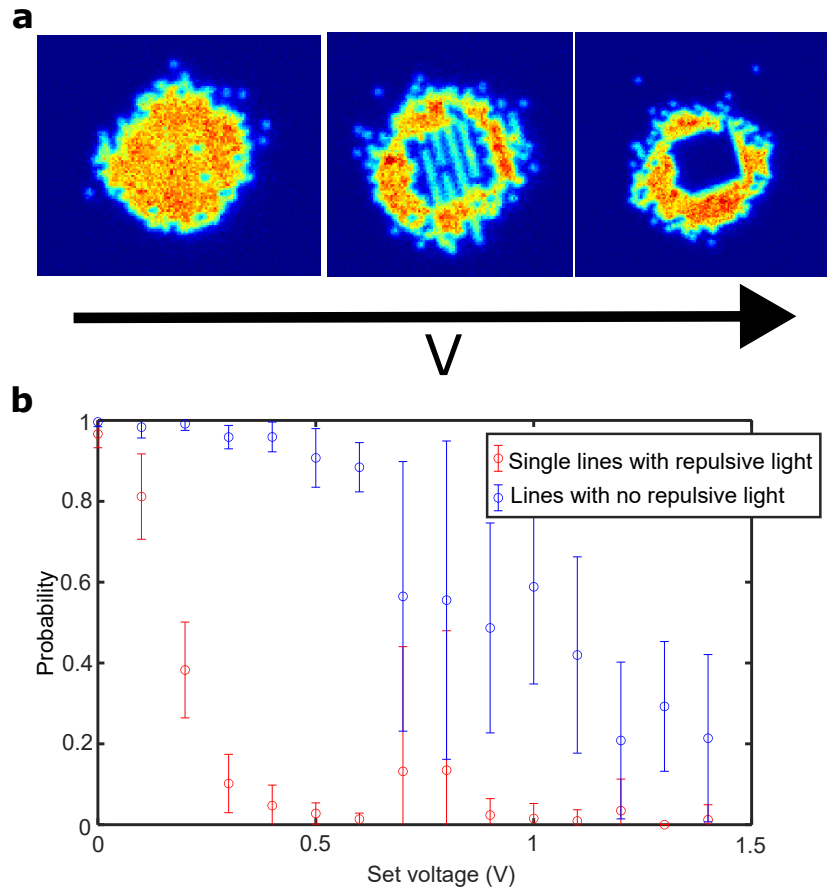


Figure 6.3: **Calibration for the disorder pattern.** **a**, Fluorescence images of the Mott insulator with single lines of intensity with increasing strength. As the intensity is increased, the lattice sites that the light is incident on have reduced occupancy down to zero. Due to the point spread function of the microscope objective, the neighbouring lattice sites have some intensity and they also experience a reduced occupancy with increasing strength. **b**, probability of occupancy in the single lines that have repulsive light incident on them and the probability for the neighbouring single lines that do not have the repulsive light incident on them.

of $V_x, V_y = 10 E_r$ with no disorder. We ramp to this 2D superfluid over 200 ms and $\tau = 70$ ms. We then ramp simultaneously the repulsive potential and the lattice depth to their final values over 100 ms (Figure 6.2). We found that the switch-on procedure for the disorder potential was critical in determining the final state of the system. When the disorder pattern was applied simultaneously with the horizontal lattice beams, only small changes in phase coherence and the Edwards-Anderson parameter (Section 6.3) were observed, likely due to increased heating. However, heating was reduced when the

random potential was introduced at a lattice depth of $10 E_r$. At this depth, the atoms remained in the superfluid phase, where tunneling was still possible, and the system was able to adjust to the added disorder potential. This two-step process, enabled the preparation of the Bose glass phase while minimising changes to the lattice depth that could otherwise induce heating.

We calibrate the depth of the disorder pattern by comparing it to the chemical potential of the system. We project a pattern with distinct lines of light and increased their intensity until the atoms are removed on the neighbouring sites (Figure 6.3). This provides an initial calibration of the strength of the disorder pattern. Lines with repulsive light are fully removed at a set voltage of 0.4V, which corresponds to a light shift equal to the harmonic potential offset at the edge of the cloud (300 Hz). The approach can also be used to determine the percentage of light that is incorrectly projected on neighbouring sites. We observe that sites show a reduced occupancy after a set voltage of 0.6V. This effect reduces the effective disorder strength. The total strength of the disorder pattern is the difference between the maximum and minimum potential depth.

6.3 Edwards-Anderson parameter

The Bose-glass differs from the Mott insulator by the absence of an energy gap and a finite compressibility, and from the superfluid by the absence of long-range phase coherence. As the disordered Bose-Hubbard model has three competing phases, an order parameter that can distinguish the Bose-glass from both the Mott insulator and the superfluid is needed. One such order parameter is the Edwards-Anderson order parameter which is zero in the Mott insulator and superfluid, and non-zero in the Bose-glass. The Edwards-Anderson order parameter is given by

$$q = \overline{\langle \hat{n}_i \rangle^2} - \overline{\langle \hat{n}_i \rangle}^2 \quad (6.2)$$

where the overline refers to the disorder average and the brackets the thermal average (Figure 6.4) [90]. It can be seen that for no disorder, $q = 0$, as in the Mott insulator,

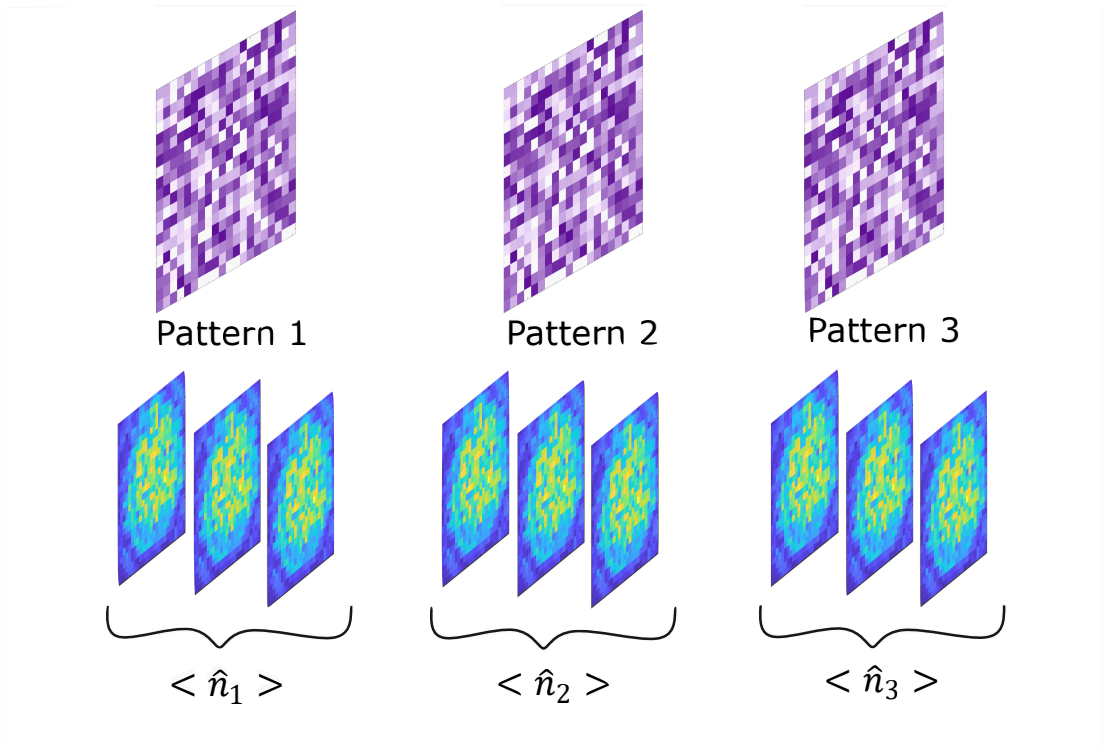


Figure 6.4: **Illustration of the method for calculating $\langle \hat{n}_i \rangle$ for the Edwards-Anderson (EA) order parameter.** A number of images are taken for each disorder pattern and averaged. Each set of disorder-averaged pictures are then used to calculate the EA parameter.

\hat{n}_i has a fixed integer value. In the superfluid state, the order parameter should also go towards zero as \hat{n}_i remains the same value for each thermal average of the system. Experimentally, the superfluid phase leads to a non-zero value of q . In the presence of weak disorder, the superfluid will have some correlations between the density and the disorder as the change in chemical potential leads to an inhomogeneous superfluid. The temperature will also contribute to a non-zero q throughout the cloud. This makes it difficult to differentiate between the superfluid and the Bose-glass using the Edwards-Anderson parameter.

We have taken preliminary results on the transition from the Mott Insulator to the Bose-glass by measuring the Edwards-Anderson parameter for increasing disorder. In the Mott Insulator, we see that q approaches zero in the centre of the cloud, but has a non-zero value on the edge (Figure 6.5). This is due to the finite temperature

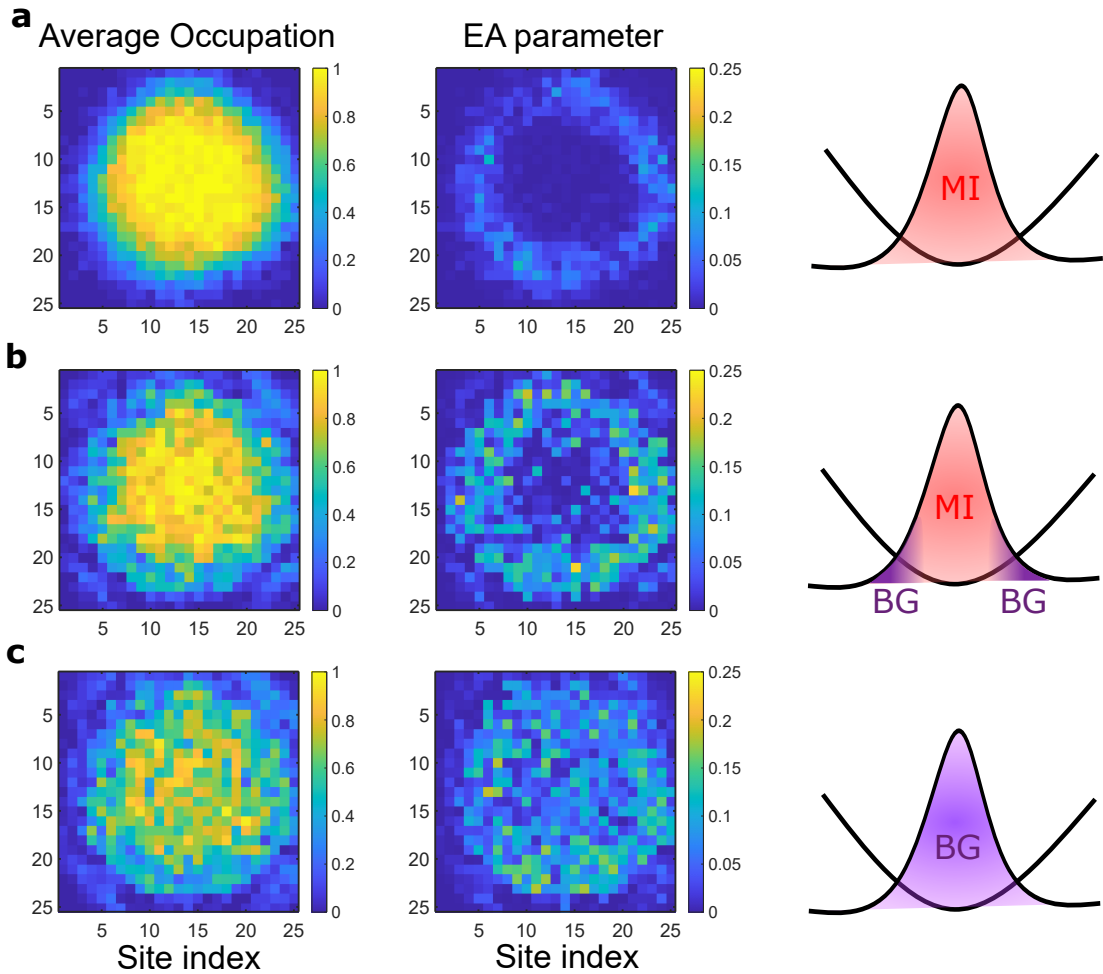


Figure 6.5: **Average occupations and Edwards-Anderson parameters.** **a**, Average occupations and EA parameter for the Mott insulator with zero disorder. The occupations are constant at one in the centre of the cloud, and q is zero. At the edges of the cloud, q increases and the average occupations decrease due to the finite temperature of the cloud. **b**, Average occupations and EA parameter for a cloud with disorder strength less than the interaction strength. q increases on the edge of the cloud but remains zero in the centre where the system is still Mott insulating with constant occupations. The illustration of the wavefunctions shows the Bose-glass starting to form on the edges. **c**, Average occupations and EA parameter for the Bose-glass, where the disorder strength is now greater than the interaction energy. q is near constant through the system and the average occupations are no longer constant in the centre of the cloud.

as the entropy of the Mott insulator is pushed to the edge of the cloud where we observe particle number fluctuations. The average occupation in the centre of the Mott insulator is one, with very little variance, which is what leads to the zero Edwards-

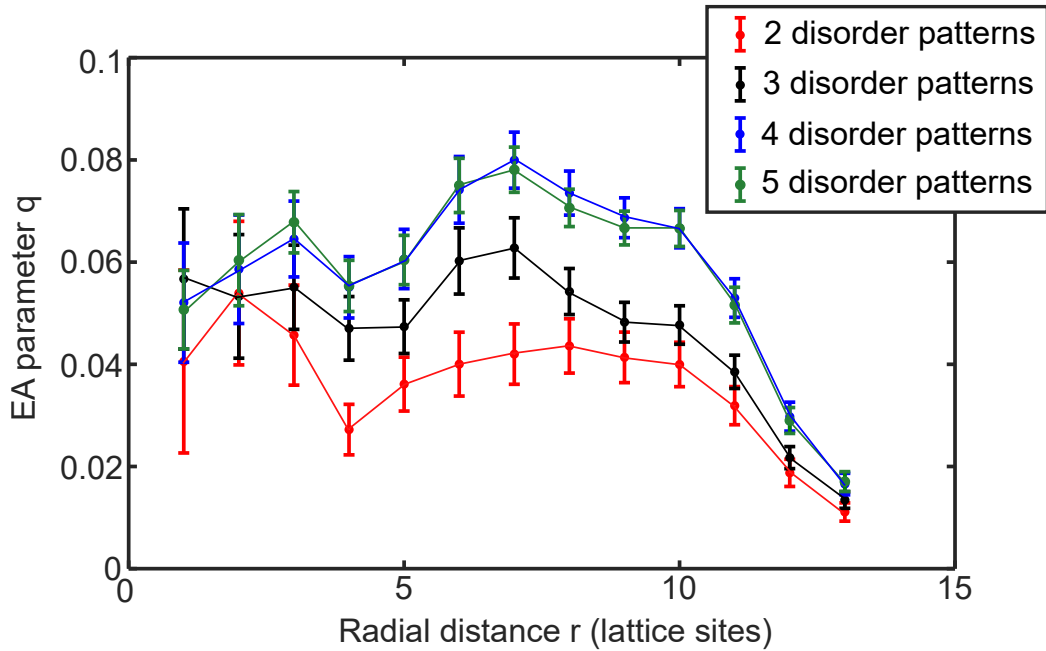


Figure 6.6: **Radial average of the Edwards-Anderson parameter for different numbers of disorder patterns.** As more disorder patterns are used in the calculation, the larger the Edwards-Anderson parameter. This effect continues until 4 disorder patterns, where adding anymore has minimal effect on the results. The data shown is taken at $V_x, V_y = 14 E_r$ and $\Delta/U = 2.5$.

Anderson parameter. When the disorder is added, q increases on the outside of the cloud while staying at zero in the centre. Once the strength of the disorder is larger than the on-site interactions, a Bose-glass is formed and q is non-zero throughout the cloud.

We study the effect of using different numbers of disorder patterns on the Edwards-Anderson parameter (Figure 6.6). The Edwards-Anderson parameter measures the correlations between the density and the disorder. Only including a small number of disorder patterns increases the probability of having regions that are similar across all the disorder patterns, which would reduce q . We take the radial average of q over the cloud and we find that q close to doubles in value going from using just two patterns compared to four patterns. There is not any difference when including a fifth pattern, suggesting that there is not a need to use more than 5 disorder patterns to get an accurate value for q .

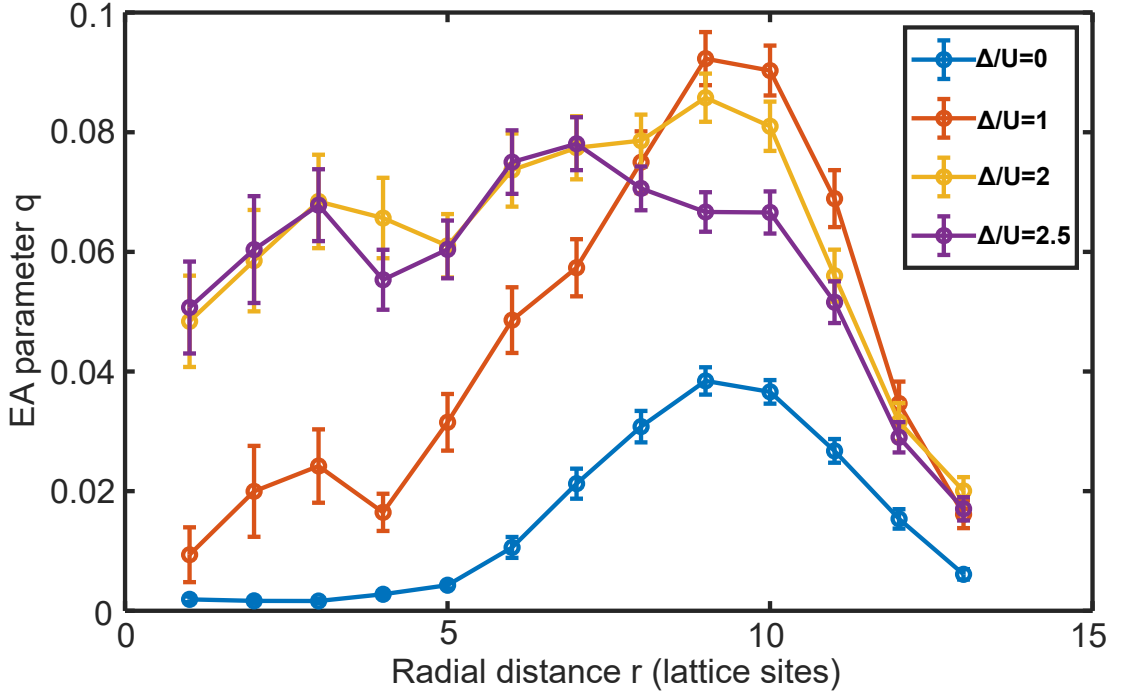


Figure 6.7: **Radial average of the Edwards-Anderson parameter for different disorder strengths.** Data taken at $V_x, V_y = 14 E_r$.

We investigate the effect of the disorder strength on the Edwards-Anderson parameter by looking at the radial averages of q for the cloud. For each dataset we took 5 sets of 10 images, with a different disorder pattern for each set. In the case with no disorder, we find that it approaches zero in the centre of the cloud and rises to $q = 0.04$ at the edge of the cloud. When we start to use the disorder, with $\Delta/U = 1$, q at the edge of the cloud rises to over 0.08 and the centre of the cloud increases slightly to $q = 0.02$, suggesting that we have now reached the Bose-glass phase. Further increasing the disorder leads to the centre of the cloud rising up to $q = 0.06$. There is no change from $\Delta/U = 2$ to $\Delta/U = 2.5$.

When the disorder strength is equal to the interaction energy, we should see an increase in the Edwards-Anderson parameter in the centre of the cloud. Our initial data shows an increase in q at $\Delta/U = 1$ which matches with our calibration for these initial results. Other groups have calibrated the disorder strength by using the differential light shift on atoms, which involves measuring the frequency difference required to transfer atoms between two hyperfine levels [13]. They start with a uniform box distribution

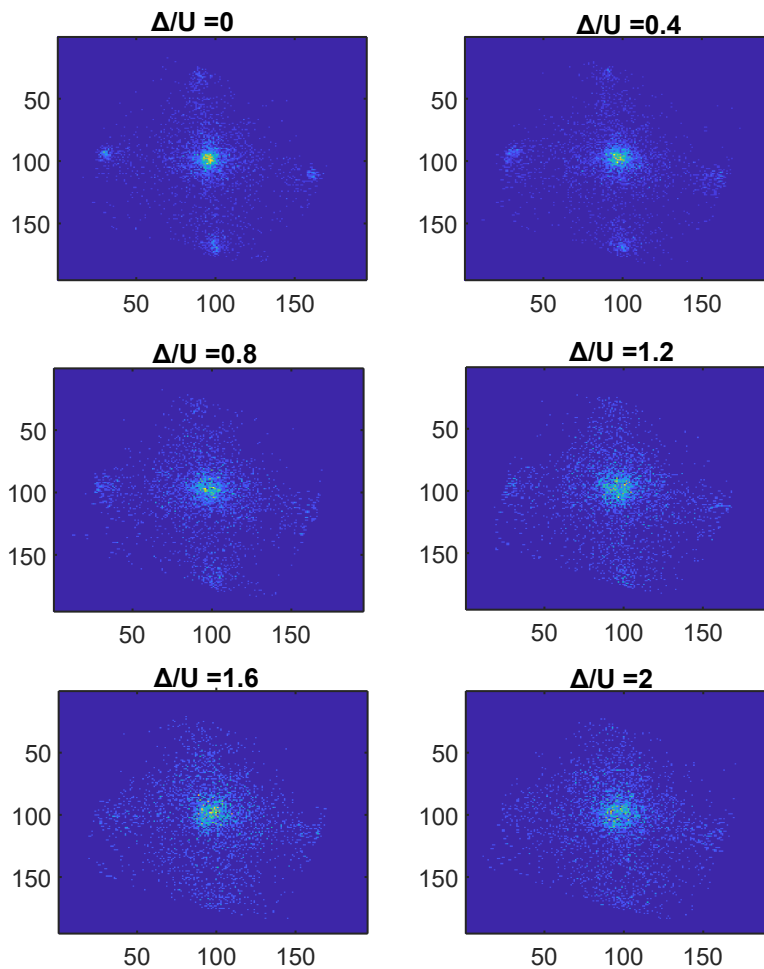


Figure 6.8: **Time-of-flight images for a range of disorder strengths.** The time-of-flight imaging was done for $V_{x,y} = 10 E_r$ in both horizontal lattices. The lattices were turned off in less than $50 \mu\text{s}$ and the atoms were allowed to evolve for 8 ms. The increasing disorder strength leads to a loss of long-range phase coherence that is measured by calculating the visibility (Figure 6.9.)

for their pattern and measure a skewed Gaussian distribution on the atoms from the light shift.

6.4 Time-of-flight measurements

One of the features of the Bose-glass is the lack of long-range phase coherence. The Bose-glass can be described as having regions of superfluid 'puddles' that are independent from each other, meaning that there is not a global phase that can be extracted

through the momentum distribution of the cloud. The superfluid to Bose-glass transition should then be characterised by a loss in phase coherence and can be measured as a decrease of the visibility as seen with the superfluid to Mott insulator transition (Figure 3.12).

We first turn the lattices to $V_{x,y} = 10 E_r$ and then turn the disorder on. The lattices are turned off in less than $50 \mu\text{s}$ and there is 8 ms before the distribution is imaged. As the disorder strength is increased, the peaks at the edge of the image from the phase coherence become less pronounced as atoms become spread out across the image (Figure 6.8). For small Δ , the phase is still superfluid but as the disorder pattern locally changes the chemical potential, the superfluid will be an inhomogeneous superfluid. This means that the density across the superfluid is not uniform so that there is a reduced superfluid fraction from this before the transition to the Bose-glass.

To quantify this effect, we measure the visibility of the cloud (Section 3.12) for different disorder strengths to quantify the transition from superfluid to Bose-glass. The visibility decreases for increasing disorder strength in line with the expected formation of separated superfluid 'puddles'. The exact point of transition from the superfluid to the Bose-glass has not been calculated theoretically for the visibility. We also explored other methods of quantifying the phase coherence, including the width of the centre peak, but we found that the visibility had less error in the measurement as the small number of atoms in the experiment made it hard to fit the width of the centre peak.

6.5 Outlook

To summarise, we have shown two experimental methods for distinguishing the Bose-glass from the Mott insulator or the superfluid. Both experimental methods for identifying the Bose-glass can be used to map out the phase diagram of the disordered Bose-Hubbard model. By varying the lattice depth with different disorder strengths, we can look at how the Bose-glass opens up between the Mott insulator and the superfluid. One area to explore is if there is or isn't a direct transition from the Mott insulator to the superfluid with disorder present.

Investigating the Bose-glass to superfluid transition is a way to explore the ergodic-

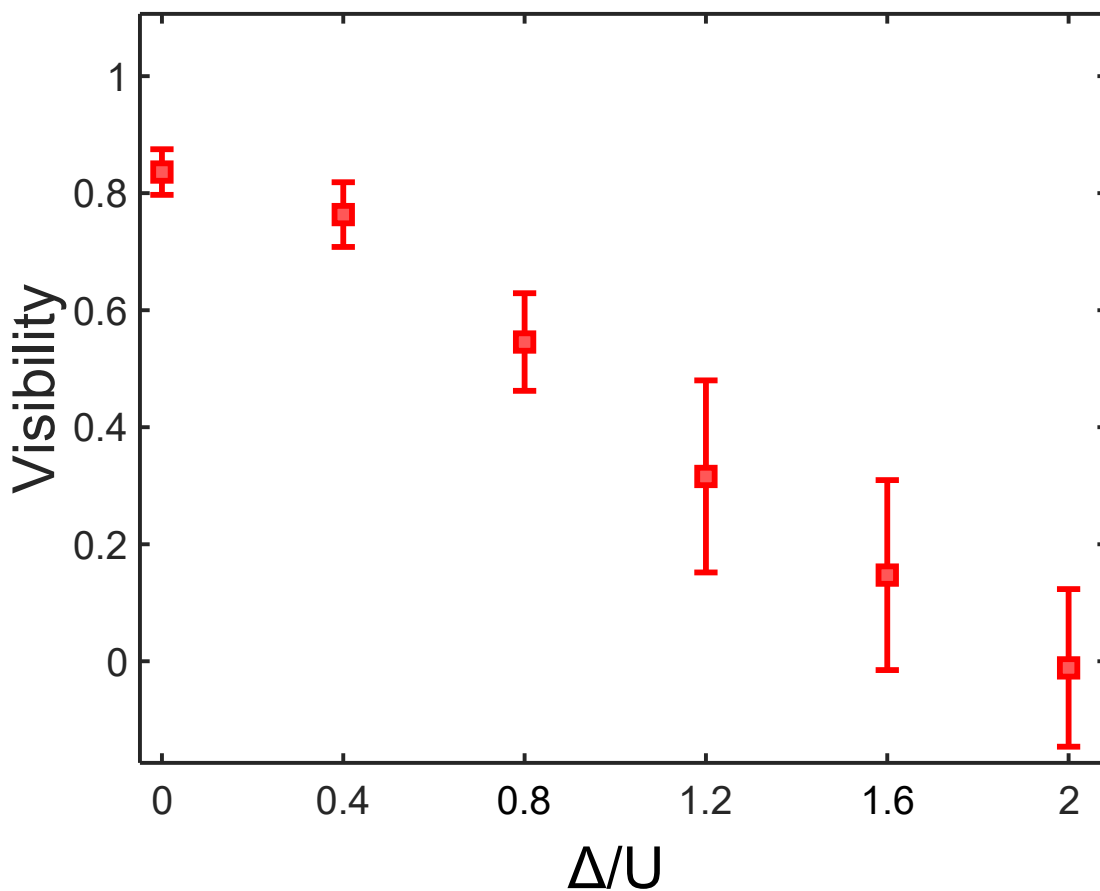


Figure 6.9: **Visibility measurement for increasing disorder strength.** The visibility is calculated from the images in Figure 6.8 by taking the difference between the peak and the corner (Section 3.12).

ity of the Bose-glass. As any small change in a non-ergodic phase will lead to heating, it should not be possible to go from the Bose-glass back to the superfluid. This can be measured through the phase coherence. This effect has been measured from a Bose-glass in a quasi-crystal going to a simple cubic lattice, and measuring an increase in the FWHM for systems that had been in the Bose-glass compared to those that had not been [92]. We also would like to explore if there is an effect on the hold time in the Bose-glass before imaging the phase coherence.

We have the capabilities to create 2D and quasi-2D geometries with specific number of lattice sites and atom number. This would allow the preparation of systems like a 2D system with 10x10 lattice sites, that can easily be captured with numerical simulations

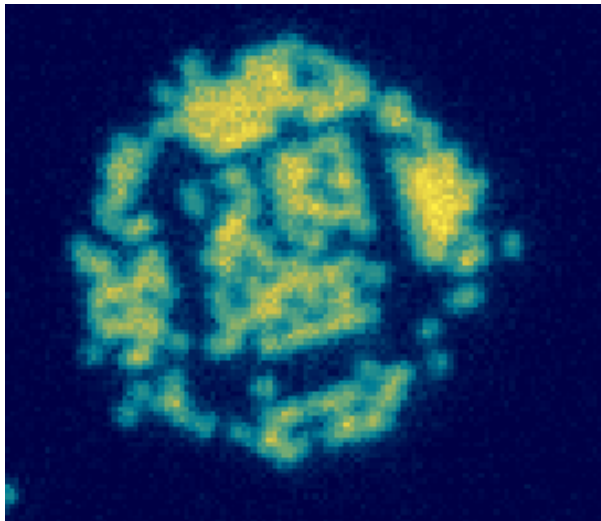


Figure 6.10: **Fluorescence image of a 10x10 area surrounded by a potential barrier with disorder.** To prepare a specific size 2D lattice with disorder, a potential barrier at the edge of the disorder pattern is used.

(Figure 6.10). The experiment and the simulations would be able to use the exact same disorder pattern. It would be possible to then explore the Mott insulator to Bose-glass transition by lowering the lattice depth, looking at where regions of superfluid puddles appear and then by continuing to lower the lattice how two superfluid puddles combine together.

In 1D, systems with spinless non-interacting fermions can be explored by using hardcore bosons, where the interactions approach infinity. Ladder geometries are then used to look at simple quasi-2D systems that can still be simulated [76, 103]. In the presence of disorder, hardcore bosons and non-interacting fermions behave differently as Anderson localisation occurs for the non-interacting particles. This provides a simple method for exploring the differences between bosons and fermions in the presence of disorder [104].

Chapter 7

Conclusion and outlook

7.0.1 Conclusion

In conclusion, we have presented 2D lattice experiments with ultra-cold atoms and single-site imaging. The introduction of the DMD to the experimental set-up has given more experimental control over the lattice including being able to prepare incommensurate and disordered systems. We can alter the underlying potential of the optical lattice using the 666 nm beam to make repulsive potentials and create specific sized 1D and 2D systems. We used the DMD dynamically to move images displayed on the DMD with sub-lattice site resolution. We used an intensity feedback algorithm to improve the accuracy of the images displayed on the DMD.

Through the use of engineered dynamical light potentials we have been able to explore commensurate and incommensurate one-dimensional systems. Dynamic potentials on the single-site scale have allowed for the controlled preparation of incommensurate systems by reducing the number of available lattice sites in the weakly-interacting regime. We were able to study non-trivial site occupation probabilities of the incommensurate systems and compare them to numerical simulations. Finally, we studied the differences between commensurate and incommensurate systems in the presence of a potential gradient. The incommensurate systems feature compression and particle mobility that is not present in the commensurate system.

By having control over the potential of single sites, we have introduced disorder to the system by having random offsets to the optical lattice. We explored the effect

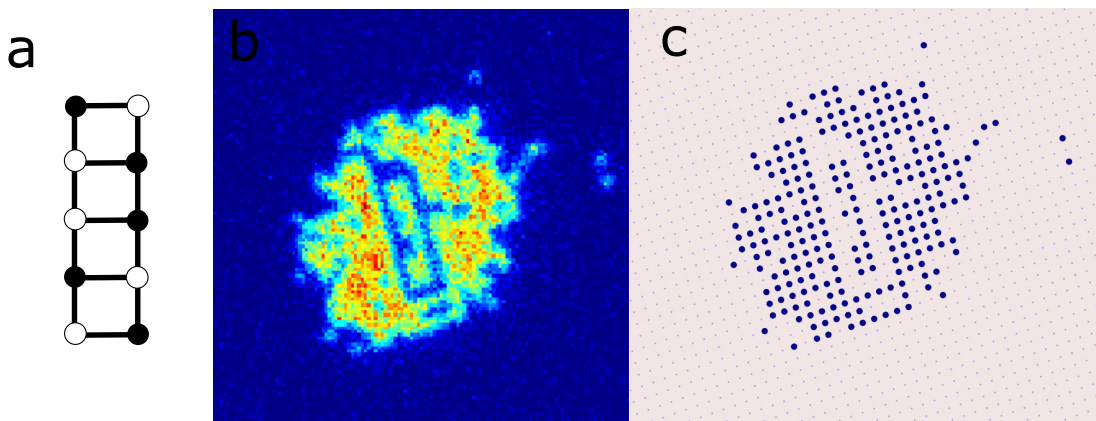


Figure 7.1: **2-leg ladder.** **a**, Schematic of the Rung-Mott insulator. Each rung should have one atom (black) and one hole (white). **b**, fluorescence image of a closed ladder system. **c**, reconstruction of the fluorescence image.

that disorder had on the long-range phase coherence in the system and measured the Edwards-Anderson order parameter in situ. We demonstrated preparation of the Bose-Glass, as shown by the loss of phase coherence and the change in the order parameter, with the intent to plot out the phase diagram in the future.

7.0.2 Outlook

We have demonstrated preparation of incommensurate 1D systems through dynamic potentials and it would be interesting to progress this technique to other lattice geometries. The addressing beam can be used in combination with different lattice geometries to prepare atoms on specific lattice sites. In this section, we look at some of the future experiments that are possible with the technical improvements, and some other experimental possibilities.

Ladders

In 1D systems, it was shown earlier that incommensurate systems host different physics in the strongly interacting regime (Chapter 5). Progressing this to ladders introduces different effects than in the 1D case. Ladders differ to 1D systems in the strongly interacting regime at low filling as they allow particles to pass each other by using the other leg of the ladder. In a 1D lattice at low filling and strong interactions, two atoms

cannot pass each other and the system can be described as a Tonks-Girardeau gas [105]. When a second leg is added to the system, at incommensurate fillings you now have a superfluid phase where the atoms are able to pass each other. This does not always hold true as, specifically at half filling in a 2-leg ladder (see Figure 7.1), hardcore bosons are theorised to form a Rung Mott insulator that is incompressible and has a gapped energy spectrum [75, 106]. An atom becomes delocalised across two sites on the two separate legs and the tunnelling is suppressed in the other direction. Through the addition of a particle or hole, the system can be brought back to the superfluid regime.

The Rung Mott insulator has not yet been realised experimentally and there remain open questions about the interleg tunnelling, interaction strengths and the minimum system size needed to experimentally see the phase. It is theorised that the Rung Mott insulator will exist for any amount of interleg tunnelling but finite temperature effects might mean that it doesn't hold true experimentally [76]. There are various approaches to preparing an incommensurate ladder, and these need to be investigated in order to identify a method that achieves high preparation fidelity while remaining in the ground state. The first method we have tried involves tuning the lattice to $V_{x,y} = 10 E_r$ to prepare a superfluid, and then turning the ladder potential on over 200 ms while simultaneously changing the lattice depth to $V_{x,y} = 20 E_r$ (See Figure 7.1). This method produces a 2-leg ladder but with a filling close to commensurate. To prepare the ladder at half filling, we could start with a closed box, only one site wide and then dynamically move one wall outwards by one site to prepare the system at half filling. For this method to work, we would need a high fidelity preparation for the one site wide box. Another method we could try would be to make use of the 787 nm beam (4), to select a single line of atoms in the Mott insulator state and use a microwave pulse to move all the other atoms to the $F = 2$ state and then heat them out the trap with a resonant beam. After this, we can swap to using the 666 nm and place the potential walls around the single line of atoms before then changing the lattice to the superfluid regime and then changing them to prepare the Rung Mott insulator.

The addition of disorder into the ladder system lets you probe the phase diagram between Bose-glass and Rung Mott insulator with disorder strength, interactions and

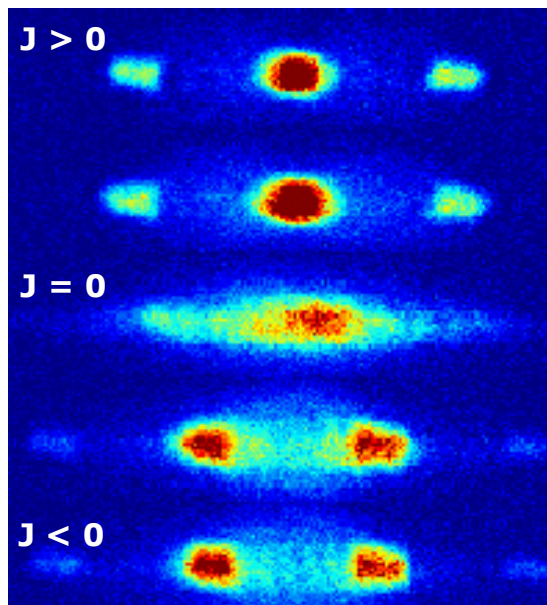


Figure 7.2: **Time-of-flight imaging for a driven lattice.** Increasing the driving strength reduces the effective tunnelling following a Bessel function.

atom number. For varying disorder strengths, there exists a Bose-glass phase between the superfluid and Rung Mott insulator when changing the atom density. For large enough values of disorder, the Rung Mott insulator cannot exist as the gap will be filled with localised states [75]. For a 3-leg ladder, there exists a Rung Mott insulator at one third filling. This density can also feature a 'gapless Mott insulator' which is incompressible but without the gap that normally characterises a Mott insulator [107]. Recently, ladders have been used with artificial magnetic fields to generate Meissner states and vortex states, using Raman-assisted tunnelling to control the tunnelling amplitudes [103, 108–112]. There is also a proposal on how to prepare solitons in a ladder [113].

Floquet

We are able to control U and J together with the power of the optical lattices, but it is also possible to control both individually. U can be controlled through a Feshbach resonance and J can be controlled with amplitude or phase modulation, which is referred to as Floquet physics. Amplitude modulation is where the intensity of the lattice is

modulated at a specific frequency and amplitude. Phase modulation involves modulating the phase of the lattice, which can be achieved by moving the retroreflecting mirror of the lattice with a piezo. Modulating the lattice can have different effects [114–117], and is most commonly used to create a reduced tunnelling term in the Hubbard model through time-averaging of high frequency modulation [118]. The effective tunnelling term has the form

$$J_{eff} = JJ_0(K/\hbar\omega) \quad (7.1)$$

where J_0 is the first order Bessel function and K is the driving strength. We demonstrate the effect of increasing the driving strength using phase modulation on a BEC with momentum imaging in free space (Fig. 7.2). As the driving strength is increased, J_{eff} reduces and reaches zero where there is no well-defined interference peaks. When J_{eff} becomes negative, the interference peaks are now at the edge of the band rather than in the centre.

Rubidium 85

It is possible to rework the experiment to work with ^{85}Rb instead of ^{87}Rb . The experiment starts with a natural source of rubidium so there is already ^{85}Rb readily available to use. ^{85}Rb has an advantage over ^{87}Rb by having a more easily accessible Feshbach resonance at 150 G. This can be used to control the interactions between atoms, that is needed for some experimental realisations [119,120].

To change the experiment to working with ^{85}Rb , we need to first change the laser locks for ^{85}Rb transitions. The master laser can easily be changed to lock onto the ^{85}Rb transition instead. The other lasers are offset locked to the master laser that involves mixing the beat signal with a 5.8 GHz. By changing it to 2.2 GHz, we are able to lock all the lasers to the ^{85}Rb transitions. There is also a microwave set-up already in place for the 3 GHz transitions between the $F = 2$ and $F = 3$ hyperfine states and there is progress towards winding and placing Feshbach coils into the experiment. We have performed red and grey molasses with ^{85}Rb and loaded the atoms into the CODT [121]. The next steps to the procedure is the atom transport before loading into the lattice,

Chapter 7. Conclusion and outlook

cooling and imaging. It is likely the Feshbach resonance is needed for to control the interactions for both the transport and the cooling stage [122].

With the introduction of a second master and repumper laser, it would be possible to work with ^{85}Rb and ^{87}Rb together. Using the two species together can allow you to create effective models [123]. The two species also have Feshbach resonances between the two atoms to control their interactions [22, 124]. ^{87}Rb might be able to be used to sympathetically cool the ^{85}Rb atoms if we are not able to reach the same temperatures that we can with ^{87}Rb .

Bibliography

- [1] I. Bloch and M. Greiner, “Exploring quantum matter with ultracold atoms in optical lattices,” *Advances in Atomic, Molecular, and Optical Physics*, vol. 52, pp. 1–47, 2005.
- [2] I. Bloch, J. Dalibard, and W. Zwerger, “Many-body physics with ultracold gases,” *Rev. Mod. Phys.*, vol. 80, pp. 885–964, 2008.
- [3] C. Gross and I. Bloch, “Quantum simulations with ultracold atoms in optical lattices,” *Science*, vol. 357, pp. 995–1001, 2017.
- [4] D. A. Abanin, E. Altman, I. Bloch, and M. Serbyn, “Colloquium: Many-body localization, thermalization, and entanglement,” *Rev. Mod. Phys.*, vol. 91, p. 021001, 2019.
- [5] I. Bloch, J. Dalibard, and W. Zwerger, “Many-body physics with ultracold gases,” *Rev. Mod. Phys.*, vol. 80, pp. 885–964, 2008.
- [6] D. Jaksch, C. Bruder, J. I. Cirac, C. W. Gardiner, and P. Zoller, “Cold bosonic atoms in optical lattices,” *Phys. Rev. Lett.*, vol. 81, pp. 3108–3111, 1998.
- [7] M. Greiner, O. Mandel, T. Esslinger, T. W. Hänsch, and I. Bloch, “Quantum phase transition from a superfluid to a mott insulator in a gas of ultracold atoms,” *Nature*, vol. 415, pp. 39–44, 2002.
- [8] S. Kuhr, “Quantum-gas microscopes: a new tool for cold-atom quantum simulators,” *National Science Review*, vol. 3, pp. 170–172, 04 2016.

Bibliography

- [9] J. F. Sherson, C. Weitenberg, M. Endres, M. Cheneau, I. Bloch, and S. Kuhr, “Single-atom-resolved fluorescence imaging of an atomic Mott insulator,” *Nature*, vol. 467, pp. 68–72, 2010.
- [10] W. S. Bakr, A. Peng, M. E. Tai, R. Ma, J. Simon, J. I. Gillen, S. Fölling, L. Pollet, and M. Greiner, “Probing the superfluid-to-Mott insulator transition at the single-atom level,” *Science*, vol. 329, pp. 547–550, 2010.
- [11] T. Oka and S. Kitamura, “Floquet engineering of quantum materials,” *Annual Review of Condensed Matter Physics*, vol. 10, pp. 387–408, 2019.
- [12] C. Weitenberg, M. Endres, J. F. Sherson, M. Cheneau, P. Schauß, T. Fukuhara, I. Bloch, and S. Kuhr, “Single-spin addressing in an atomic Mott insulator,” *Nature*, vol. 471, pp. 319–324, 2011.
- [13] J. Choi, S. Hild, J. Zeiher, P. Schauß, A. Rubio-Abadal, T. Yefsah, V. Khemani, D. A. Huse, I. Bloch, and C. Gross, “Exploring the many-body localization transition in two dimensions,” *Science*, vol. 352, p. 1547, 2016.
- [14] R. Islam, R. Ma, P. M. Preiss, M. Eric Tai, A. Lukin, M. Rispoli, and M. Greiner, “Measuring entanglement entropy in a quantum many-body system,” *Nature*, vol. 528, pp. 77–83, 2015.
- [15] M. P. A. Fisher, P. B. Weichman, G. Grinstein, and D. S. Fisher, “Boson localization and the superfluid-insulator transition,” *Phys. Rev. B*, vol. 40, pp. 546–570, 1989.
- [16] F. Gerbier, S. Fölling, A. Widera, O. Mandel, and I. Bloch, “Probing number squeezing of ultracold atoms across the superfluid-mott insulator transition,” *Phys. Rev. Lett.*, vol. 96, p. 090401.
- [17] C. Weitenberg, “Single-atom resolved imaging and manipulation in an atomic mott insulator,” *Dissertation der Fakultät für Physik der Ludwig-Maximilians-Universität München*, 2011.

Bibliography

- [18] B. Capogrosso-Sansone, Ş. G. Söyler, N. Prokof'ev, and B. Svistunov, “Monte carlo study of the two-dimensional bose-hubbard model,” *Phys. Rev. A*, vol. 77, p. 015602, 2008.
- [19] T. D. Kühner and H. Monien, “Phases of the one-dimensional bose-hubbard model,” *Phys.Rev. B*, vol. 58, p. R14741, 1998.
- [20] R. Grimm, M. Weidemüller, and Y. B. Ovchinnikov, “Optical dipole traps for neutral atoms,” vol. 42, pp. 95–170, 2000.
- [21] M. Greiner, “Ultracold quantum gases in three-dimensional optical lattice potentials,” *Dissertation in the Physics department of the Ludwig-Maximilians-Universität München*, 2003.
- [22] C. Chin, R. Grimm, P. Julienne, and E. Tiesinga, “Feshbach resonances in ultracold gases,” *Rev. Mod. Phys.*, vol. 82, p. 1225, 2010.
- [23] C. Weitenberg and J. Simonet, “Tailoring quantum gases by floquet engineering,” *Nat. Phys.*, vol. 17, p. 1342–1348, 2021.
- [24] W. Kohn, “Analytic properties of Bloch waves and Wannier functions,” *Phys. Rev.*, vol. 115, pp. 809–821, 1959.
- [25] R. Walters, G. Cotugno, T. Johnson, S. Clark, and D. Jaksch, “Ab initio derivation of hubbard models for cold atoms in optical lattices,” *Phys. Rev. A*, vol. 87, p. 043613, 2013.
- [26] O. Morsch and M. Oberthaler, “Dynamics of Bose-Einstein condensates in optical lattices,” *Rev. Mod. Phys.*, vol. 78, pp. 179–215, 2006.
- [27] W. Zwerger, “Mott – Hubbard transition of cold atoms in,” *J. Opt. B: Quantum Semiclass. Opt.*, vol. 5, pp. 5–16, 2003.
- [28] A. Ulibarrena, “Creation of an all-optical bose-einstein condensate,” *PhD Thesis, University of Strathclyde*, 2020.

Bibliography

- [29] I. Despard, “The construction of a bosonic quantum-gas microscope,” *PhD Thesis, University of Strathclyde*, 2021.
- [30] M. Khudaverdyan, W. Alt, I. Dotsenko, L. Förster, S. Kuhr, D. Meschede, Y. Miroshnychenko, D. Schrader, and A. Rauschenbeutel, “Adiabatic quantum state manipulation of single trapped atoms,” *Phys. Rev. A*, vol. 71, p. 031404, 2005.
- [31] C.-L. Hung, X. Zhang, N. Gemelke, and C. Chin, “Accelerating evaporative cooling of atoms into bose-einstein condensation in optical traps,” *Phys. Rev. A*, vol. 78, p. 011604, 2008.
- [32] D. Jacob, E. Mimoun, L. De Sarlo, M. Weitz, J. Dalibard, and F. Gerbier, “Production of sodium Bose–Einstein condensates in an optical dimple trap,” *New J. Phys.*, vol. 13, p. 065022, 2011.
- [33] C. Weitenberg, M. Endres, J. F. Sherson, M. Cheneau, P. Schau, T. Fukuhara, I. Bloch, and S. Kuhr, “Single-spin addressing in an atomic Mott insulator,” *Nature*, vol. 471, pp. 319–325, 2011.
- [34] A. La Rooij, C. Ulm, E. Haller, and S. Kuhr, “A comparative study of deconvolution techniques for quantum-gas microscope images,” *New J. Phys.*, vol. 25, p. 083036, 2023.
- [35] W. S. Bakr, A. Peng, M. E. Tai, R. Ma, J. Simon, J. I. Gillen, S. Fölling, L. Pollet, and M. Greiner, “Probing the superfluid–to–mott insulator transition at the single-atom level,” *Science*, vol. 329, pp. 547–550, 2010.
- [36] P. A. Murthy, D. Kedar, T. Lompe, M. Neidig, M. G. Ries, A. N. Wenz, G. Zürn, and S. Jochim, “Matter-wave fourier optics with a strongly interacting two-dimensional fermi gas,” *Phys. Rev. A*, vol. 90, p. 043611, 2014.
- [37] F. Gerbier, A. Widera, S. Fölling, O. Mandel, T. Gericke, and I. Bloch, “Phase coherence of an atomic mott insulator,” *Phys. Rev. Lett.*, vol. 95, p. 050404, 2005.

Bibliography

- [38] C. Ulm, “Multi-site addressing of single atoms in a quantum gas microscope,” *Master’s Thesis, University of Strathclyde*, 2022.
- [39] A. M. Kaufman and K.-K. Ni, “Quantum science with optical tweezer arrays of ultracold atoms and molecules,” *Nat. Phys.*, vol. 17, pp. 1324–1333, 2021.
- [40] N. Navon, R. P. Smith, and Z. Hadzibabic, “Quantum gases in optical boxes,” *Nat. Phys.*, vol. 17, pp. 1334–1341, 2021.
- [41] S. Flannigan, L. Madaïl, R. G. Dias, and A. J. Daley, “Hubbard models and state preparation in an optical lieb lattice,” *New J. Phys.*, vol. 23, p. 083014, 2021.
- [42] M. Sun, T. Čadež, I. Yurkevich, and A. Andreanov, “Enhancement of superconductivity in the fibonacci chain,” *Phys. Rev. B*, vol. 109, p. 134504, 2024.
- [43] M. Di Liberto, A. Hemmerich, and C. Morais Smith, “Topological varma superfluid in optical lattices,” *Phys. Rev. Lett.*, vol. 117, p. 163001, 2016.
- [44] A. Rubio-Abadal, J.-y. Choi, J. Zeiher, S. Hollerith, J. Rui, I. Bloch, and C. Gross, “Many-body delocalization in the presence of a quantum bath,” *Phys. Rev. X*, vol. 9, p. 041014, 2019.
- [45] A. Di Carli, C. Parsonage, A. La Rooij, L. Koehn, C. Ulm, C. W. Duncan, A. J. Daley, E. Haller, and S. Kuhr, “Commensurate and incommensurate 1D interacting quantum systems,” *Nat Commun*, vol. 15, no. 474, 2024.
- [46] I. Brouzos, S. Zöllner, and P. Schmelcher, “Correlation versus commensurability effects for finite bosonic systems in one-dimensional lattices,” *Phys. Rev. A*, vol. 81, p. 053613, 2010.
- [47] A. N. Wenz, G. Zürn, S. Murmann, I. Brouzos, T. Lompe, and S. Jochim, “From few to many: Observing the formation of a fermi sea one atom at a time,” *Science*, vol. 342, pp. 457–460, 2013.
- [48] P. A. Lee, N. Nagaosa, and X.-G. Wen, “Doping a mott insulator: Physics of high-temperature superconductivity,” *Rev. Mod. Phys.*, vol. 78, pp. 17–85, 2006.

Bibliography

- [49] M. Xu, L. Kendrick, A. Kale, Y. Gang, G. Ji, R. Scalettar, M. Lebrat, and M. Greiner, “Frustration- and doping-induced magnetism in a fermi–hubbard simulator,” *Nature*, vol. 620, p. 971–976, 2023.
- [50] R. Anderson, F. Wang, P. Xu, V. Venu, S. Trotzky, F. Chevy, and J. H. Thywissen, “Conductivity spectrum of ultracold atoms in an optical lattice,” *Phys. Rev. Lett.*, vol. 122, p. 153602, 2019.
- [51] P. T. Brown, D. Mitra, E. Guardado-Sanchez, R. Nourafkan, A. Reymbaut, C.-D. Hébert, S. Bergeron, A.-M. S. Tremblay, J. Kokalj, D. A. Huse, P. Schauß, and W. S. Bakr, “Bad metallic transport in a cold atom fermi-hubbard system,” *Science*, vol. 363, pp. 379–382, 2019.
- [52] M. A. Nichols, L. W. Cheuk, M. Okan, T. R. Hartke, E. Mendez, T. Senthil, E. Khatami, H. Zhang, and M. W. Zwierlein, “Spin transport in a mott insulator of ultracold fermions,” *Science*, vol. 363, pp. 383–387, 2019.
- [53] C. S. Chiu, G. Ji, A. Bohrdt, M. Xu, M. Knap, E. Demler, F. Grusdt, M. Greiner, and D. Greif, “String patterns in the doped Hubbard model,” *Science*, vol. 365, pp. 251–256, 2019.
- [54] G. Salomon, J. Koepsell, J. Vijayan, T. A. Hilker, J. Nespolo, L. Pollet, I. Bloch, and C. Gross, “Direct observation of incommensurate magnetism in hubbard chains,” *Nature*, vol. 565, pp. 56–60, 2019.
- [55] J. Koepsell, J. Vijayan, P. Sompet, F. Grusdt, T. A. Hilker, E. Demler, G. Salomon, I. Bloch, and C. Gross, “Imaging magnetic polarons in the doped fermi–hubbard model,” *Nature*, vol. 572, pp. 358–362, 2019.
- [56] J. Koepsell, D. Bourgund, P. Sompet, S. Hirthe, A. Bohrdt, Y. Wang, F. Grusdt, E. Demler, G. Salomon, C. Gross, and I. Bloch, “Microscopic evolution of doped mott insulators from polaronic metal to fermi liquid,” *Science*, vol. 374, pp. 82–86, 2021.

Bibliography

- [57] G. Ji, M. Xu, L. H. Kendrick, C. S. Chiu, J. C. Brüggenjürgen, D. Greif, A. Bohrdt, F. Grusdt, M. Knap, E. Demler, M. Lebrat, and M. Greiner, “Coupling a Mobile Hole to an Antiferromagnetic Spin Background: Transient Dynamics of a Magnetic Polaron,” *Phys. Rev. X*, vol. 11, p. 021022, 2021.
- [58] S. Hirthe, T. Chalopin, D. Bourgund, P. Bojović, A. Bohrdt, E. Demler, F. Grusdt, I. Bloch, and J. Zeiher, “Magnetically mediated hole pairing in fermionic ladders of ultracold atoms,” *Nature*, vol. 613, pp. 463–467, 2023.
- [59] A. Lazarides, O. Tieleman, and C. Morais Smith, “Strongly interacting bosons in a one-dimensional optical lattice at incommensurate densities,” *Phys. Rev. A*, vol. 84, p. 023620, 2011.
- [60] H. P. Büchler, “Crystalline phase for one-dimensional ultra-cold atomic bosons,” *New J. Phys.*, vol. 13, p. 093040, 2011.
- [61] B. Damski, J. Zakrzewski, L. Santos, P. Zoller, and M. Lewenstein, “Atomic bose and anderson glasses in optical lattices,” *Phys. Rev. Lett.*, vol. 91, p. 080403, 2003.
- [62] L. Fallani, J. E. Lye, V. Guarrera, C. Fort, and M. Inguscio, “Ultracold atoms in a disordered crystal of light: Towards a bose glass,” *Phys. Rev. Lett.*, vol. 98, p. 130404, 2007.
- [63] X. Cai, S. Chen, and Y. Wang, “Superfluid-to-bose-glass transition of hardcore bosons in a one-dimensional incommensurate optical lattice,” *Phys. Rev. A*, vol. 81, p. 023626, 2010.
- [64] G. E. Astrakharchik, K. V. Krutitsky, M. Lewenstein, F. Mazzanti, and J. Boronat, “Optical lattices as a tool to study defect-induced superfluidity,” *Phys. Rev. A*, vol. 96, p. 033606, 2017.
- [65] W. J. Kwon, G. Del Pace, K. Khani, L. Galantucci, A. Muzi Falconi, M. Inguscio, F. Scazza, and G. Roati, “Sound emission and annihilations in a programmable quantum vortex collider,” *Nature*, vol. 600, pp. 64–69, 2021.

Bibliography

- [66] G. Del Pace, K. Khani, A. Muzi Falconi, M. Fedrizzi, N. Grani, D. Hernandez Rajkov, M. Inguscio, F. Scazza, W. J. Kwon, and G. Roati, “Imprinting persistent currents in tunable fermionic rings,” *Phys. Rev. X*, vol. 12, p. 041037, 2022.
- [67] M. T. Reeves, K. Goddard-Lee, G. Gauthier, O. R. Stockdale, H. Salman, T. Edmonds, X. Yu, A. S. Bradley, M. Baker, H. Rubinsztein-Dunlop, M. J. Davis, and T. W. Neely, “Turbulent relaxation to equilibrium in a two-dimensional quantum vortex gas,” *Phys. Rev. X*, vol. 12, p. 011031, 2022.
- [68] T. Fukuhara, A. Kantian, M. Endres, M. Cheneau, P. Schauß, S. Hild, D. Bellem, U. Schollwöck, T. Giamarchi, C. Gross, I. Bloch, and S. Kuhr, “Quantum dynamics of a mobile spin impurity,” *Nat. Phys.*, vol. 9, pp. 235–241, 2013.
- [69] M. Rigol, G. G. Batrouni, V. G. Rousseau, and R. T. Scalettar, “State diagrams for harmonically trapped bosons in optical lattices,” *Phys. Rev. A*, vol. 79, p. 053605, 2009.
- [70] D. Raventós, T. Graß, M. Lewenstein, and B. Juliá-Díaz, “Cold bosons in optical lattices: a tutorial for exact diagonalization,” *Journal of Physics B: Atomic, Molecular and Optical Physics*, vol. 50, no. 11, p. 113001, 2017.
- [71] N. Gemelke, X. Zhang, C. L. Hung, and C. Chin, “In situ observation of incompressible Mott-insulating domains in ultracold atomic gases,” *Nature*, vol. 460, pp. 995–998, 2009.
- [72] T.-L. Ho and Q. Zhou, “Obtaining the phase diagram and thermodynamic quantities of bulk systems from the densities of trapped gases,” *Nat. Phys.*, vol. 6, pp. 131–134, 2010.
- [73] E. Busley, L. Miranda, A. Redmann, C. Kurtscheid, K. K. Umesh, F. Vewinger, M. Weitz, and J. Schmitt, “Compressibility and the equation of state of an optical quantum gas in a box,” *Science*, vol. 375, pp. 1403–1406, 2022.

Bibliography

- [74] N. M. Myers, R. Scott, K. Park, and V. W. Scarola, “Quantum simulation costs for suzuki-trotter decomposition of quantum many-body lattice models,” *Physical Review Research*, vol. 5, no. 2, p. 023199, 2023.
- [75] J. Carrasquilla, F. Becca, and M. Fabrizio, “Bose-glass, superfluid, and rung-Mott phases of hard-core bosons in disordered two-leg ladders,” *Phys. Rev. B*, vol. 83, pp. 1–7, 2011.
- [76] F. Crépin, N. Laflorencie, G. Roux, and P. Simon, “Phase diagram of hard-core bosons on clean and disordered two-leg ladders: Mott insulator-Luttinger liquid-Bose glass,” *Phys. Rev. B*, vol. 84, pp. 1–22, 2011.
- [77] D. A. Abanin, E. Altman, I. Bloch, and M. Serbyn, “Colloquium: Many-body localization, thermalization, and entanglement,” *Rev. Mod. Phys.*, vol. 91, p. 021001, 2019.
- [78] P. W. Anderson, “Absence of diffusion in certain random lattices,” *Phys. Rev.*, vol. 109, pp. 1492–1505, 1958.
- [79] G. Roati, C. D’Errico, L. Fallani, M. Fattori, C. Fort, M. Zaccanti, G. Modugno, M. Modugno, and M. Inguscio, “Anderson localization of a non-interacting bose-einstein condensate,” *Nature*, vol. 453, pp. 895–898, 2008.
- [80] F. Jendrzejewski, A. Bernard, K. Mueller, P. Cheinet, V. Josse, M. Piraud, L. Pezzé, L. Sanchez-Palencia, A. Aspect, and P. Bouyer, “Three-dimensional localization of ultracold atoms in an optical disordered potential,” *Nat. Phys.*, vol. 8, pp. 398–403, 2012.
- [81] D. H. White, T. A. Haase, D. J. Brown, M. D. Hoogerland, M. S. Najafabadi, J. L. Helm, C. Gies, D. Schumayer, and D. A. Hutchinson, “Observation of two-dimensional anderson localisation of ultracold atoms,” *Nat commun*, vol. 11, p. 4942, 2020.
- [82] S. S. Kondov, W. R. McGehee, J. J. Zirbel, and B. DeMarco, “Three-dimensional anderson localization of ultracold matter,” *Science*, vol. 334, pp. 66–68, 2011.

Bibliography

- [83] R. T. Scalettar, G. G. Batrouni, and G. T. Zimanyi, “Localization in interacting, disordered, bose systems,” *Phys. Rev. Lett.*, vol. 66, pp. 3144–3147, 1991.
- [84] W. Krauth, N. Trivedi, and D. Ceperley, “Superfluid-insulator transition in disordered boson systems,” *Phys. Rev. Lett.*, vol. 67, pp. 2307–2310, 1991.
- [85] J.-W. Lee, M.-C. Cha, and D. Kim, “Phase diagram of a disordered boson hubbard model in two dimensions,” *Phys. Rev. Lett.*, vol. 87, p. 247006, 2001.
- [86] I. Aleiner, B. Altshuler, and G. Shlyapnikov, “A finite-temperature phase transition for disordered weakly interacting bosons in one dimension,” *Nat. Phys.*, vol. 6, pp. 900–904, 2010.
- [87] K. Binder and A. P. Young, “Spin glasses: Experimental facts, theoretical concepts, and open questions,” *Rev. Mod. Phys.*, vol. 58, pp. 801–976, 1986.
- [88] L. Pollet, N. V. Prokof’ev, B. V. Svistunov, and M. Troyer, “Absence of a direct superfluid to mott insulator transition in disordered bose systems,” *Phys. Rev. Lett.*, vol. 103, p. 140402, 2009.
- [89] P. B. Weichman, “Dirty bosons: Twenty years later,” *Mod. Phys. Lett. B*, vol. 22, pp. 2623–2647, 2008.
- [90] S. J. Thomson, L. S. Walker, T. L. Harte, and G. D. Bruce, “Measuring the edwards-anderson order parameter of the bose glass: A quantum gas microscope approach,” *Phys. Rev. A*, vol. 94, p. 051601, 2016.
- [91] A. R. Abadal, “Probing quantum thermalization and localization in bose-hubbard systems,” *PhD Thesis, Ludwig-Maximilians-Universität München*, June 2020.
- [92] J.-C. Yu, S. Bhave, L. Reeve, B. Song, and U. Schneider, “Observing the two-dimensional bose glass in an optical quasicrystal,” *Nature*, vol. 633, pp. 338–343, 2024.
- [93] S. G. Söyler, M. Kiselev, N. V. Prokof’ev, and B. V. Svistunov, “Phase diagram of the commensurate two-dimensional disordered bose-hubbard model,” *Phys. Rev. Lett.*, vol. 107, p. 185301, 2011.

Bibliography

- [94] V. Gurarie, L. Pollet, N. V. Prokof'ev, B. V. Svistunov, and M. Troyer, "Phase diagram of the disordered bose-hubbard model," *Phys. Rev. B*, vol. 80, p. 214519, 2009.
- [95] C. Meldgin, U. Ray, P. Russ, D. Chen, D. Ceperley, and B. DeMarco, "Probing the bose glass–superfluid transition using quantum quenches of disorder," *Nat. Phys.*, vol. 12, pp. 646–649, 2016.
- [96] G. Chauveau, C. Maury, F. Rabec, C. Heintze, G. Brochier, S. Nascimbene, J. Dalibard, J. Beugnon, S. Roccuzzo, and S. Stringari, "Superfluid fraction in an interacting spatially modulated bose-einstein condensate," *Physical Review Letters*, vol. 130, p. 226003, 2023.
- [97] M. Schreiber, S. S. Hodgman, P. Bordia, H. P. Lüschen, M. H. Fischer, R. Vosk, E. Altman, U. Schneider, and I. Bloch, "Observation of many-body localization of interacting fermions in a quasirandom optical lattice," *Science*, vol. 349, pp. 842–845, 2015.
- [98] P. Bordia, H. Lüschen, S. Scherg, S. Gopalakrishnan, M. Knap, U. Schneider, and I. Bloch, "Probing slow relaxation and many-body localization in two-dimensional quasiperiodic systems," *Phys. Rev. X*, vol. 7, p. 041047, 2017.
- [99] J. Billy, V. Josse, Z. Zuo, A. Bernard, B. Hambrecht, P. Lugan, D. Clément, L. Sanchez-Palencia, P. Bouyer, and A. Aspect, "Direct observation of anderson localization of matter waves in a controlled disorder," *Nature*, vol. 453, pp. 891–894, 2008.
- [100] M. Piraud and L. Sanchez-Palencia, "Tailoring anderson localization by disorder correlations in 1d speckle potentials," *Eur. Phys. J. Spec. Top.*, vol. 217, pp. 91–102, 2013.
- [101] M. Pasienski, D. McKay, M. White, and B. DeMarco, "A disordered insulator in an optical lattice," *Nat. Phys.*, vol. 6, pp. 677–680, 2010.

Bibliography

- [102] M. Sbroscia, K. Viebahn, E. Carter, J.-C. Yu, A. Gaunt, and U. Schneider, “Observing localization in a 2d quasicrystalline optical lattice,” *Phys. Rev. Lett.*, vol. 125, p. 200604, 2020.
- [103] M. Di Dio, S. De Palo, E. Orignac, R. Citro, and M. L. Chiofalo, “Persisting Meissner state and incommensurate phases of hard-core boson ladders in a flux,” *Phys. Rev. B*, vol. 92, pp. 1–5, 2015.
- [104] J. Carrasquilla, F. Becca, and M. Fabrizio, “Bose-glass, superfluid, and rung-mott phases of hard-core bosons in disordered two-leg ladders,” *Phys. Rev. B*, vol. 83, p. 245101, 2011.
- [105] B. Paredes, A. Widera, V. Murg, O. Mandel, S. Fölling, I. Cirac, G. V. Shlyapnikov, T. W. Hänsch, and I. Bloch, “Tonks–girardeau gas of ultracold atoms in an optical lattice,” *Nature*, vol. 429, pp. 277–281, 2004.
- [106] P. Donohue, M. Tsuchiizu, T. Giamarchi, and Y. Suzumura, “Spinless fermion ladders at half filling,” *Phys. Rev. B*, vol. 63, pp. 451211–451218, 2001.
- [107] M. S. Block, R. V. Mishmash, R. K. Kaul, D. N. Sheng, O. I. Motrunich, and M. P. Fisher, “Exotic gapless mott insulators of bosons on multileg ladders,” *Phys. Rev. Lett.*, vol. 106, p. 046402, 2011.
- [108] M. Atala, M. Aidelsburger, M. Lohse, J. T. Barreiro, B. Paredes, and I. Bloch, “Observation of chiral currents with ultracold atoms in bosonic ladders,” *Nat. Phys.*, vol. 10, pp. 588–593, 2014.
- [109] A. Keleş and M. Oktel, “Mott transition in a two-leg Bose-Hubbard ladder under an artificial magnetic field,” *Phys. Rev. A*, vol. 91, p. 013629, 2015.
- [110] E. Orignac, R. Citro, M. Di Dio, S. De Palo, and M. L. Chiofalo, “Incommensurate phases of a bosonic two-leg ladder under a flux,” *New J. Phys.*, vol. 18, p. 055017, 2016.

Bibliography

- [111] A. Petrescu, M. Piraud, G. Roux, I. P. McCulloch, and K. Le Hur, “Precursor of the Laughlin state of hard-core bosons on a two-leg ladder,” *Phys. Rev. B*, vol. 96, p. 014524, 2017.
- [112] M. Piraud, F. Heidrich-Meisner, I. P. McCulloch, S. Greschner, T. Vekua, and U. Schollwöck, “Vortex and Meissner phases of strongly interacting bosons on a two-leg ladder,” *Phys. Rev. B*, vol. 91, p. 140406, 2015.
- [113] E. Wybo, A. Bastianello, M. Aidelsburger, I. Bloch, and M. Knap, “Preparing and analyzing solitons in the sine-gordon model with quantum gas microscopes,” *PRX Quantum*, vol. 4, p. 030308, 2023.
- [114] A. Eckardt, “Colloquium: Atomic quantum gases in periodically driven optical lattices,” *Rev. Mod. Phys.*, vol. 89, p. 011004, 2017.
- [115] C. Weitenberg and J. Simonet, “Tailoring quantum gases by floquet engineering,” *Nat. Phys.*, vol. 17, pp. 1342–1348, 2021.
- [116] C. Sträter, S. C. Srivastava, and A. Eckardt, “Floquet realization and signatures of one-dimensional anyons in an optical lattice,” *Phys. Rev. Lett.*, vol. 117, p. 205303, 2016.
- [117] J. Kwan, P. Segura, Y. Li, S. Kim, A. V. Gorshkov, A. Eckardt, B. Bakker-Hassani, and M. Greiner, “Realization of 1d anyons with arbitrary statistical phase,” *Science*, vol. 386, pp. 1055–1060, 2024.
- [118] A. Eckardt, C. Weiss, and M. Holthaus, “Superfluid-insulator transition in a periodically driven optical lattice,” *Phys. Rev. Lett.*, vol. 95, p. 260404, 2005.
- [119] H. Zhao, J. Vovrosh, F. Mintert, and J. Knolle, “Quantum many-body scars in optical lattices,” *Phys. Rev. Lett.*, vol. 124, p. 160604, 2020.
- [120] J. Xu, Q. Gu, and E. J. Mueller, “Realizing the haldane phase with bosons in optical lattices,” *Phys. Rev. Lett.*, vol. 120, p. 085301, 2018.
- [121] H. Ranganath, “Single-atom imaging of 40k via raman sideband cooling,” *PhD Thesis, University of Strathclyde*, 2022.

Bibliography

- [122] H. Otoishi, S. Nagata, T. Yukawa, K. Yamashita, and T. Kinoshita, “Rapid production of a rb 85 bose-einstein condensate in a double compressible optical dipole trap,” *Phys. Rev. A*, vol. 102, p. 023316, 2020.
- [123] E. Altman, W. Hofstetter, E. Demler, and M. D. Lukin, “Phase diagram of two-component bosons on an optical lattice,” *New J. Phys.*, vol. 5, p. 113, 2003.
- [124] Z. Li, S. Singh, T. Tscherbul, and K. Madison, “Feshbach resonances in ultracold rb 85-rb 87 and li 6-rb 87 mixtures,” *Phys. Rev. A*, vol. 78, p. 022710, 2008.